Presynaptic biogenesis by axonal transport of lysosome-related vesicles

Inaugural-Dissertation

to obtain the academic degree

Doctor rerum naturalium (Dr. rer. nat)

submitted to the Department of Biology, Chemistry and Pharmacy of the

Freie Universität Berlin

by

Ulises Rey

born in

Barcelona

Berlin, January 2018

This thesis was prepared between the Charité and the Freie Universität Berlin, Department of Genetics, from August 2013 until January 2018 under the supervision of Prof. Dr. Stephan Sigrist.

1st Reviewer: Prof. Dr. Stephan Sigrist

2nd Reviewer: Prof. Dr. Hans-Joachim Pflüger

Date of defence: 15.06.2018

Herewith I declare that my thesis “Presynaptic biogenesis by axonal transport of lysosome-related vesicles” has been written independently and all the parts taken from previous scientific works are indicated, quoted and referenced as such.

Ulises Rey

Berlin January 2018

a la meva mare

y a mi padre

con cariño

Table of contents

Summary

The most complex and the same time the most interesting entity in the universe, the brain, remains largely enigmatic. The building blocks of it, neurons, are highly specialized processing units that together underlie more complex processes. Neurons communicate with each other via synapses, where they exchange information. This information exchange needs to be very precise and is tightly controlled in space and time. In order to their sophisticated jobs, neurons depend on a highly specialized morphology. To send information to other neurons, evolution has engineered the axon, a long prolongation of the cell membrane that resembles a wire. The axon is efficient at propagating electric signals because they do not require the transfer of mass, however transport of proteins and organelles to support the extended axons and distant synapses is a challenge. The problem is that the exact mechanisms that orchestrate and regulate the transport of active zone precursors are far from being fully understood. In my doctoral research, I analyzed the cellular machinery and processes that organize axonal transport.

Drosophila melanogaster is a highly suitable model to understand these processes. Particularly, the larval stage is highly accessible to intravital and super-resolution light microscopy techniques, while the abundance of genetic tools allows for dissection of the various elements in an unprecedented manner. By using fluorescent tags to label synaptic proteins, I was able to quantitatively characterize their transport to the synaptic terminal in the living intact animal. Moreover, the genetic tools that the *Drosophila* community has elaborated allowed to generate mutants of different proteins involved in the process to see how transport and synapse function are affected when they are absent or altered.

In the current work, I present evidence that presynaptic biogenesis is mediated by axonal co-transport of active zone proteins and synaptic vesicle proteins in a new organelle that resembles lysosomes, we named PLV (presynaptic lysosome-related vesicle). By intravital in vivo imaging of *Drosophila* larvae, we have been able to see how synaptic proteins and active zone components are transported together with proteins of the lysosomal pathway. Furthermore, we show how Arl8, a kinesin adaptor for lyososomal transport, is also required for proper transport of synaptic proteins. Loss of Arl8 results in the depletion of synaptic proteins at the presynaptic sites, which in turn leads to impaired neurotransmission. In the absence of Arl8, the PLVs accumulate in neuronal cell bodies and hardly any axonal transport can be observed. The characterization of these accumulations showed that these vesicles are around 70 nm in diameter, and are positive for synaptic markers as well as active zone proteins. Conversely, up regulation of Arl8

results in an increase in axonal transport of PLVs proteins and presynaptic function is facilitated. These data was supported by experiments in mouse models with comparable results.

To conclude, this work reveals an unexpected function for a lysosome-related organelle as the basic building block for presynaptic biogenesis and contributes to a better understanding of axonal transport.

Zusammenfassung

Das komplexeste und gleichzeitig interessanteste Gebilde des Universums, das Nervensystem, ist nach wie vor eines der am wenigsten verständlichen. Seine Bausteine, die Neuronen, sind hochspezialisierte Verarbeitungseinheiten die gemeinsam die Grundlage für noch komplexere Prozesse bilden. Kommunikation und Informationsaustausch zwischen den Neuronen erfolgen über die Synapsen. Dieser Informationsaustausch muss sehr präzise sein und wird in Raum und Zeit streng kontrolliert. Um diese raffinierte Aufgabe erfüllen zu können sind Neuronen in ihrem Aufbau hoch spezialisiert. Um Informationen an weiter entfernte Zellen zu senden hat die Evolution das Axon erfunden, ein langer Fortsatz der Zellmembran, der einem Draht ähnelt. Das Axon ist sehr effizient bei der Weiterleitung elektrischer Signale, da diesen kein Stofftransport zu Grunde liegt. Der Transport von Proteinen und Organellen über lange Distanzen stellt jedoch eine Herausforderung dar. Während meiner Doktorarbeit habe ich versucht die Mechanismen und Prozesse zu verstehen, die zur Überwindung dieses Hindernisses beitragen können.

Drosophila melanogaster bildet ein großartiges Model zur Untersuchung dieses Prozesses. Bereits im Larvenstadium ist eine mikroskopische Untersuchung mit verschieden Techniken möglich. Die Vielfalt der vorhandenen genetischen Werkzeuge erlaubt dabei ein genaues Sezieren der verschiedenen Komponenten. Als ich meine Arbeit begann war wenig darüber bekannt, welche Mechanismen dem axonalen Transport der synaptischen Proteine zugrunde liegen. Unter Nutzung fluoreszierender Marker zur Kennzeichnung der synaptischen Proteine war es mir möglich ihren Transport zum synaptischen Endknöpfchen *in vivo* zu charakterisieren. Zudem erlaubten es mir die, von der *Drosophila*-Wissenschaftsgemeinschaft entwickelten, genetischen Werkzeuge, Mutanten verschiedener, am Prozess beteiligter Proteine, zu erzeugen. Mithilfe dieser Mutanten konnte beobachtet werden, wie der axonale Transport und die synaptischen Funktionen beeinflusst werden, wenn die Transportproteine abwesend sind oder verändert werden.

Mit der vorliegenden Arbeit liefere ich den Beweis, dass eine präsynaptische Biogenese von axonalem Cotransport von Proteinen der aktiven Zone und synaptischen Vesikelproteinen in einem neuen Organell vermittelt wird. Dieses ähnelt in seiner Struktur und Funktion einem Lysosom weshalb wir es PLV (presynaptic lysosome-related vesicle) genannt haben. Mithilfe der intravitalen (*in vivo*) Bilderfassung war es uns möglich zu sehen, wie synaptische Proteine und Teile der aktiven Zone gemeinsam mit Proteinen des lysosomalen Weges transportiert werden. Darüber hinaus zeigen wir wie Arl8, ein

Kinesin-Adaptor für den lysosomalen Transport, auch für den reibungslosen Transport synaptischer Proteine benötigt wird. Der Wegfall von Arl8 ruft einen Abbau synaptischer Proteine auf der präsynaptischen Seite hervor, welcher zu Beeinträchtigung der Neurotransmission führt. In Abwesenheit von Arl8 akkumulieren die PLVs in Nervenzellkörpern und es kann kaum noch axonaler Transport beobachtet werden. Die Charakterisierung dieser Akkumulierungen hat gezeigt, dass die Vesikel ca. 70 nm Durchmesser haben und sie sowohl synaptische Marker, wie auch Proteine der aktiven Zone beinhalten. Umgekehrt bewirkt eine Hochregulierung der Expression von Arl8 einen Anstieg des axonalen Transports der PLVs, wodurch die präsynaptische Funktion erleichtert wird. Diese Daten wurden von Experimenten mit Maus-Modellen untermauert, welche vergleichbare Ergebnisse lieferten.

Zusammenfassend kann gesagt werden, dass die vorliegende Arbeit eine unerwartete Funktion eines mit Lysosomen verwandten Organells, als Grundbaustein für die präsynaptische Biogenese enthüllt, und zum besseren Verständnis des axonalen Transports beiträgt.

Introduction

Introduction

Neuroscience

Neuroscience or Neurobiology is the scientific discipline that studies the nervous system. Although the study of the brain can be traced back in time to the ancient Egypt, it has not been until the emergence of the scientific method that it has developed into a *science* according to the definition from a modern perspective.

To introduce the work of this thesis I would like to start by presenting the discoveries of two neuroscientists that in my opinion are the founders of the field as we know it nowadays: Camillo Golgi (1843-1926) and Santiago Ramón y Cajal (1852-1934), both awarded the Nobel Prize in 1906 for their studies on the structure of the nervous system.

At the time, there were two opposing theories as to how the nervous system was organized: the neuron doctrine and the reticular theory. The neuron doctrine was an extension from the cell theory, which was proposed after improvements made to microscopes allowed to identify single "units" as building blocks of tissue. As such, the neuron doctrine proposed that the brain and the nervous system were not an exception and that it was made up of discrete cells. On the other hand, the reticular theory proposed that the nervous system was a continuous network.

Camillo Golgi discovered in 1873 a new staining technique, named la *reazione nera* (the black reaction). This protocol, based on silver, stained only a fraction of the cells of the nervous system and they appeared black under a light microscope. This technique was used by Santiago Ramón y Cajal and allowed him to see the "celled" organisation of the nervous system. With his fantastic drawings, Ramón y Cajal popularized and confirmed the nowadays-accepted neuron doctrine, that is, that the nervous system is organized by many individual cells, which build the circuits of the nervous system.

A

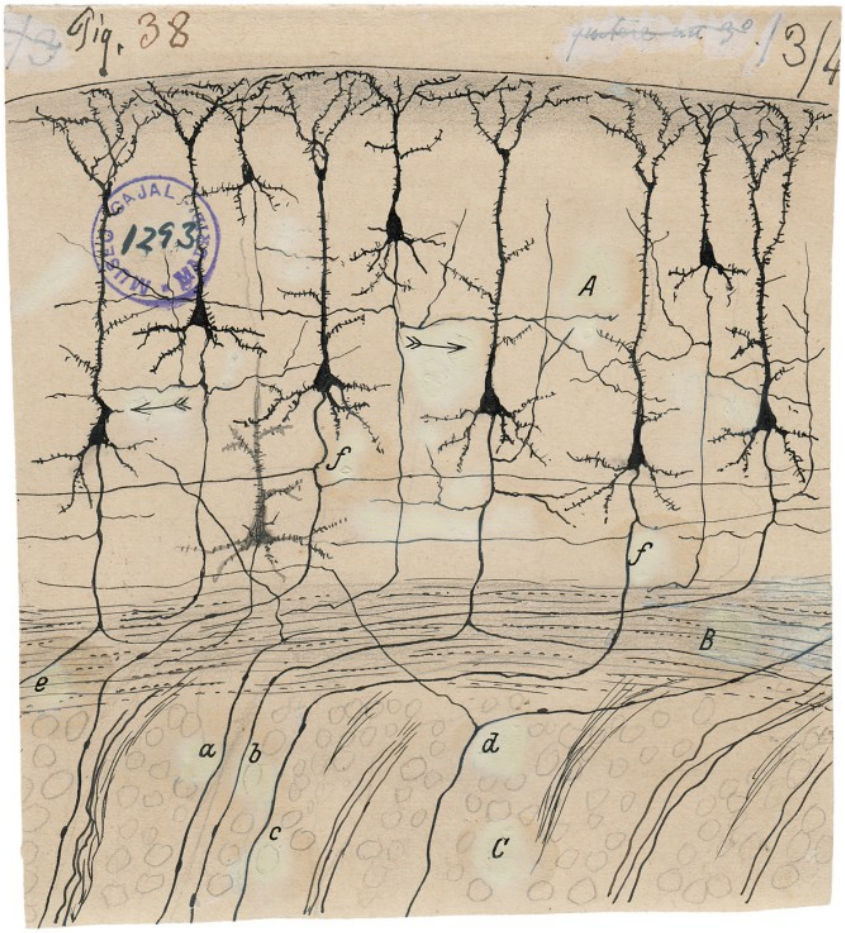

Fig. 1 | Structure and connections of Neurons.

(A) Drawing of Pyramidal neurons of the central cortex and their axon pathways by Santiago Ramón y Cajal (Picture from the exhibition at Ciutat de les Arts i les Ciències, València).

Models for Neurobiology studies

One of the aims of biomedical research is to have a better understanding of human physiology to prevent and cure diseases. In the field of neuroscience, gaining a deeper understanding of the physiology of the nervous system will not only increase our biological understanding but may open routes prevent, mitigate and cure neuronal disorders. To understand how an organ or tissue of the human body functions one has to have access to it. For neuroscience one of the problems is that the skull protects the human brain, making it difficult to access, thus obtaining brain samples has been limited patients undergoing brain surgery or from organ donations from deceased people. A very recent solution to this has been the use of modern techniques such as Computer Tomography

(TC) or fMRI (Functional Magnetic Resonance Imaging) which allows imaging of the brain in a non-invasive manner. However, these methodology can be costly and therefore, as a strategy to circumvent this, neuroscientists have studied non-human brains as models for the human brain. Most animals have brains and their nervous system is related to human because it originated from a common ancestor and therefore are evolutionary related to each other, that is, they are homologous (Darwin, 1859). Choosing a model organism to study the nervous system is complicated, and many factors are involved. Probably the most determinant is the trade-off between similarity and ethics. Animals that are more similar to us are a priori a better system to study, however, also because they are more similar to us they demand a better ethical treatment. On the other side we have animals that are less similar to us, so there are lesser ethical concerns, but at the same time, by studying them we can learn less about our brain.

Historically the field of neuroscience has used animals in this spectrum for their studies: from chimpanzees or great apes, to monkeys, mice or rats, birds, fish, insects or annelids. Also historically, there has been a trend towards an increase in ethical requirements that has significantly decreased the number of experiments performed in our closest relatives. This has gone as far as to completely stop the breeding program of our closest relatives, the chimpanzees, by the NIH in 2007 (Cohen, 2007; Knight, 2008).

In this context, most of the research conducted in this thesis has used an insect, the *Drosophila melanogaster*, as a model organism.

Drosophila melanogaster

Drosophila melanogaster, or commonly known as the fruit fly, is an insect of the Diptera order. Thomas Hunt Morgan pioneered the use of *D. melanogaster* as a model organism for genetics studies at the beginning of the XX century. He isolated a white eye mutant fly and described the transmission of the trait in accordance with mendelian ratios (Morgan, 1911). Since then, the field of Drosophila genetics has expanded exponentially and it is now one of the most used animal models for research including neuroscience.

There are several advantages which make Drosophila a preferred choice over other animal models that have a closer evolutionary relationship to humans (Jennings, 2011) First of all they are very easy to grow and maintain. *Drosophila melanogaster* have very well identified life cycle, which is also comparatively short to most vertebrates. From the moment the egg is laid until an adult fly emerges from the pupa there is only a 10 days interval in normal conditions (Fig. 2 A-B). This cycle is temperature dependent, and it is faster at higher temperatures (up to 29º C) and slower at low temperatures (18 ºC). They can live in small vials and can feed on fruit or a variety of foods easy to prepare. Their

standard laboratory food preparation consists of corn and soy flour with syrup, yeast and propionic acid, plus agar to confer gel consistency, is also very easy to prepare (Lakovaara, 1982; Jennings, 2011).

Drosophila genome is organized in 4 chromosomes, which makes gene mapping fairly easy. Moreover, in 1881 Balbani discovered that the chromosomes in the salivary glands of insects are extremely big, reaching up to 200 μm in length (Fig. 3 A), which makes them observable under the microscope (Fig. 3 A).

Work from Painter during the 30s described in very much detail how these salivary gland chromosomes, also called polytene chromosomes, are organized. Polytene chromosomes are found in the giant cells of the salivary glands. DNA molecules in these cells undergo multiple cycles of DNA synthesis without cell division. The resulting cells can contain as many as several thousand times the normal DNA complement. More interestingly and contrary to other polyploid cells, these secretory larval cells have all the homologous chromosome copies held together side by side, like pick up sticks in a bundle, creating a single polytene chromosome. A salivary gland cell of a Drosophila larva can undergo 10 DNA replication cycles without cell division, creating 2^{10} (1024) identical strands of chromatin perfectly aligned. Polytene chromosomes are easy to visualize with light microscopy and have unique band patterns that allow for topographic characterization.

A

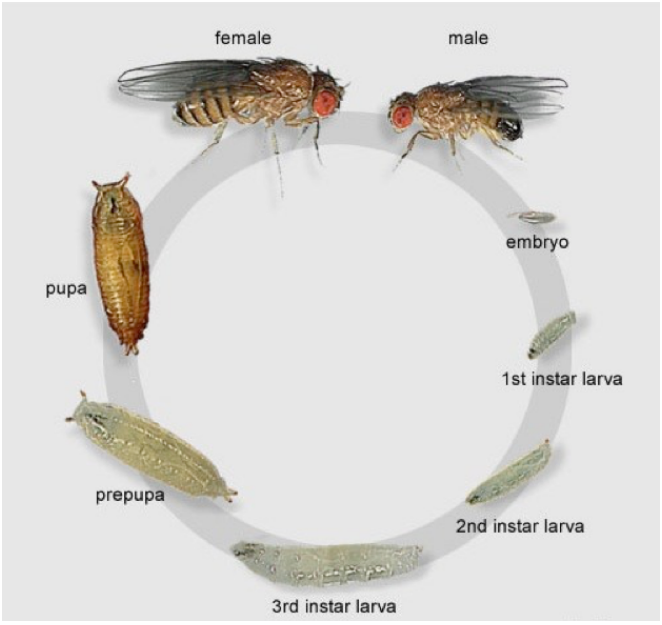

B

Time after fertilization

Hour	Days	Developmental event (at 25 ºC)
24	1	Hatching from egg; first larval instar begins
49	2	First molt; second instar begins
72	3	Second molt; third instar begins
120	5	Puparium formation; puparium white
122	5.1	Puparium fully colored
124	5.2	Prepupal molt
132	5.5	Pupation; cephalic complex, wings, legs everted
169	7	Eye pigmentation begins
189	7.9	Bristle pigmentation begins
216	9	Adult ready to emerge from pupa case

Adapted from (Doane 1967) and http://flymove.uni-muenster.de

Fig. 2 | The life cycle of *Drosophila melanogaster*.

(A-B) After female and male adult flies mate, female flies lay fertile eggs containing embryos. After 24h the first larva hatch from the egg to feed and grow. The two molt events that separate the three larval stages. After 3 days the last, 3rd instar, larval stage is fully developed and crawls high to pupate. In the pupae metamorphosis happens during ~4 days until the adult fly fully developed emerges.

A

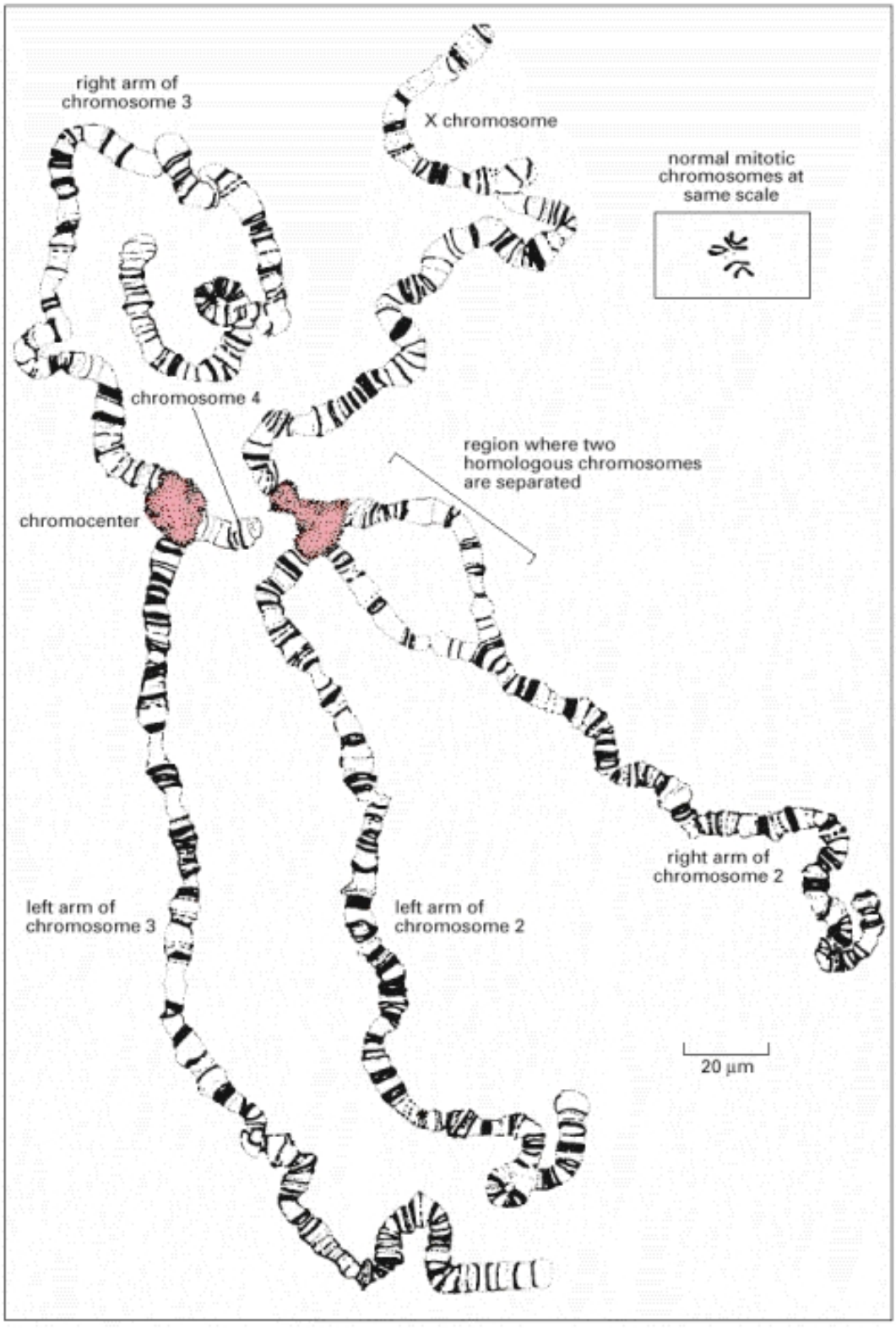

Fig. 3 | The polytene chromosomes.

(A) The first drawing from Painter of the polytene chromosomes found on the salivary glands of *Drosophila melanogaster* larvae (1934). In this drawing the 4 chromosomes as well as their respective arms can be easily seen. Each parental chromosome is tightly

paired with its homologue and there are regions where they are separated (asynapsis). See the upper right square for comparison with normal mitotic chromosomes.

Drosophila was the second animal to have its genome sequenced (Adams et al., 2000) (only after *C. elegans* (Consortium*, 1998)), and with the development of large number of genetic tools (Fraser et al., 1983; Jenett et al., 2012; Jennings, 2011) makesthe fruit fly an ideal candidate as an animal model.

GAL4 UAS System

One of the most useful genetic tools is the GAL4 UAS system. In 1993, Brand and Perrimon published a landmark article describing the GAL4 upstream activating sequence (UAS) system to target gene expression in Drosophila (Brand and Perrimon, 1993). This system has become one of the most powerful tools for studying gene function. This method is based on two components from the yeast *Sccharomyces cerevisiae* gene regulatory machinery. GAL4 is a transcription factor (TF) that activates transcription of its target genes by binding to specific *cis*-regulatory sites (CREs) called UAS. In Drosophila, the idea is to have one Drosophila line expressing the GAL4 TF in tissues or cell lines marked by a genomic enhancer for that tissue. The second component is in another Drosophila line, which carries the gene or construct of interest with UAS as a CRE. When the two parental lines are crossed the resulting offspring will bear the two components, and the GAL4 TF will be activated in the tissue of selection. Once TF binds to the UAS sequence the gene after it will be expressed only in the cell line specified by the GAL4 driver. In all the other cell lines the gene will not be expressed. The advantage of this bipartite system is that one can generate a library of GAL4 lines with different enhancers and these can be combined with any existing UAS construct. Different research groups can generate new GAL4 driver lines or new UAS constructs allowing for and almost infinite number of combinations (Fig. 4 A). The potential of this tool can go as far as finding an enhancer for every cell type. In 2012 laboratories in the Janelia Research Campus generated 7000 GAL4 lines to target different neuronal cell lines (Jenett et al., 2012). Of course, the system has some limitations (Ito et al., 2003). The most important to take into account is that the gene of interest will be expressed under an exogenous promoter and its expression will not be regulated by endogenous feedback mechanisms that act at the level of gene transcription. Therefore, one has to keep in mind that the amount of protein expressed is not the same as it would be with the endogenous

promoters. Because the system comes from the budding yeast, its activity is higher at higher temperatures, and vice versa, and can be regulated depending on the temperature flies are reared. The second limitation to take into account is that the size of the sequence that can be inserted into the genome is limited. Therefore most of the time the construct inserted contains only exons and when so, any regulation that could happen at the splicing level is lost.

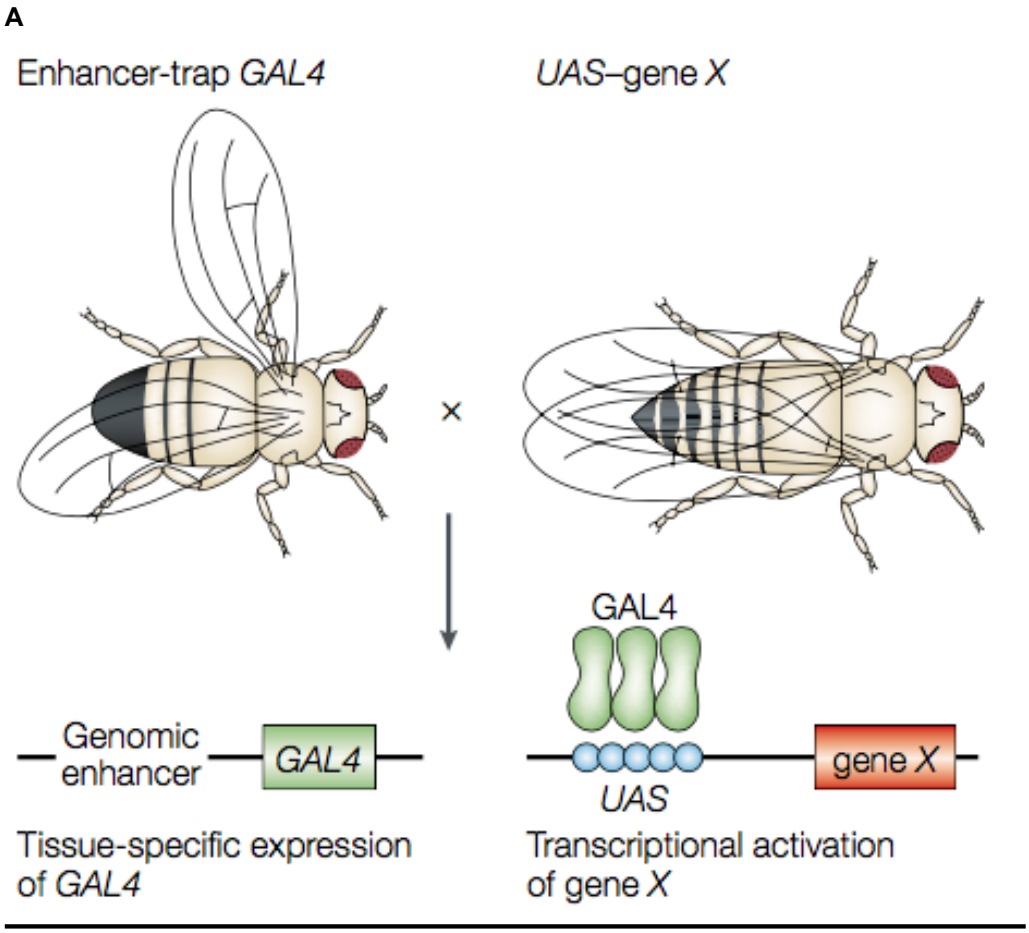

Adapted from (Johnston 2002).

Fig. 4 | The GAL4-UAS System for targeted gene expression.

(A) The yeast transcriptional activator GAL4 can be used to regulate gene expression in Drosophila by inserting the upstream activating sequence (*UAS*) to which it binds next to a gene of interest (gene *X*). The *GAL4* gene has been inserted at random positions in the Drosophila genome to generate 'enhancer-trap' lines that express *GAL4* under the control of nearby genomic enhancers, and there is now a large collection of lines that express *GAL4* in a huge variety of cell-type and tissue-specific patterns. Therefore, the expression of gene *X* can be driven in any of these patterns by crossing the appropriate *GAL4* enhancer- trap line to flies that carry the *UAS*–gene *X* transgene.

Another resource that has been of great use for this thesis and for the Drosophila community in general is the existence of UAS-RNAi lines for almost every gene, produced by the Vienna Drosophila Resource Center (Dietzl et al., 2007). In a nutshell, the RNAi technology allows silencing of protein expression, not by acting at the gene level, nor by inhibiting protein function, but by blocking the mRNA. Here, a the genome with a small sequence is transcribed into RNA. The sequence is coded to have a base pair complementation leading to binding to the native mRNA of the target gene (Napoli et al., 1990). The hybridization of the two strands physically blocks mRNA from binding to ribosomes for protein translation resulting in degradation of the mRNA. This resource enables large-scale genetic screens, making it possible to carry out loss-of-function experiments in essentially any tissue or cell at any stage in the life of the organism. When crossed to a GAL4 driver line, the UAS-RNAi stocks induce expression of a specific hairpin structure, which silences expression of the target gene via RNAi. Collectively, the RNAi lines cover a total of 12,671 (91%) of the *D. melanogaster* protein-coding genes.

As seen, the GAL4/UAS system and its extensions allow in vivo experimental dissection of a wide range of biological questions (Valakh et al., 2012; Busson and Pret, 2007; Kvon et al., 2014).

The Neuron

Neurons are the smallest single units composing the nervous system responsible for receiving, processing and transmitting information. For example, an olfactory or visual stimuli and be integrated and processed to respond has a feeding behavior, for instance via the contraction of a muscle via the activation of a motoneuron (neurons that control muscular activity) There is a very wide range of neuron types depending on the function and the organism we are considering.

There are also other cell types apart from neurons that also constitute the nervous system. These include oligodendrocytes, the astrocytes and the microglia, and their function is to support neurons. Although there is growing evidence that non-neuronal cells play more active roles within the neuronal system (Trotta et al., 2018; Ronzano, 2017; Stephen D. Skaper et al., 2017) since they are out of the scope of this thesis they will not be described any further.

As mentioned, Neurons will have different sizes and morphology, depending on their specific function and their localization in the nervous system or the organism,

neurons have different sizes and morphology. One example of a neuron is the motor neuron (Fig. 5).

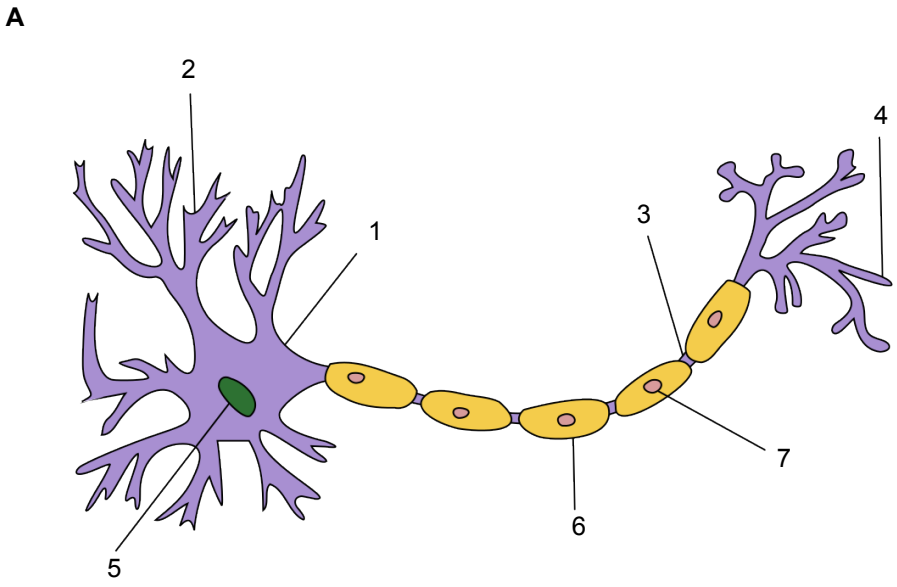

Fig. 5 | The stereotypical neuron.
(A) Represents a standard myelinated neuron depicting its most important parts. (1) Is the cell soma. (2) The dendritic tree where signals from other neurons are received. (3) The axon, through which the signal, as an electric action potential is transmitted until the synaptic terminal (4). (5) Is the nucleus of the neuron. (6) Is the myelin sheath produced by the Schwann cells (7), which fosters faster transmission of the electric current. Schwann cells are glia cells of the peripheral nervous system and are not found in all neurons.

The main three parts of our chosen neuron are the cell body or soma, the dendrites, the axon and the synaptic terminal. The cell body (1) of the neuron is where the nucleus is, and where most of the non-specific cellular processes mainly take place: transcription, protein synthesis and metabolism. The dendrites (2) are branched structures specialized in establishing contacts with the surrounding neurons from where they receive inputs, these inputs are also sent by the dendrites to the soma, where they are processed and integrated. After the cell body has processed the information, the neuron propagates the signal further to its corresponding target cell via the axon (3). The target cells can be another neuron or a different cell type. The length of the axon is always very long if one compares it to the average dimensions of a cell, but it is especially long when the target

cell is not another neuron within the central nervous system or vicinity but one from a target organ far away. This is the case of all motoneurons, whose target cell is a myocyte that can be up to meters away. The information is transmitted through the axon until it arrives at the synaptic terminal (4), where the axon branches to innervate the target cell in what is called the synapse.

The Axon

Even animals that we consider small, like for example the fruit fly, are relatively big compared to the dimensions of a cell or of a neuron. This fact, explains the existence of the axon. Neurons perceive information from parts of the body that might be very far away from the brain. After this information has been received, neurons need to send commands or instructions to response cells that are far away from where it was processed. For the fruit fly, a typical 8 μm diameter motoneuron needs to send information to muscles that are 6 mm away, that is almost 100 times larger, so a difference of two orders of magnitude. This of course increases in bigger animals, for instance the distance a human motoneuron has to cover can be up to 1 m, a difference of 10000 times. This multiscale challenge was solved with the evolution of a long projection from the nerve cell that is specialized in transmitting information along very long distances: the axon.

The axon originates adjacent to the cell body in a region known as the axon hillock, and from there the prolongation extends until the target cell. As we said, the primary function of the axon is to transmit information. The way the axon does it is via an electric impulse that is transmitted downstream from the cell soma to the synaptic terminal. In most organisms this is performed via an action potential (Lockery and Goodman, 2009; Lockery et al., 2009; Mellem et al., 2008).

Along the axon there are sodium and potassium channels that control the electric potential of the neuron. At a resting state, the membrane of the neuron has an electric potential of -70 mV. This difference in potential the neuron has in respect to the extracellular fluid is achieved by a difference in Na^+ and K^+ ions concentration regulated by ion channels present all along the membrane of the axon that control ion flux (Fig 6. A). When the neuron is activated, then voltage gated Na^+ channels open and let sodium enter the neuron, producing a depolarization phase, where the membrane potential arises until +40 mV. After that, sodium channels inactivate and potassium channels are activated, allowing for a K^+ efflux from the neuron to the extracellular fluid that restores the membrane potential, and then potassium channels close too. The Na^+ remain in an inactivated state known as the refractory period because no more action potentials can be

produced during this time. The temporary inactivation of the sodium channels allows for unidirectional transmission of the action potential: the impulse can only be transmitted forward because the sodium channels “behind” are inactive (Fig. 6 B) (Alberts et al., 2002).

As we see, the axon is a very efficient structure at transmitting information. It does so by sending the information via electric impulses that do not require transport of "mass" or material, every time there is an action potential. However, this very long structure becomes a challenge because the cell needs to transport all the cellular material to the tip of the axon to pass the signal further (specially important in chemical synapses). Moreover, it needs to transport other proteins and organelles that are not synapse specific but that are also required for the normal metabolism of synapse (mitochondria, degradation proteins, enzymes, etc.)

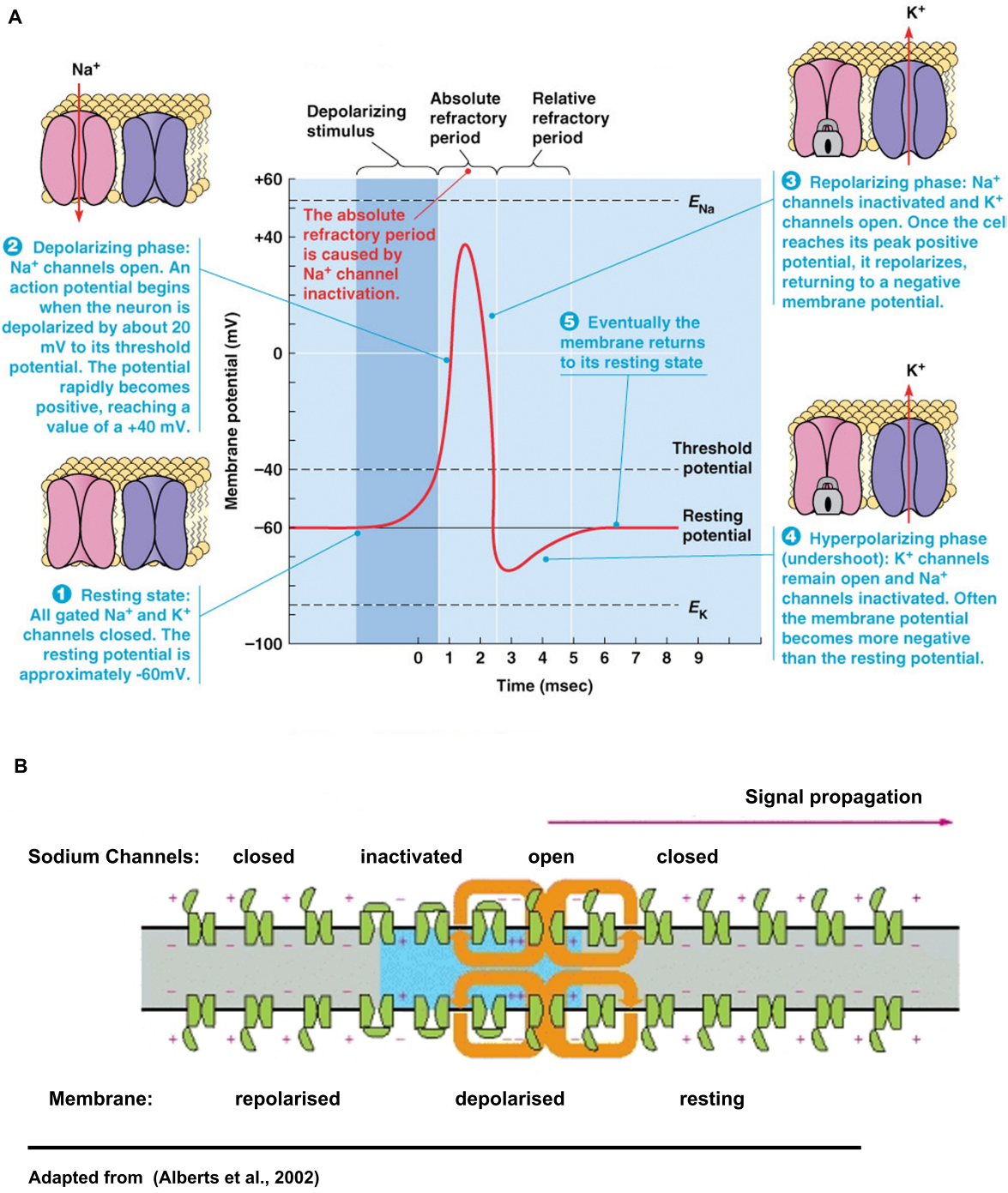

Adapted from (Alberts et al., 2002)

Fig. 6 | The action potential

(A) Description of the phases of the action potential. (1) Resting state, (2) depolarizing phase, (3) repolarizing phase and (4) hyperpolarizing phase. **(B)** Scheme on how signal propagation works via opening, inactivation and closing the sodium channels of the axon. The fact that the sodium channels are inactivated after being open, allows the signal to be transmitted unidirectionally.

The Synapse

Since Santiago Ramón y Cajal proposed that the nervous system is formed by neurons as discrete units rather than by a continuous wiring, the concept of synapse (junction) gained importance. The synapse, thus, is where the discrete units of the brain connect with each other to exchange information.

There are again no two identical synapses, but synapses have been classified into electric or chemical synapses depending on how they transmit the information. In this introduction the focus will be on the chemical synapse because is the one used in this thesis as a model (Schuster, 2006).

Since the communication is directional the synapse consists of two asymmetric parts: the presynapse and the postsynapse. The presynapse is at the very end of the axonal terminal and contains all the machinery to send the message. On the other hand, the postsynapse locates at the dendrites and has all the necessary components to receive the message and propagate it further.

The principal components of the presynapse are:

- Synaptic Vesicles
- Active Zone Cytomatrix
- Voltage Gated Calcium Channels

The main components of the postsynapse are:

- Neurotransmitter receptors

The specific synapse used as a model for most of the research done for this thesis, the Drosophila neuromuscular junction, will be described in more detail in the next chapter.

The larval Neuromuscular Junction of Drosophila as a model synapse

Drosophila larval motoneurons are a very good neuron of choice to unveil synapse function. Their cell bodies are located at the CNS but their axons project further out of it to reach the muscle target cell. The synapse between the motoneurons and the muscle cell

is called Neuromuscular Junction (NMJ). Like in vertebrate skeletal muscles, larval muscle cells are huge multinucleated fibers to allow fiber contraction in a coordinated manner. The motoneuron has to innervate a very big cell and as a result has one of the biggest synapses.

Work in late 1970s established the larval neuromuscular junction (NMJ) as a model synapse (Jan and Jan, 1976) and since then, many publications have followed studying its development, morphology and function (Halpbern et al 1991, Johansen et al 1989a, Johansen et al 1989b; Schmid et al., 2008; Fouquet et al., 2009; Petzoldt et al., 2014).

Drosophila larvae, in comparison to adult flies, are more suitable because the nerve-muscle preparation is thin and almost transparent which makes it ideal for microscopy, plus the nerve terminals are readily accessible to experimental manipulation. The nerve endings follow the stereotypical organization of the body wall muscles (Fig. 6 A). The larva is divided into 8 segments, each segment is innervated by motoneurons whose cell bodies are located in the VNC and represent a topographical map of the segments1. More anterior muscles are innervated by motoneurons that are more anterior and posterior muscles are innervated by motoneurons that are at the end of the VNC. Each segment is divided by an axis of symmetry, called the midline, which divides the larvae into two equal hemisegments (right and left). Each hemisegment consists of 30 muscles, and it is organized in two layers, one more superficial and another just underneath it. Muscles can also be categorized as dorsal, lateral or ventral depending on their position. By convention every muscle has a number (from 1 to 30) to identify it.

[1] This organization in segments or metamers, is common to many bilateral animals and human ribs or vertebrae are vestiges of it.

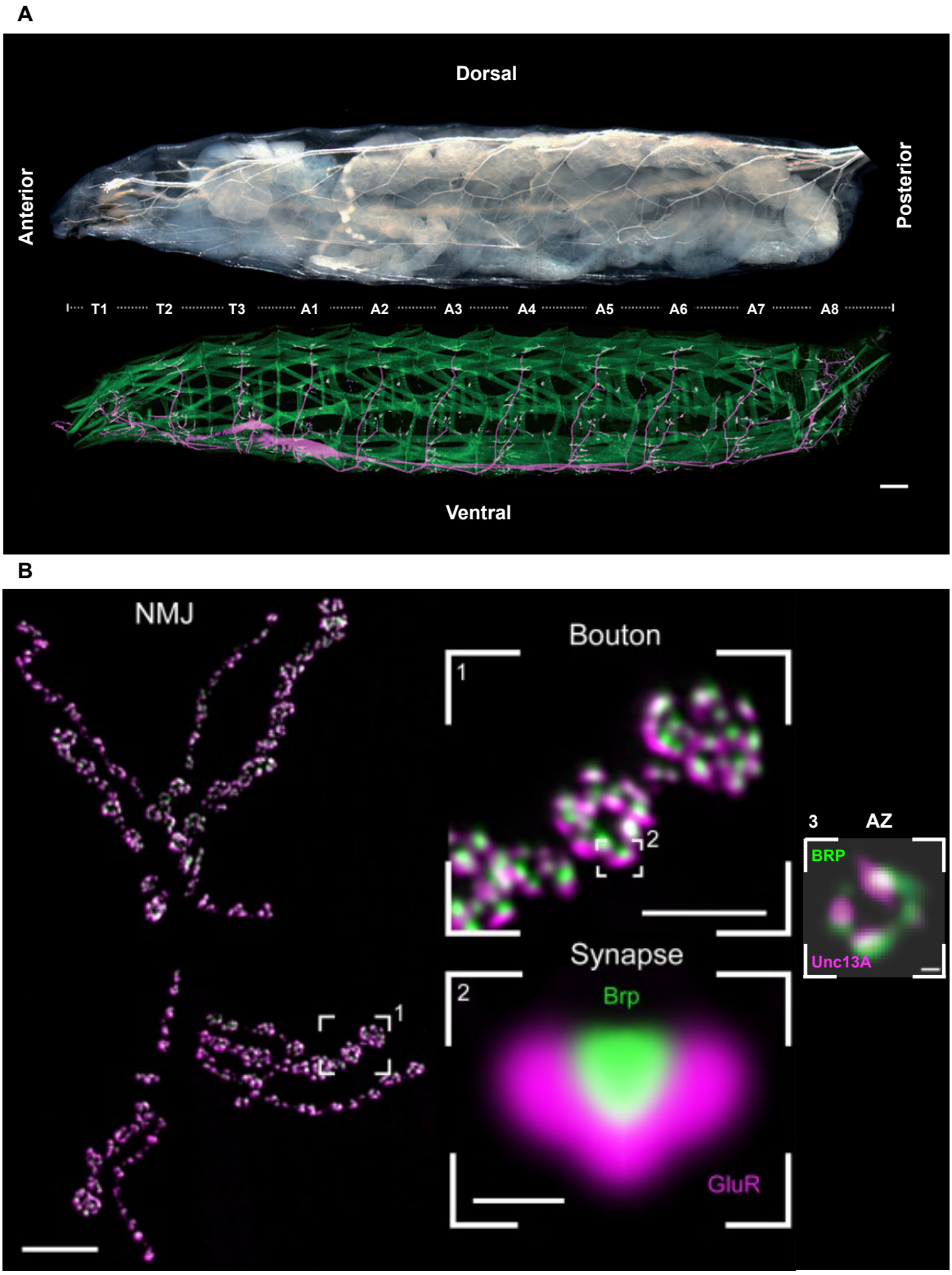

Adapted from (Ehmann 2017; Böhme 2016)

Fig. 7 | The *Drosophila* neuromuscular junction.

(A) Image of a 3rd instar larva viewed from the side, with its mouth hooks to the left and the tail to the right. In the bottom panel muscles are highlighted in green and the nervous system in purple. Muscles are organized in 8 similar segments (A1-A8) with a similar

structure and same muscle pattern. These muscles are innervated by motoneurons whose nuclei reside in the VNC (purple). **(B)** Confocal images of the NMJ synapse at its various scales. Left, whole NMJ of muscle 6/7. Right (1), magnification of the bouton structure showing the single AZ labeled with Brp (green) with the Glutamate receptor (purple) opposed to them. (2) Confocal image of a single AZ where a BRP AZ is surrounded by a Glutamate Receptor field. To resolve further the AZ organization we need to go to super resolution two color STED microscopy (3), where the BRP ring (green) is then easily identifiable, with Unc13A (purple) sitting just next to it. Scale bars: 10 µm (NMJ), 3 µm (1), 300 nm (2) and 50 nm (3).

The fact that the NMJs are big, accessible, stereotypical, repetitive structures and that they are conserved during larval development makes the larval NMJs a paradigm for synapse study and research. Data from different individuals but the very same synapse can be easily obtained, making it highly comparable.

In regards to morphology, the synapses are divided into three groups depending on the type of innervation. All the work of this thesis dealt with type-I because they are the main excitatory innervations, use glutamate as neurotransmitter, and are the most well described. Type-I synapses are divided into Type-1b (big) and Type-1s (small), and Type-1b are again the ones better understood. Type II synapses innervate more than one muscle and part of their function is to coordinate locomotion. They release octopamine instead of glutamate, which corresponds to adrenaline or noradrenaline in mammalians. Type-III are only found in some muscles and they have been also understudied in comparison to Type-I. (Koon et al., 2011; Ruiz-Canada et al., 2004; Koon and Budnik, 2012).

Type-Ib terminals are organized in beads on a string structure. The beads correspond to the boutons that are interconnected by axonal cytoplasm. The number and morphology of every terminal varies depending on the muscle. Muscle 4 is among the preferred ones for immunohistochemistry because a) it is big and easy to identify, b) it is in the inner layer, so after the larval preparation the objective can really be in direct contact to the NMJ (no tissue in between that could interfere or hinder image quality) and c) because it is smaller, less branched and does not go as deep inside the muscle as muscle 6 or 7, which makes it harder for confocal imaging. As said, every terminal is organized in boutons where the synapses are located. As the larva grows, so do the muscle and the terminal, producing more boutons by division, budding or de novo

(Pennetta et al., 2002; Menon et al., 2013). At larval stage 3, muscle 4 Type-Ib terminals can contain up to 20 boutons and its total length is between 30 and 50 µm (Fig. 7 B). Each bouton contains on average around 10 individual synapses, each containing the complete architecture and machinery to be able to transmit the signal, which is also referred as Active Zone (AZ) (Crossley et al., 1978; Menon et al., 2013).

The Active Zone

The term Active Zone was first used by Monique Pécot-Dechavassinein and René Couteaux after their observation that Synaptic Vesicles would only fuse at specific sites of the synapse (Tsuji, 2006). Indeed, the interaction surface between the presynaptic and the postsynaptic membrane is relatively large. However, by carefully looking at the ultrastructure of synapses they could observe that the profiles of fused vesicles were only to be found at specialized regions of the membrane that were more electron dense, and named them “les zones actives” (Fig. 8 A) (Tsuji, 2006). Subsequently same observations were made in other synapses, and since then many studies have further identified components of the AZ.

The AZ is the release site for SVs, and its function is to facilitate tethering, docking and fusion of SVs with the plasma membrane (Zhai et al., 2001). The actual building blocks of the AZ have been under study since the discovery by Monique Pécot-Dechavassinein and René Couteaux. The AZ components can vary between species, tissues and cells, but the basic design of the release sites is largely conserved (Fig. 8 B-D).

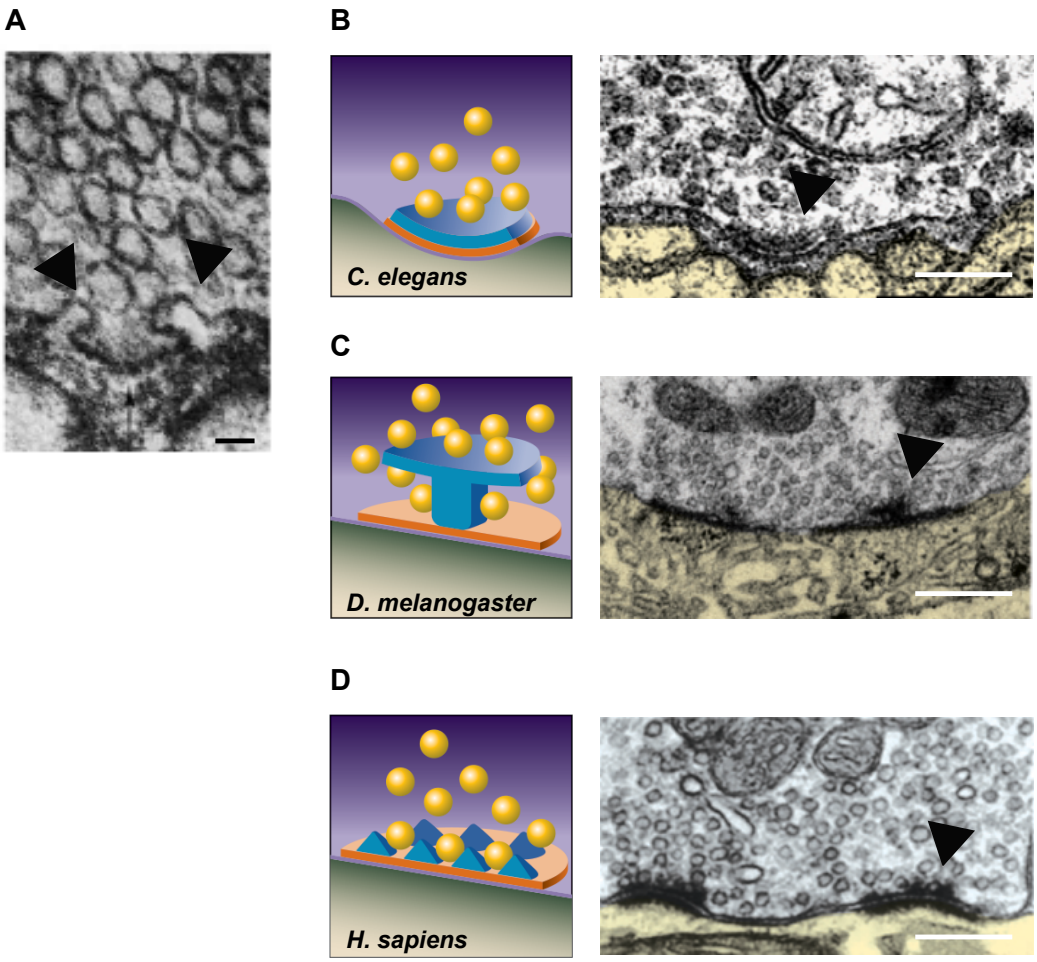

Adapted from (Couteaux and Pécot Dechavassinein, 1970; Zhai and Bellen, 2004)

Fig. 8 | Structure of cytomatrices at Active Zones.

(A) Electron microscopy image of the first Active Zone to be observed, from the experiments by Couteaux and Pécot Dechavassinein in 1970, at the frog synapse. Arrowheads show vesicles fusing at the most electron dense area of the synapse. **(B-D)** Schematic representations and EM images of the Active Zones and cytomatrices of *C.* elegans, *D.* melanogaster and *H.* sapiens. **(B)** Active Zone of the nematode *C. elegans* synapse at the NMJ. **(C)** NMJ of the fruit fly showing the characteristic T-Bar. **(D)** Human active zones at the hippocampal synapse. Scale bars are 50 nm (A) and 300 nm (B-D).

In Drosophila, thanks to the joint effort of many research groups, the various components of the AZ have been identified and their function characterized to a very large extend (Fouquet et al., 2009; Kittel et al., 2006a; Owald et al., 2010, Owald et al., 2012; Peled et al., 2014; Reddy-Alla et al., 2017). But still there is a collection to disclose. Hereafter the current status of our knowledge about the drosophila Active zone will be briefly described.

AZ formation at the NMJ starts just after embryogenesis stage 13/14 when growth cones of VNC neurons navigate to their stereotypic positions where they establish adhesive contacts with their appropriate target muscles. 13h after egg laying the whole muscular pattern is defined and AZ formation begins (Bate, 1990; Grenningloh et al., 1991; Landgraf and Thor, 2006; Sánchez-Soriano et al., 2007). The components of the AZ cytomatrix arrive in at least two waves (Fig 9 A). The early components of the AZ are Cacophony (Calcium Channel), Syd-1, Liprin-α and Unc-13B. Syd-1 arrives at the same time as Liprin-α to the presynaptic membrane of the terminal and they localize at the edge of the AZ. Via interaction with the trans synaptic complex Neurexin-Neuroligin-1, they orchestrate the early assembly of the AZ opposed to the Post Synaptic Density (PSD). At this time the process is still reversible, and clusters of Syd-1 and Liprin-α can undergo rounds of assembly and disassembly before it is decided to proceed to the next step. After Syd-1 and Liprin-α have established the site for a new AZ, the later components arrive. RBP and BRP arrive together (Siebert et al., 2015) and at the same time Unc13A is incorporated. At this point the mature synapse is formed and BRP, RBP and Unc13A act as tight calcium sensors for SV vesicle release (Fig. 9 B) (Böhme et al., 2016; Reddy-Alla et al., 2017).

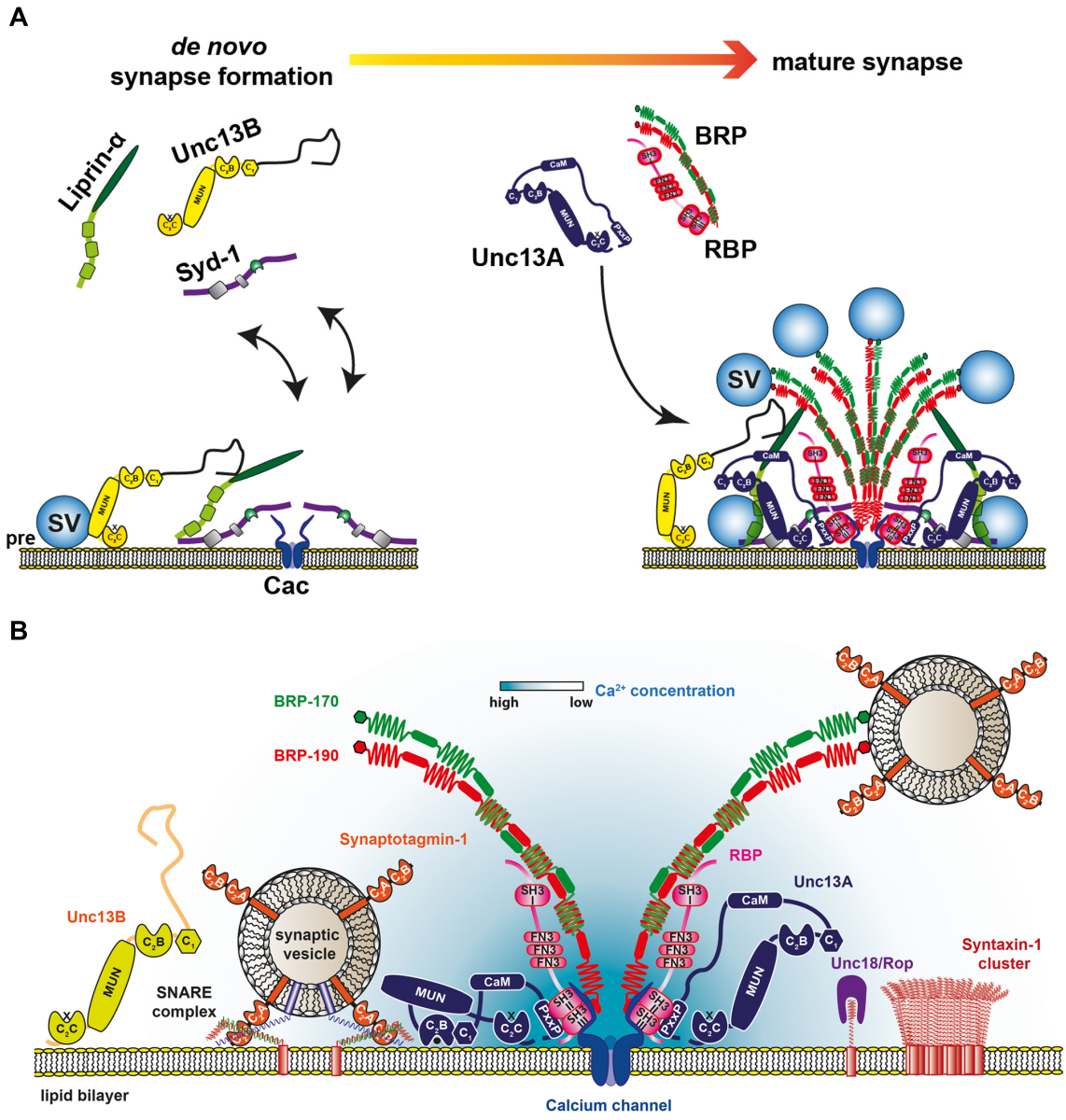

Adapted from (Böhme et al., 2016)

Fig. 9 | Illustration showing the formation of an AZ and its final form with the most important players depicted.

(A) During the process of AZ assembly, clusters of Syd-1 and Liprin-α undergo rounds of assembly and disassembly at the presynaptic membrane. Unc13B localizes to sites of de novo synapse formation via the Syd-1/Liprin-α scaffold. At nascent synapses, this induces a loose SV-Calcium channel coupling. Later during the AZ maturation process, Unc13A localizes to more mature synapses via a second, central RBP/BRP scaffold that concentrates Unc13A at the center of the AZ. Unc13A facilitates a close localization of SVs to the presynaptic calcium channels and therefore maintains a tight stimulus/secretion coupling. **(B)** Final assembly of the AZ with SV fusing to the membrane.

Axonal Transport

For the appearance of life one of the critical steps was to have a compartment that would be capable of isolating and protecting chemical reactions from the entropy of the surrounding environment. The minimum machinery to do so is the simplest living organism and it is what we call the cell. A cell is separated from the entropy from the outside by a membrane that allows cellular processes to take place (Cooper, 2000). At the same time, the cell requires compartmentalization in order to not to mix the different biological processes that simultaneously happen inside the cell. For compartmentalization membranes are again a good resource, as it is the case of the nucleus, mitochondria or the Golgi Apparatus, but as important than that is a system that can transport cellular content from one part of the cell to another, and can do it in a specific manner.

Transport of cellular content in eukaryotes is achieved by the cytoskeleton and the molecular motors. The cytoskeleton is comprised of actin filaments, microtubule and intermediate filaments. Only the microtubules will be described in this thesis because the other two are not that relevant for this work. Microtubule are polymers of tubulin dimers (alpha and beta tubulin) that form cylindrical (24 nm diameter) and long structures (up to 50 micrometers in length) (Linck and Langevin, 1981; Stephens, 1970). They are important for many cellular processes like cell division, shape maintenance and cell locomotion, and they serve also as roads or highways for transport. Microtubules reach almost every point of the cell and are polarised because of the asymmetry of the tubulin dimers. One the plus (+) end, tubulin dimers are oriented in a way that they expose their GTP binding domain motif and it is easier for another tubulin dimer to get attached to it. The plus end is therefore the growing end. On the minus (-) end, because of its conformation, tubulin dimers cannot bind so easily and is actually more probable that the tubulin dimers depolymerise (at a standard tubulin dimer concentration of the cell, 24 μM) (Cooper, 2000; Mozziconacci et al., 2008).

Axonal transport that occurs via microtubules is called fast axonal transport. There is also slow axonal transport which is independent of microtubules and Kinesin (Hurd and Saxton, 1996), but only fast axonal transport, from now on referred as axonal transport alone, will be discussed in this thesis. Axonal transport is of the utmost importance for the proper maintenance and function of neurons and its disruption has been proposed as a hallmark of several neurodegenerative diseases (Vicario-Orri et al., 2015; Julien and Millecamps, 2013). At the axon, microtubules are organized always with their plus end towards the synaptic terminal, and are used to transport cargoes, among other functions. Transport begins at the cell soma where proteins are loaded into their cargoes and bind to

the anterograde motors. How this process exactly occurs is still not fully understood. It is known that some cargoes are captured directly from the cytoplasm, like mitochondria and some proteins that do not have a transmembrane domain. Other proteins, can be loaded into their cargoes as vesicles just after exiting the Golgi Apparatus. Cargo loading into the anterograde motors requires specificity and some of it is achieved via the Golgi Apparatus sorting (Fig. 10 B) (Chia et al., 2013). After the cargoes have been loaded the long journey starts, its duration depends mostly on the length of the axon, and cargoes move at a typical speed of 1 μm/s. Because of the microtubule polarity two types of motors exist: anterograde and retrograde. Kinesins walk towards the plus end and are responsible for anterograde motion, Dyneins walk towards the minus end and are responsible for retrograde motility. Some times both motors pull the cargo at the same time, this phenomenon is known as Tug of War and is one of the mechanisms to regulate axonal transport (Müller et al., 2008; Müller et al., 2008; Müller et al., 2010). At the end of the journey, when the cargo has reached the appropriate destination the motor unloads the cargo (Fig. 10 D) (Chua et al., 2012). For proper targeting many factors regulate this process, some of them mentioned before (Fig. 9 A).

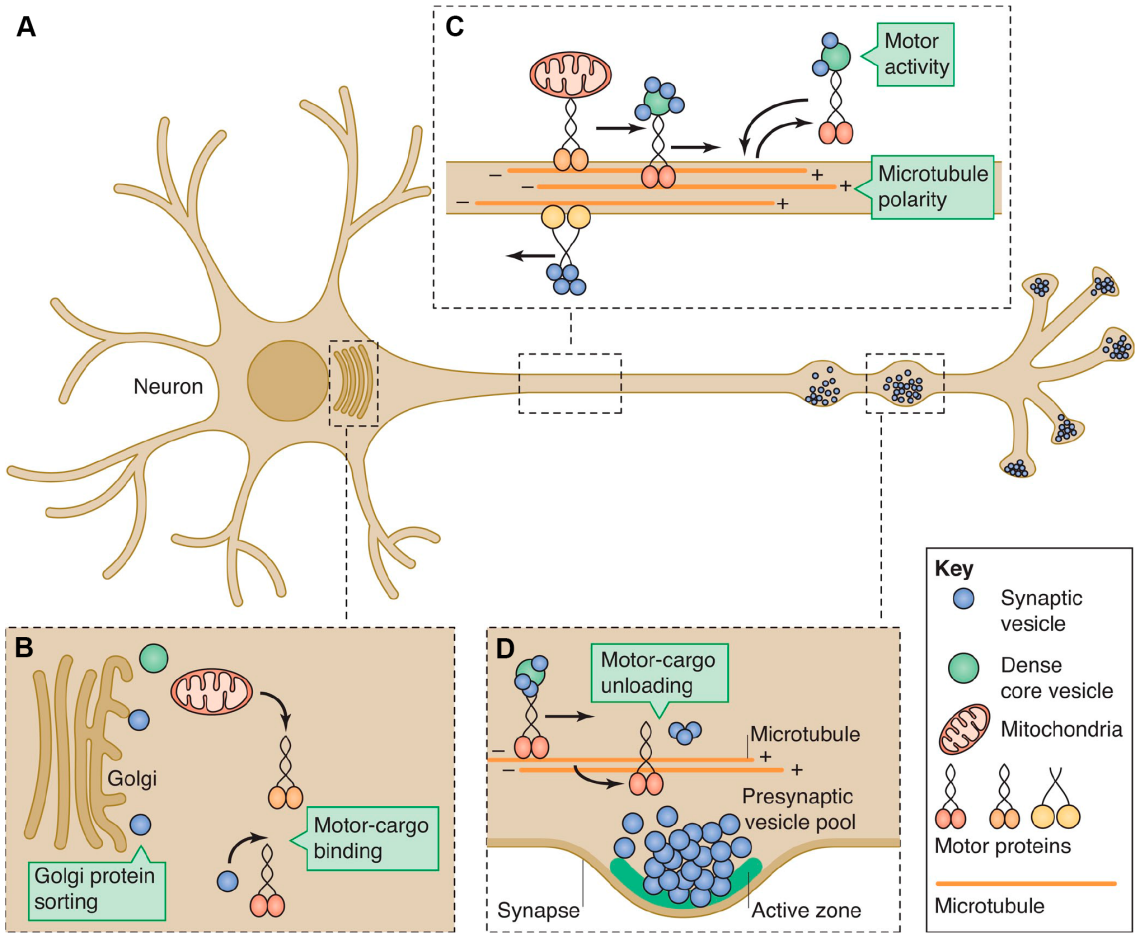

Adapted from (Chia et al., 2013)

Fig. 10 | Steps of polarized motor-based transport of synaptic material.

(A) Overview of the neuron with the most important steps highlighted. **(B)** Cargo loading from the cytoplasm or Golgi apparatus into the motor. **(C)** Establishment of proper microtubule polarity along the axon determines anterograde and retrograde trafficking by plus end– (kinesins) and minus end–directed (dynein). **(D)** At the appropriate destination, motor-cargo unloading occurs in a regulated fashion to achieve the appropriate distribution of synaptic boutons.

Motor proteins

Motor proteins are biological molecular machines that are capable of transforming energy stored in chemical bonds into mechanic work. The two most relevant families for long-range active transport are Kinesins and Dyneins. Both Kinesins and Dyneins use the polarity of microtubule to orient themselves along them and use ATP as “fuel” to move.

Dyneins

Dyneins are a group of motor proteins that form a complex with multiple and different subunits, depending on their function, their location within the cell or the organism. This multi subunit complex as a whole is sometimes refered as Dynein (in singular) and it is comparatively bigger than kinesin (Fig. 11 D) (Spudich, 2011). The first time to be described was in 1965 as a protein isolated from the cilia of *Tetrahymena pyriformis*. It was named Dynein from the greek term *dyne-* (force) and *–in* for protein (Gibbons and Rowe, 1965). Dynein thus, was first characterized to be an important protein capable of converting ATP energy into force production important for the movement of cilia in this single cell eukaryotic organism. Dynein operates by changing its conformation upon ATP hydrolysis. Later investigations found that it is via its association to microtubules that it can generate a force in the axoneme (not to be confused with the axon) (Otokawa, 1972). Moreover, by microinjecting an specific inhibitor of Dynein called EHNA[2] in axons that were isolated from the sea slug (*Aplysia californica*), it was shown that Dynein is required for fast axonal transport (Goldberg, 1982). Using the same assay but this time in axons isolated from lobsters, the group of Promersberger demonstrated that EHNA actually only blocks axonal transport in the retrograde direction (Forman et al., 1983). Dyneins are thus, the motor for retrograde axonal transport.

[2] EHNA was described by (Bouchard et al., 1981) as a drug to prevent sperm motily. It was shown that EHNA functions by selectively inactivang dynein.

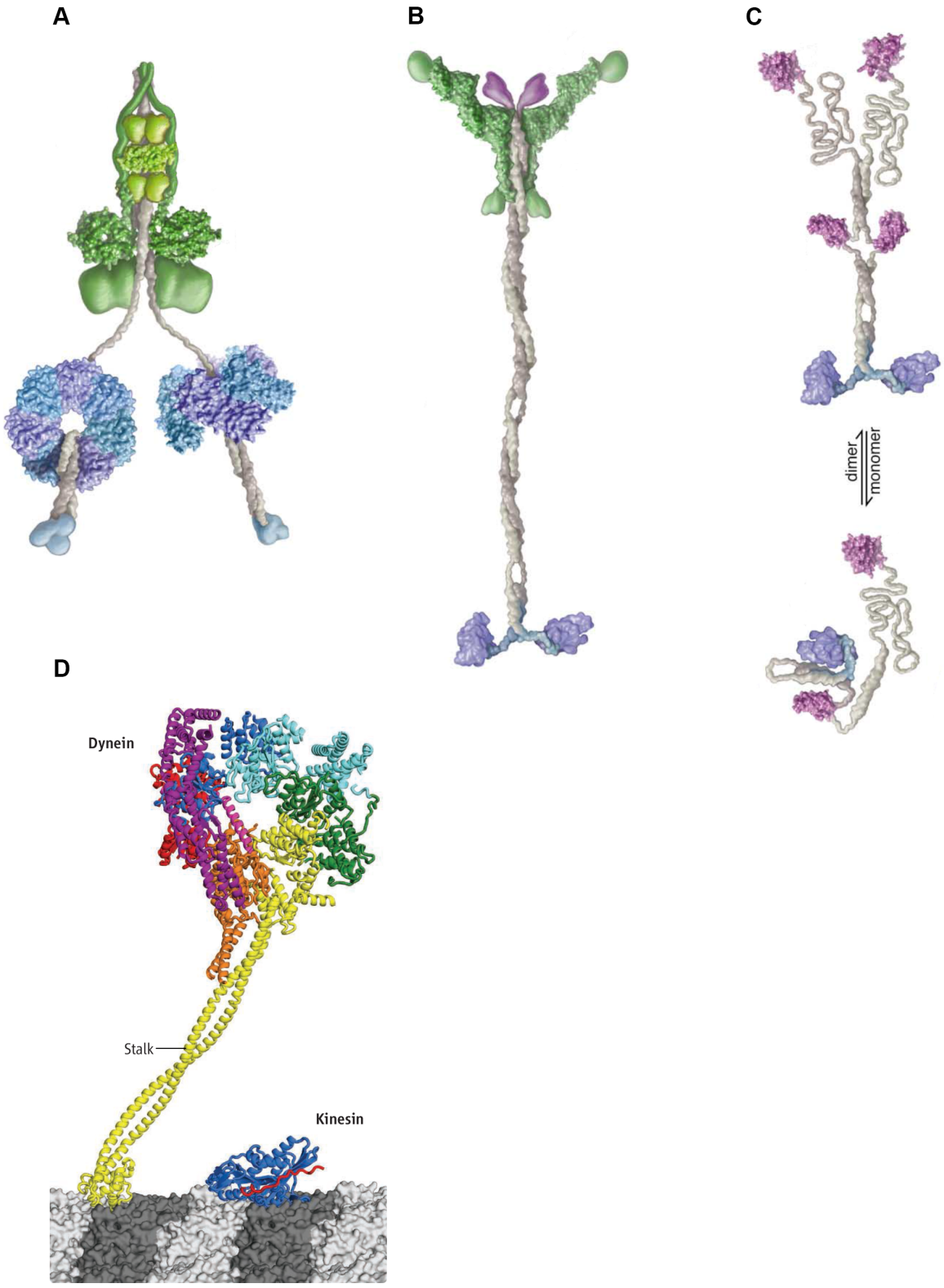

Adapted from (Vale 2003; Spudich et al., 2011)

Fig. 11 | Molecular structure of the molecular motors

(A-C) Molecular structure of Dynein, Kinesin (KHC) and Unc-104. Proteins are not to scale. Blue represents motor domains, grey the stalk, and green for associated proteins. **(A)** Dynein with all its domains: shaded blue are the MT binding domains (bottom). The ring is a globular structure where ATP is hydrolyzed. The stalk connects it further Dynein associated proteins like the Light Intermediate Chain (LIC) and the Intermediate Chain (IC) (green). IC has also a stalk that binds to dynactin, and from there to the cargo. **(B)** KHC molecular structure showing the motor domain in light blue, stalk in grey and in green the KLC. The domain that interacts with the cargo is shown in purple. **(C)** Unc-104 molecular structure showing the two known conformations: dimer (upper) activated, and monomer (bottom) inactivated. Blue shows the motor domain, in the middle purple shows the forkhead-associated (FHA) domain and upper most purple is the cargo binding domain PH. **(D)** Molecular structure of Dynein and Kinesin to scale to see how big the Dynein complex is in comparison to KHC.

Kinesins

Kinesins are a class of motor proteins that hydrolyze ATP to produce mechanical work. Kinesins are essential for the transport of a variety of cargos such as protein complexes and membranous organelles (Hirokawa and Noda, 2008). The kinesin superfamily includes 45 human genes and 25 genes in *Drosophila melanogaster*. Their classification and nomenclature was a headache until it got standardized in a recent review (Miki et al., 2005). In Drosophila, two kinesins have been characterized for axonal transport: KHC and imac.

KHC

KHC (Kinesin-1) is also known as the classical kinesin, because it was the first one identified and is therefore the founding member of the superfamily (Brady, 1985; Vale et al., 1985). KHC dimerizes and builds up what are called the two heavy chains of the Kinesin, at the same time, this KHC dimer binds to the Kinesin Light Chain (KLC) that is itself another dimer. Mammals have at least three heavy chain genes that somehow specify its function. The fruit fly and *C. elegans*, however, have only one heavy chain gene KHC (called *unc-116* in *C. elegans*) (Patel et al., 1993). Mutations of KHC in Drosophila are lethal but not before larval stage, probably because there is enough maternal KHC mRNA contribution to produce enough KHC protein until larval stages (Tsien and Wattiaux, 1971). Most evident symptoms of KHC mutations include axonal loss, motor disabilities and paralysis during early developmental stages (Franker and Hoogenraad, 2013; Saxton et al., 1991; Tanaka et al., 1998). Larvae of KHC mutants have problems crawling and their tail flips upwards indicating early paralysis of the distal muscles. KHC

mutants have an inhibition of action potentials and neurotransmitter secretion, but this is a secondary effect of the transport phenotype. KHC has been described to transport a wide range of cargoes towards the presynapse, among them SV and AZ proteins as well as mitochondria (Hirokawa et al., 2010). In the absence of functional KHC, Drosophila larvae develop dramatic focal swellings along their axon. These swellings are packed with fast axonal transport cargoes like synaptic proteins, mitochondria and prelysosomal organelles (Hurd and Saxton, 1996).

Unc-104/imac

Unc-104, also called imac (in Drosophila), is the second most relevant Kinesin for axonal transport in Drosophila. It is the homologous to the mammalian KIF1 and belongs to the Kinsein-3 family. Unlike KHC, imac has been described to be able to work as a motor also in its monomeric form in vitro. Imac null mutants are lethal at embryonic stages. Therefore the first characterization of the protein in Drosophila was done in embryos (Pack-Chung et al., 2007). Drosophila embryos lacking imac fail at forming synaptic boutons. The axons of motoneurons lacking imac could properly target the muscle cells but the terminals had very few active zones and lacked synaptic vesicle components and DCVs (dense core vesicles) (Pack-Chung et al., 2007).

More recently an hypomorph allele has been described that has allowed further characterization of the Kinesin and also its function at the larval stage (Kern et al., 2013). The hypomorph of unc-104, called bristly (unc-104^{bris}), was identified in a screen examining mutants for a synaptogenesis phenotype in the group of Tobias M. Rasse. The mutation is a single aminoacid change in the β-11 loop of the forkhead-associated (FHA) domain of unc-104. The Arginine that is at the position 561 is substituted by a Histidine (R561H). From structure based analysis of the human KIF1A it is believed that the residue Arginine in 583, also part of the β-11 loop, interacts with the E499 residue in β-1/2 loop. It is believed that this interaction stabilizes the Kinesin dimer and therefore its mutations hinder unc-104 performance (Huo et al., 2012). In contrast with the imac^{170} mutation described by (Pack-Chung et al., 2007), the hypomorph unc-104^{bris} survives to larval stages, also in transheterozygosity with the null allele (unc-104^{bris}/unc-104^{170} or also referred to as unc-104^{bris}/-). Motoneuron axons of the unc-104^{bris}/- mutants could also target the muscle, rejecting an axonogenesis problem. At the NMJ, the overall BRP intensity is severely reduced and boutons show many Post Synaptic Densities unapposed by BRP.

A

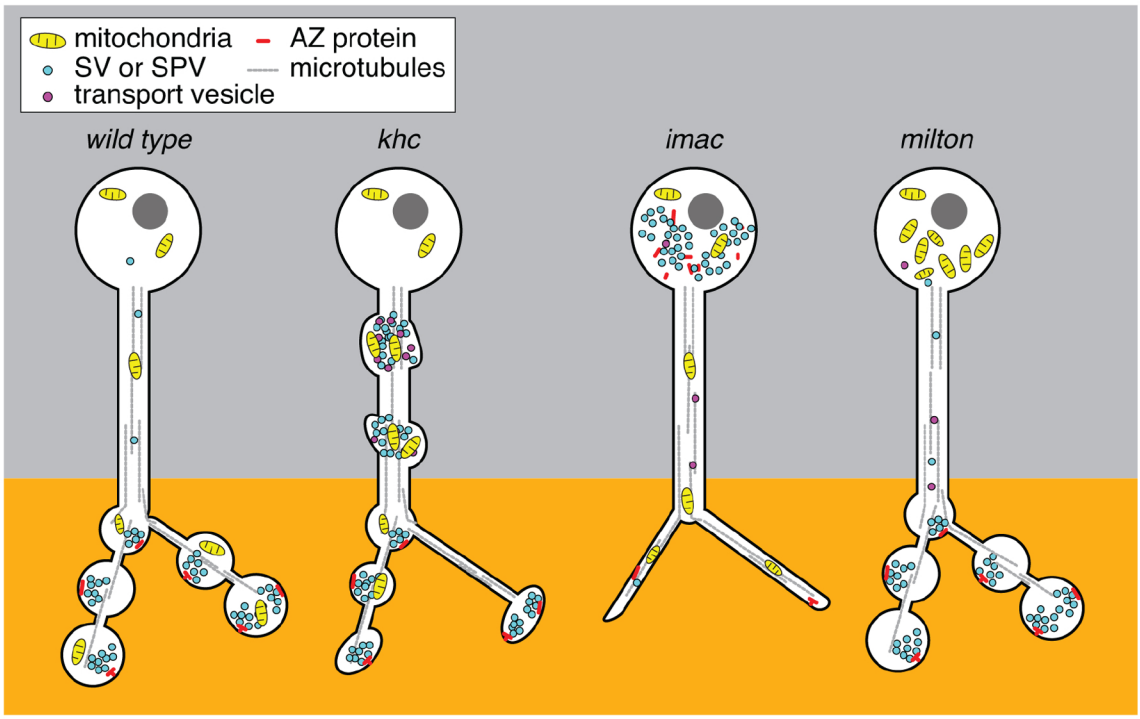

Adapted from (Goldstein et al., 2008)

Fig. 12 | Illustration and comparison of the phenotypes for KHC, imac and Milton

(A) In wild type animals the presynaptic compartment of the neuron is normally enriched with mitochondria (yellow) and SVs (blue) in close apposition to the AZ (red). Loss of the KHC, leads to accumulations of mitochondria, SPV as well as post-golgi transport vesicles in the axon. *Imac* mutants on the other hand have hardly any bouton and do not show axonal swellings, instead, the cargo is accumulated in the cell bodies. In *milton* mutants there is only accumulation of mitochondria, which cannot be shipped out and remain in the cytoplasm

Adaptors

As we have seen, in Drosophila, so far only two Kinesins have been identified to be responsible for axonal transport: KHC and imac. On the other hand, as we have discussed too, there is plenty of material that needs to be transported to the axonal terminal: AZ proteins, Synaptic Vesicle precursors, mitochondria and many other proteins. Some of them might be found only in neurons and many other that are not neuronal specific.

If two Kinesins are responsible of transporting such wide variety of cargoes, how do they achieve specificity? Specificity is of course a requirement to have different cargoes and to be able to regulate them and send them to different locations. To solve this problem Kinesins associate to a broad number of adaptor proteins that can specify cargo and regulate their function. Next we will comment on the most relevant adaptors.

KLC

Kinesin light chain (KLC) was one of the first adaptor of Kinesin to be described (Gauger and Goldstein, 1993). KLC forms a complex with the Kinesin heavy chain (KHC) to form what is also known as the native Kinesin (Fig. 11 B). KLC molecular weight is 58 kDa, around half of the molecular weight of KHC which is 115 kDa. The whole complex is composed of two molecules of each protein, resulting in a heterotetramer of 346 kDa. The *klc* gene, located on the third chromosome is widely expressed in all tissues. Gauger and Goldstein could copurify KLC and KHC even in the presence of high salt, nonionic detergens and reducing agents, proving a very strong interaction between the two proteins. Furthermore they could show that KLC interacts specifically to the tail domain of the KHC, and actually is this last portion of the KHC the one most conserved domain across species, indicating the importance of the interaction (Wong and Rice, 2010). Moreover, they could narrow down the interaction domain to a stretch of heptad repeats of the KHC tail domain that interact with the heptad repeats of KLC, being the interaction between two coiled-coil domains. In another study (Gindhart et al., 1998) the role of KLC in the axonal transport of Drosophila was better characterized by generating mutants via P-element-directed mutagenesis. The resulting klc^{1} mutant proved that KLC function is essential for Drosophila development and the phenotype reminds to a large extend to that of the KHC mutants. In fact, klc^{1} mutants are also lethal, with larvae dying between the second and third larval instars, similar to KHC mutants (Brendza et al., 1999). At the same time, and similar to *khc* mutants, klc^{1} mutants exhibit progressive paralysis during the larval stages, more prominent in the posterior muscles, reflecting a stronger phenotype for longer axons. Klc^{1} mutants also show the characteristic tail flipping phenotype common to different axonal transport mutants (Gindhart et al., 1998). The phenotype between *khc*

and *klc* mutants is so similar, and the interaction so strong that it seems unlikely that KHC can operate without the presence of KLC. The data so far acquired for both mutants suggest that the role of KLC is more to complement KHC function rather than to specificy it, e.g. restricting KHC binding to a certain subset of cargoes. In that sense, *klc*^{1} mutants could not be shown to disrupt specific pathways of axonal transport. Rather, they disrupt, as *khc* mutants do, all of the pathways for fast axonal transport so far studied. Indeed, *klc*^{1} mutants showed severe CSP and Syt-1 accumulations in the axons of motoneurons, with no apparent difference to *khc* mutants (Gindhart et al., 1998).

Milton

As we have discussed in the chapter of the axon, this very elongated structure comes along with some challenges. One of them is the energetic requirement of the synapse. Mitochondria are double membrane organelles found in all eukaryotic organisms and provide the cell with energy in the form of adenosine triphosphate (ATP). Mitochondria produce ATP via the Krebs cycle, which consists in a group of chemical reactions that oxidize the acetyl-CoA that derives from carbohydrates, fats or proteins. As a result it also produces CO_2. ATP is a small molecule that can diffuse through the cell, but not at a rate that could reach the axonal terminal in a satisfactory manner (Cooper, 2000). For that, it is very important for synaptic function that mitochondria are also transported to the synaptic terminal in order to provide with a source of energy to all the cellular processes that take place there.

In a genetic screen using eye aberration phenotypes for axonal and synaptic function genes the group of Thomas Schwarz identified a new protein and named it Milton (after the blind British poet). Flies homozygous for the *milt*^{92} null allele die at larval stage 2 (Glater et al., 2006). KHC coimmunoprecipitated with Milton and one of the two isoforms of Milton also coimmunoprecipitated with KLC. In HEK293T cells, milton selectively colocalized with mitochondria. In Drosophila larvae, milton was found in axonal and synaptic regions and in the axons the milton antibody colabeled with the marker for mitochondria Hsp60. In distal axons of first instar larvae Milton colocalized also with KHC, although KHC had a more widespread distribution and not all KHC particles were positive for milton, indicating that milton is not present in every KHC complex, but only in the subset of them that is transporting mitochondria (Stowers et al., 2002). In a more recent publication from again the group of Thomas Schwarz it was shown that milton is actually the recruiter of KHC to the mitochondria. This recruitment is independent of KLC and although a possible direct binding of the C-Term of milton to the mitochondria could not be ruled out, the anchorage is mediated by the protein miro, which is necessary to produce

proper coupling and anterograde transport of the mitochondria. Confocal stacks of the VNC of second instar larvae of the *milt*^{92} mutant, revealed apparently normal axons but completely depleted of the GFP labeled mitochondria, whereas Syt-1 was still present (Lin and Sheng, 2015; Pilling et al., 2006). This defect was selective for mitochondria, as KHC immunoreactivity was not disturbed in the mutant axons. Mitochondria were otherwise fine in the cell bodies of motoneurons, to a similar extent in *milt*^{92} mutants and control. However, *milt*^{92} also had a decrease in mitochondrial signal in the neuropile, indicating that milton is also required for proper dendritic transport of mitochondria (Fig. 12 A).

Aplip-1

In a genetic screen for KHC interacting proteins, the laboratory of William Saxton identified Aplip-1 (APP-like interacting protein1), a Drosophila homolog of JIP-1. JIP-1 (JNK interacting protein 1) had been proposed to act as linker between KHC and certain vesicles in cultured mammalian neurons. In Drosophila one single amino acid change in the Aplip-1 polypeptide chain (P483L) caused larval paralysis, axonal swellings and reduced levels of vesicle transport, anterograde as well as retrograde (Horiuchi et al., 2005). This mutation P483L is in a conserved region where Aplip-1 binds to the Kinesin Light Chain and through it to the KHC. The P483L Aplip-1 mutation is referred as Aplip-1^{ek4}. The Aplip-1^{ek4} in homozygosis has comparable severity phenotype as the Aplip-1 null, indicating that the Aplip-1^{ek4} is a very strong hypomorphic allele. However, compared to the KHC null mutants, which are lethal, Aplip-1^{ek4} survive into active and fertile adults. This indicates that Aplip-1 has a very strong relationship with KHC but it is itself not essential, probably because it contributes to a subset of the KHC functions (Horiuchi et al., 2005).

Experiments in the lab of Erika Holzbaur further defined the interactions of JIP-1 and the molecular motors in mammalian neurons. JIP-1 knockdown affected axonal transport of APP (Amyloid Precursor Protein) not only anterograde but also retrograde. To investigate whether JIP-1 can bind to Dynein and thereby, in JIP-1 absence retrograde transport gets disrupted, they performed coimmunoprecipitations of mouse brain homogenates and they could find interactions between JIP-1 and p150^{Glued}. p150^{Glued} is a subunit of the dynactin complex which is a Dynein activator. By truncating p150^{Glued} they could identify that JIP-1 binds to the C-Terminal part of it. Narrowing it down with more truncated forms of p150^{Glued}, they could more precisely identify the last 100 amino acids of the cargo-binding domain of p150^{Glued} to be responsible for the interaction with JIP-1. Furthermore, they characterized the interactions between KHC and JIP-1. Compared to the first publication (Horiuchi et al., 2005), where they described Aplip-1 to bind to KHC through KLC, the most recent publication showed that JIP-1 can bind also directly to KHC

(Fu and Holzbaur, 2013). JIP-1 has indeed a KLC binding domain at the most C-Terminal part. But in addition, it has at least two domains that bind straight to the KHC. One domain binds to the Tail of KHC, called JIP-1 TBD and the other one to the stalk, called JIP-1 SBD. Binding of JIP-1 to KHC via the TBD prevents the tail domain to fold and bind to the KHC motor domain and thereby JIP-1 blocks the autoinhibtion of KHC. Most interestingly however, is the fact that the JIP-1 SBD is in the same region as the domain that binds to $p150^{Glued}$. Taking these results together, JIP-1 can only bind Kinesin or Dynein at the same time. This is regulated via a JNK-dependent phosphorylation in the S421 residue of JIP-1; phosphorylated JIP-1 binds preferentially to KHC and non phosphorylated JIP-1 to Dynein via $p150^{Glued}$. When JIP-1 is not phosphorylated it binds to $p150^{Glued}$ via the PTB domain an activates Dynein. This, in turn, blocks the TBD of JIP-1 to bind to KHC, and the Tail domain of Kinesin can fold to bind to the Motor domain and KHC stays autoinhibited while Dynein is active.

Experiments in our group further identified the critical role of Aplip-1 in axonal transport and shed light on its direct interaction with AZ protein cargoes that are transported anterogradelly from the cell soma to the synaptic terminal (Siebert et al., 2015). In vivo imaging of whole Drosophila larvae showed that BRP and RBP are transported together in the same anterograde cargo and that this cargo is also co-transported with Aplip-1 in motoneuronal axons. Both Aplip-1 mutants, the null (*aplip-1*^{ex213}) as well as the Aplip-1^{ek4}, showed a pronounced decrease in BRP flux both anterograde and retrograde, that could be rescued with a genomic rescue construct in the *aplip-1* null background. When the axons of the *aplip-1* mutants were imaged with confocal microscopy, a very strong accumulation of BRP as well as RBP could be found. Regarding interactions, a direct binding of RBP to Aplip-1 could be established via a Yeast two Hybrid (Y2H) screen. Moreover, semi quantitative liquid Y2H assays revealed an interaction of the second and third SH3 domains of RBP with the PxxP domains of Aplip-1, which were abolished when these domains were mutated. Interestingly, no direct interaction could be shown for BRP and Aplip-1. Even if RBP and BRP are transported in the same cargo (Results Fig. 5 A) and they are in very close proximity in the AZ as well (Liu et al., 2011), it seems that their co-transport is independent of their interaction when they traffic along the axon. Removing BRP in *aplip*-1 mutants had no effect on axonal RBP accumulations, nor was the case the other way around. Hence, even a direct interaction between Aplip-1 and BRP could not be shown, it is not via binding to RBP that BRP is coupled to the Aplip-1. A possible explanation for that, could be that BRP is attached to the cargo via other AZ proteins, or other adaptors (Siebert et al., 2015).

ARFs and Arls

Arl8 is a small protein of 186 amino acids that belongs to the family of Arf-like proteins also called Arls. The Arf-like family is one of the three subgroups that form the Arf family, which consists on the Arfs, the Arls and the SARs proteins (Kahn et al., 2006). Since the discovery of the first members of the Arf family as ADP ribosylation factors (Arf), they have been found to be ubiquitious regulators of membrane traffic and phospholipid metabolism (Burd et al., 2004; Nie et al., 2003).

Arfs are soluble proteins, typically of 21 kDa, that are found in the cytosol and upon GTP binding change to their activated state and translocate to the membrane (not necessarily the plasma membrane, but also membranes from organelles). Their function at the membrane varies for each Arf member but also on the effectors to whom they associate. These are very diverse and range from coat complexes, adaptor proteins or lipid modifying enzimes (Kahn et al., 2006; Tamkun et al., 1991).

The initial factors for considering a protein as an Arf member were mainly functional. They had to fulfill three criteria: 1) they had to serve as cofactors for the cholera toxin, 2) rescue the lethal phenotype of *arf1* and *arf2* mutants in *Saccharomyces cerevisiae* and 3) directly activate Phospholipase D. Thus, when work at the group of James Kennson discovered a protein in Drosophila structurally related to Arf (60% identity) but that did not meet the before mentioned criteria, the Arf-like family was founded, being Arl1 its first member (Kahn et al., 2006; Tamkun et al., 1991).

It is of important note that although the Arf family comprises proteins with one or more specific functions or activities, this is not the case for the Arl family. Arf-like family only indicates that the protein has a structural similarity to Arf proteins. Consequently Arl proteins do not have to be functionally related to another nor are they related phylogenetically. For that reason, only Arl8, which is most relevant for the work in this thesis, will be more extensively explained.

Arl8

Arl8 exists as a single gene in the Drosophila genome as well as in *c. elegans*, and as two paralog genes in mammals, named Arl8A and Arl8B. The gene sequence identity between the human and the Drosophila Arl8 is 88%, which indicates that there has been positive evolutionary selection to preserve it.

The human Arl8a and Arl8b were first cloned by the group of Toshiaki Katada and although they observed structural similarity with the Arf family they firstly categorized it as a different family under the names of Gie1 and Gie2 (by the time of the publication the Arl family was still not very well defined) (Okai et al., 2004). In this first publication, the genes were named Gie for "GTPase indispensable for equal segregation of chromosomes" and it was described to have a major role in the proper segregation of chromosomes in mitosis. Gie mutants showed aberrant nucleus division and formation of micronucleus (Okai et al., 2004). Currently Arl8a and Arl8b are also sometimes referred as Gie1 and Gie2, or Gie alone in Drosophila, but there is consensus to group them in the Arl family, and it is more adequate to refer to them as Arl8.

As we have described before, small GTPases of the Arf and Rab families have crucial and specific roles for subcellular membranous organelles. Work from the group of Sean Munro identified Arl8 to be the small GTPase for lysosomes (Hofmann and Munro, 2006). Using COS cells and GFP and HA tags they could see that both Arl8A and Arl8B colocalized extensively with known markers of lysosomes such as CD63 and Lamp2. Both proteins showed a mild overlap with markers of the late endosomal compartments Rab7 and the mannose-6-phosphate receptor (MPR) and no colocalization at all with EEA1, which labels early endosomes (Stenmark et al., 1996). It is believed now that the localization of Arl8 at the mitotic spindle during cytokinesis could had been an artifact of the FLAG tag interfering with the localization sequence. Nonetheless it could be that there is a minor subfraction of Arl8 that localizes to mitotic structures (Hofmann and Munro, 2006).

Most members of the Arl (and Arf) family bind to the membrane via N-Terminal myristoylation and an N-Terminal amphipathic helix that inserts into the membrane upon activation. However, neither Arl8a nor Arl8b have the glycine at position 2 needed for myristoylation. Arl8a and Arl8b instead attach to the membrane through acetylation of a methionine residue located at the N-Term (Hofmann and Munro, 2006). Furthermore, it was established that the domain that allows for membrane targeting and the domain that confers lysosomal specificity are not the same ones, but two different. Replacing a single aminoacid in Arl8b (L2A) resulted in a loss of lysosomal localization and lead to a non-specific and diffuse distribution through the cytoplasm. However, it was further observed via mass spectrometry that the L2A mutant had lost the first methionine residue, a phenomenon previously documented in proteins with a small amino acid in their second position (Bradshaw et al., 1998). To see if the loss of proper localization was due to the L2A mutation or to the lack of methionine, a new mutation, L2F, was generated.

Interestingly, L2F mutants were able to protect the first methionine, which could be then acetylated and the location to lysosomes was restored. Thus, L2 is sufficient but not necessary for proper localization.

The candidate domain to mediate membrane targeting was the amphipathic alpha helix also located at the N-Terminal. Indeed, when hydrophobic residues from the helix were mutated to Alanine (I5A, L8A and F12A) to break it, Arl8b did not target to lysosomes anymore. To test if the alpha helix was just an anchor mechanism or if it conferred also specificity, the Arl8 alpha helix was replaced for the equivalent part of Arf1[3]. The Arf1 chimera now expressing the Arl8 alpha helix was not able to bind to lysosomes but it had the ability still to bind to the Golgi apparatus, demonstrating that the alpha helix is used to bind to membrane but it is the Methionine-Leucine that confers the lysosome specificity.

After showing that Arl8 binds to lysosomes, the next question to answer was, what is its function there. Lysosomes are very dynamic intracellular organelles (Heuser, 1989; Luzio et al., 2007) and their location varies depending on the nutritional state of the cell. Namely, lysosomes stay perinuclear in situations of nutritional stress (starvation) and move to the periphery when nutrients are abundant, e.g. after starvation (Korolchuk et al., 2011). Research from the laboratory of David Rubinsztein showed that Arl8B is required for proper localization of lysosomes in the cell. When Arl8B was depleted in HeLa cells using siRNA, lysosomes could not be transported to the plasma membrane and accumulated in a cluster in very close proximity to the nucleus (Korolchuk et al., 2011). On the other hand, upon overexpression of Arl8b, lysosomes moved to the periphery. The effect of Arl8 overexpression was severe to the extent, that cells which were starved (and therefore should have perinuclear lysosomes) had their lysosomes close to the plasma membrane. This result indicates that Arl8b dictates where lysosomes should be even in "contradiction" to the nutritional status, Arl8 is thus hierarchically above the nutritional status for what refers at least to lysosome positioning.

More recently, an adaptor for Arl8 has been described that sheds light into the transport phenotype of Arl8. SKIP, a protein first identified in context of response to Salmonella infection (Zhao et al., 2015) was later shown to bind to Kinesin (Boucrot et al., 2005). SKIP was also identified in an affinity chromatography with immobilized human Arl8b-GST, and their interaction was confirmed with Y2H. Moreover, it was shown that

[3] Arf1 is the Golgi GTPase and it localises at the Golgi apparatus (Hofmann and Munro, 2006).

SKIP binds to the KLC and the Arl8b-SKIP complex can then recruit Kinesin to the lysosome to promote its transport (Rosa-Ferreira and Munro, 2011).

Arl8 has been also found to interact with the HOPS complex (Homotypic Fusion and Protein Sorting). The HOPS complex is a multi-subunit complex that is found from yeast to mammals and regulates lysosome fusion with late endosomes. The HOPS complex has 6 identified units: Vps39, Vps41, Vps11, Vps18, Vps16 and Vps33 (Balderhaar and Ungermann, 2013; Khatter et al., 2015). The group of Prof. Mahak Sharma identified Arl8 to recruit the HOPS complex via the specific Vps41 subunit and proved that this interaction is required for the formation of the tethering complex with endosomes to produce endocytic degradation (Khatter et al., 2015).

Aim of the present study

Principal goal of this was to analyze mechanisms of axonal transport and protein turnover. First, degradation pathways, particularly autophagosomal machinery, was characterized by intravital imaging at synaptic terminals and axons. Having recognized that lysosomal markers did co-traffic with AZ proteins, precursor vesicles transporting AZ material towards synapses were characterized in detail.

Materials and methods

Materials and Methods

Experimental models

Drosophila melanogaster: Fly strains were reared under standard laboratory conditions and raised at 25°C and 70% humidity on semi-defined medium (Bloomington recipe). For RNAi and Arl8 overexpression experiments flies were kept at 29°C. For electrophysiological recordings, only male larvae were used, for all other experiments both male and female were used. See Key Resources Table for genotypes and strains used.

Mice: All animal experiments involving mice (C57/BL6) were reviewed and approved by the ethics committee of the "Landesamt für Gesundheit und Soziales" (LAGeSo) Berlin and were conducted accordingly to the committee's guidelines.

• Health/immune status: The animals have a normal health and immune status. The animal facility where the mice are kept is regularly checked for standard pathogens. The health reports can be provided upon request.

• Mice used for all experiments were naive. No drug tests were done.

• Sample size estimation: No estimation of simple size was done as sample sizes were not chosen based on pre-specified effect size. Instead, multiple independent experiments were carried out using several biological replicates specified in the legends to figures.

• How subjects/samples were allocated to experimental groups: Hippocampal neurons from several newborn mice of identical genotype from the same litter were pooled and analyzed. For neurons from wild-type mice neuronal cultures were randomly allocated to different treatments (drugs, transfection with plasmids etc.).

• Gender of subjects or animals: Mice from both genders were used.

• Neuronal cultures were prepared by surgically removing the hippocampi from postnatal mice at p1-5, followed by trypsin digestion to dissociate individual neurons. Cultures were grown in MEM medium (Thermo Fisher) supplemented with 5% FCS and 2% B-27. 2 µM AraC was added to the culture medium at 2 days in vitro (DIV) to limit glial proliferation. Cells were transfected at DIV 7-9 using a Calcium Phosphate transfection kit (Promega).

Method details

Molecular cloning of constructs for production of transgenic flies: cDNA encoding full length *Drosophila* Arl8 (LD29185) was obtained from Drosophila Genomics Resource Center (DGRC). Primers used for amplification and insertion into the Gateway entry vector pENTR4 (Invitrogen) are listed in the Key Resources Table.

For production of transgenic flies, the gene cassette containing Arl8 cDNA was then transferred to Gateway destination vector pTW (no tag or GFP tag) following manufacturer's instructions (Invitrogen). In brief, entry clone, destination vector and TE buffer were mixed at room temperature and incubated for 20 min. The Clonase enzyme mix was then added and the whole reaction was incubated for 1 hour at 25°C. The reaction was terminated by addition of Proteinase K for 10 minutes at 37°C. Chemically competent *E.coli* Top10 cells were then transformed and grown at 37°C. Miniprep DNA preparations of positive clones were sent for injection into w1118 fly embryos to BestGene Inc. (USA).

Co-immunoprecipitation of proteins from Hek293T cells: HEK293T cells were obtained from ATCC. Cells were cultured in DMEM with 4.5g/L glucose (Lonza) containing 10% heat-inactivated FBS (Gibco) and 100 U/ml penicillin, 100 µg/ml streptomycin (Gibco) during experimental procedures. Cells were routinely tested for mycoplasma contamination. *Drosophila* dArl8-GFP (a kind gift from Dr. Sean Munro, MRC LMB Cambridge, United Kingdom) and dUnc104/imac-myc (imac/unc-104 (clone 6-4-1, kindly provided by Dr. Thomas Schwarz Children's Hospital Boston, USA) were transfected into HEK 293T cells using calcium phosphate. 48h post-transfection cells were washed twice with ice-cold PBS, lyzed in ice cold lysis buffer (0.1% saponin, 20 mM HEPES pH7.4, 130 mM NaCl, 2 mM $MgCl_2$, 10 mNaF, protease inhibitor cocktail from Sigma) and protein concentrations were measured by Bradford assay. As input for each immunoprecipitation (IP) 3 mg total protein was used. For IP of dUnc104/imac-myc 10 µL myc-trap magnetic bead slurry (Chromo Tek, myc-TRAP®_MA) was used. Protein lysates and myc-trap beads were incubated on a rotating wheel for 2h at 4°C. Afterwards, beads were washed five times in lysis buffer, boiled for five minutes in Laemmli buffer and lysates were loaded on SDS-PAGE (8%) for analysis. Immunoblotting was done on nitrocellulose membranes. Nitrocellulose membranes were incubated with the primary antibodies at 4°C overnight. On the next day, primary antibodies were detected by goat anti-rabbit IRD800 and goat anti-mouse IRDye800 (LI-COR Biosciences, 925-32210 and 925-32211, 1:10000). Immunoblots were scanned on an LI-COR Odyssey fluorescent reader.

Immunostaining of Drosophila larvae: Larval filets were dissected and stained as previously described (Owald et al., 2010). The signal of the Cy5αHRP antibody was used as template for a mask, restricting the quantified area to the shape of the NMJ. For STED, larval filets were fixed with ice-cold methanol for 5 or 10 min (following the protocol above). Larvae were mounted in ProLong Gold (Thermofischer) or MOWIOL (SigmaAldrich).

Confocal microscopy analyses of Drosophila: Confocal microscopy was performed with a Leica SP8 microscope (Leica Microsystems, Germany). Images of fixed and live samples were acquired at room temperature. Confocal imaging of NMJs and VNC was done using a z-step of 0.25 µm. The following objective was used: 63×1.4 NA oil immersion for confocal imaging, 100×1.4 NA for STED. All images were acquired using the LAS X software (Leica Microsystems, Germany). Images from fixed samples were taken from 3rd instar larval NMJs (segments A2-A5) or VNCs. Images for figures were processed with ImageJ software to enhance brightness using the brightness/contrast function. If necessary, images were smoothened (0.5 pixel Sigma radius) using the Gaussian blur function. Confocal stacks were processed with Fiji (http://fiji.sc)(Schindelin et al., 2012). Quantifications of AZs (scored via BRP) were performed following an adjusted manual (Andlauer and Sigrist, 2012), briefly as follows. The signal of a HRP-Cy5 antibody was used as template for a mask, restricting the quantified area to the shape of the NMJ. The original confocal stacks were converted to maximal projections, and after background subtraction, a mask of the synaptic area was created by applying a certain threshold to remove the irrelevant lower intensity pixels. The segmentation of single spots was done semi-automatically via the command “Find Maxima” embedded in the Fiji and by hand with the pencil tool and a line thickness of 1 pixel. To remove high frequency noise a Gaussian blur filter (0.5 pixel Sigma radius) was applied. The processed picture was then transformed into a binary mask using the same lower threshold value as in the first step. This binary mask was then projected onto the original unmodified image using the “min” operation from the ImageJ image calculator. For sum / total intensities all intensities of the corresponding channel of one NMJ were added up, n represents the number of NMJs, For STED, deconvolution was performed with Huygens Software using the deconvolution wizard setting background value and signal to noise ratio manually.

In vivo live imaging and analysis of Drosophila larvae: *In vivo* imaging of intact *Drosophila* larvae was performed as previously described (Füger et al., 2007). Briefly, third instar larvae were put into a drop of Voltalef H10S oil (Arkema, Inc., France)

within an airtight imaging chamber. The larvae were anaesthetized before imaging with 10 short pulses of a desflurane (Baxter, IL, UAS) air mixture until the heartbeat completely stopped. Axons immediately after exiting the ventral nerve cord were imaged using confocal microscopy. Kymographs were plotted using a custom-written Fiji script (See Annexes for the code).

Immunostaining of hippocampal neurons in culture: Cultured hippocampal neurons were fixed at DIV 7.5 using 4% (w/v) paraformaldehyde (PFA) and 4% sucrose in PBS for 15 min at RT. Fixed neurons were blocked and permeabilized with PBS containing 10% (v/v) normal goat serum and 0.1% Triton X-100 for 30 min, followed by incubation with primary antibodies in 5% (v/v) normal goat serum and 0.1% Triton X-100 in PBS overnight at 4°C. Unbound primary antibody was removed with PBS while bound was detected with corresponding secondary antibodies (coupled to Alexa Fluor 488 and 647, Life technologies) for 45 min in 5% (v/v) normal goat serum in PBS plus 0.1% Triton X-100. Neuronal nuclei were visualized with DAPI (0.02 µg/mL in H_2O). Coverslips were mounted with Immumount (Thermo-Fisher).

Staining of HeLa cells: Anti-myc made in mouse (self-made, 1:200); Alexa568 goat anti mouse (Invitrogen, A11031, 1:400).

Confocal imaging of hippocampal neurons: Imaging was performed with a Zeiss Axiovert 200M equipped with the Perkin-Elmer Ultra View ERS system and a Hamamatsu C9100 EM-CCD camera under the control of Volocity software (Perkin-Elmer). Fluorescent intensities were quantified using ImageJ by the use of custom-written macros. Proximal axons were identified by ankyrin G staining.

Transfection of hippocampal neurons in culture: Neuronal cultures were prepared by surgically removing the hippocampi from postnatal mice at postnatal day 1-2, followed by trypsin digestion to dissociate individual neurons. Cultures were grown in MEM medium (Thermo Fisher) supplemented with 5% FCS and 2% B-27 and L-Glutamine. 2µM AraC was added to the culture medium at 2 days in vitro (DIV) to limit glial proliferation. Cells were transfected at DIV 3 using a Calcium Phosphate transfection kit (Promega), for knockdown of Arl8A and overexpression of Arl8B-HA. For transfection 1µg plasmid DNA, 250 mM $CaCl_2$ and water (for each well of a 12-well plate) were mixed with equal volume of 2x HEPES buffered saline (50 µL per) and incubated for 20 min allowing for precipitate formation, while neurons were starved in NBA medium for the same time at 37°C, 5% CO_2. For knock down experiments 500nM siRNA (Arl8A smart pools from Dharmacon) was additionally included and precipitated

together with the plasmid DNA. Precipitates were added to neurons and incubated at 37°C, 5% CO_2 for 30 min. Finally, neurons were washed twice with HBSS medium and transferred back into their conditioned medium.

Live imaging of hippocampal neurons in culture: Cultured hippocampal neurons were transfected with GFP-Bsn(95-3938) and Lamp1-mCherry or Arl8B-mCherry at DIV6 and used for live cell imaging at DIV9. For axonal co-trafficking, neurons were imaged in basic buffer (170mM NaCl, 3.5mM KCl, 0.4mM KH_2PO_4, 20mM N-Tris[hydroxyl-methyl]-methyl-2-aminoethane-sulphonic acid (TES), 5mM $NaHCO_3$, 5mM glucose, 1.2mM Na_2SO_4, 1.2mM $MgCl_2$, 1.3mM $CaCl_2$) using a Nikon Eclipse Ti microscope, equipped with an incubation chamber (37 °C), a 60x TIRF objective (oil-immersion, Nikon), a sCMOS camera (Neo, Andor), a 200 W mercury lamp (Lumen 200, Prior), and a dual-colour TIRF setup in epifluorescent mode (laser lines: 488 nm, 568 nm; exposure times: 200 ms each), all operated by open-source ImageJ-based micromanager software. Images were acquired with a frame rate of 2 seconds for a total time of 60 seconds. For fluorescence recovery after photobleaching (FRAP), axon terminals were imaged at DIV6 in the same basic buffer as above at a resolution of 512 × 512, with 16-bit sampling using a Zeiss LSM 710 confocal laser scanning microscope equipped with an incubation chamber (37 °C). For FRAP, the 488 nm line of the argon laser and the and 561 nm line of the DSSP laser was used in combination with a Plan-Apochromat × 63/1.40 oil DIC objective, After 10 seconds of baseline recording, both channels were bleached and a total time of 300 frames was acquired with 1 s interval.

3D-time-gated STED imaging: STED imaging with time-gated detection was performed on a Leica SP8 TCS STED microscope (Leica Microsystems) equipped with a pulsed white light excitation laser (WLL; 80 ps pulse width, 80 MHz repetition rate; NKT Photonics) and two STED lasers for depletion at 592 nm and 775 nm. The pulsed 775 nm STED laser was triggered by the WLL. Two-channel STED imaging was performed by sequentially exciting Alexa 488, Cy3 and ATTO647N at 488 nm, 568 nm, and 646 nm, respectively. Emission from Alexa 488 was depleted with 592 nm, whereas the 775 nm STED laser was used to deplete both Cy3 and ATTO647N. Time-gated detection was set from 0.3–6 ns for all dyes. Fluorescence signals were detected sequentially by hybrid detectors at appropriate spectral regions separated from the STED laser. Single optical slices were acquired with an HC PL APO CS2 100×/1.40-N.A. oil objective (Leica Microsystems), a scanning format of 1,024 × 1,024 pixel, 8 bit sampling, and 6 fold zoom, yielding a voxel dimension of 18.9x18.9 nm. To minimize thermal drift, the microscope was housed in a heatable incubation chamber (LIS Life Imaging Services).

BRP rings were measured from planar oriented Active Zones using a custom written Fiji script.

FM1-43 dye uptake in Drosophila larvae: The FM dye uptake experiment was performed following the protocol published previously (Verstreken et al., 2008). In short, 3rd instar larvae were dissected as described above and NMJs on muscle 4, segments A2 and A3 were analyzed. The larval filets were first stimulated with high K+ saline containing 4µM FM1-43 dye for 1 min and washed (3x, 5min) with Ca^{2+}-free saline. Ca^{2+} was added to extracellular haemolymph-like saline (HL-3) to a final concentration of 1.5mM (Stewart et al., 1994). For image acquisition, a 40x water immersion lens on an upright epifluorescence Olympus BX51WI microscope (equipped with a Hamamtsu Orca ER cooled CCD digital camera and a Visitron lambda DG-4 ilumination system) was used. Single optical slices of boutons were acquired and their fluorescence intensity was measured by drawing a region of interest (ROI) around boutons and subtracting the background intensity. For each NMJ a mean value was established and subsequently normalized to wild type levels. ImageJ was used for image processing and GraphPad Prism5 for statistical analysis.

Electron microscopy: Drosophila larval brains were dissected, fixed with glutaradehyde, postfixed with osmium tetroxide, dehydrated in methanol and embedded into Epoxy resin. Following polymerization, ~60 nm sections were collected and contrasted for transmission electron microscopy analysis. For tomography 3D reconstruction, ≈200 nm sections were collected on coated slotted grids, and imaged at Tecnai F20 TEM. 10 nm gold particles were used as fiducials. Tomograms were built with a help of IMOD and ETomo software. 3D reconstruction was rendered with a help of Microscopy image browser and Imaris.

For Correlative Light and Electron Microsocopy (CLEM) and immunoelectron microscopy brains were fixed in 4% formaldehyde for 20 min, stained by methylene blue cryoprotected in 2.3M sucrose and plunge-frozen on pins for Tokuyasu sectioning (Tokuyasu, 1973). For CLEM, semithin, 1µm sections were transferred to acid cleaned and silanized coverslips, stained with BRP last 200 antibodies, 488 secondary antibodies and Hoechst, mounted as a wet chamber onto slides and imaged by epifluorescence microscopy. Subsequently coverslips were retrieved and capsules with LR White resin were positioned onto brain sections. After resin polymerization, coverslips were removed and semithin sections on the surface of resulting resin block were stained by methylene blue for visibility, trimmed into a pyramid and ultrathin sectioned and contrasted. Areas of

the brain were imaged with a TEM and superimposed with fluorescent image using nuclear staining for the alignment.

For immunogold labeling, ultrathin sections were collected on coated grids, blocked and stained by BRP last 200 primary and 10 nm gold coupled secondary antibodies. After washing, sections were contrasted and covered by polyvinyl alcohol and tungstosilicic acid hydrate. Immunolabelling for gSTED imaging was performed on 150nm cryosections that were collected on acid cleaned and silanized high precision coverslips. Coverslips were blocked in PBS containing 1% BSA and 0.1M Glycine. Staining was performed with anti-BRP (last 200, 1:500) and Rabbit αSynaptotagmin-1 (1:500) followed by secondary antibodies αGuinea pig Alexa488 (Life Technologies), αRabbit Atto647N (Active Motif), Cy3αHRP antibody (Jackson ImmunoResearch 1:250) and Hoechst 33258 (Life Technologies, 5ug/ML). Samples were mounted in Prolong Gold and cured for 24h at room temperature.

Electrophysiological analysis of Drosophila larvae: Two-electrode voltage clamp (TEVC) recordings were performed essentially as previously described (Qin et al., 2005). All experiments were performed on male, third-instar larval NMJs (muscle 6 of abdominal segments A2/A3), raised on semi-defined medium (Bloomington recipe) at 25°C. Recordings were made from cells with an initial V_m between -50 and -70mV and input resistances of ≥4 MΩ, using intracellular electrodes with resistances of 10-25 MΩ, filled with 3M KCl. eEJCs were recorded at a voltage clamp of -60 mV and mEJCs were recorded at a voltage clamp of -80 mV. The eEJCs were low-pass filtered at 5kHz and sampled at 10kHz. Larvae were dissected in Ca^{2+}-free haemolymph-like solution (HL3) (Stewart et al., 1994); Composition (in mM): NaCl 70, KCl 5, $MgCl_2$ 20, $NaHCO_3$ 10, trehalose 5, sucrose 115, HEPES 5, pH adjusted to 7.2). The bath solution was HL3 containing 1.5 mM $CaCl_2$. The exemplary traces are averaged traces unless otherwise noted. The stimulation artifact of eEJCs was removed for clarity. Data were analyzed using Clampfit version 10.7.0.3. (Molecular Devices, LLC, Sunnyvale, CA, USA, 2016). Data are presented as mean ± SEM, n indicates the number of cells examined.

Experimental Design: A strategy for randomization, stratification or blind selection of samples has not been carried out. Sample sizes were not chosen based on pre-specified effect size. Instead, multiple independent experiments were carried out using several sample replicates as detailed in the figure legends.

Quantification and statistical analysis

Quantified data were analyzed using the GraphPad Prism6 software: Mann-Whitney test was used for experiments with two genotypes and one-way analysis of variance (ANOVA) for experiments with more than two. Data are reported as mean±SEM unless stated otherwise and n represents the number of samples analyzed. Significance is denoted using asterisks *P<0.05, ** P<0.01, *** < 0.001 and p>0.05 is not significant (ns).

Materials

Drosophila antibodies	Source	Identifier
Bruchpilot (Nc82), mouse, used 1:250	Developmental Studies Hybridoma Bank	
Cysteine String Protein (6D6), mouse, used 1:100	Developmental Studies Hybridoma Bank	
Syntaxin (8C3), mouse, used 1:100	Developmental Studies Hybridoma Bank	
Synapsin (3C11), mouse, used 1:100	Developmental Studies Hybridoma Bank	
Stoned B, rabbit, used 1:500	V. Haucke lab	
Dap160, rabbit, used 1:500	O. Shupliakov lab	
Glutamate Receptor IID, rabbit, used 1:500	S. J. Sigrist lab	
Vglut, rabbit, 1:500	H. Aberle lab	
Synaptotagmin, rabbit, 1:1000	BD Bioscience	

Mouse antibodies	Source	Identifier
GFP (chicken, polyclonal, used at 1:2000 in IF)	Abcam	ab13970
Ankyrin G made in mouse (used at 1:200 in IF)	Thermo Scientific	33-8800
Alexa488 goat anti chicken (used at 1:800 in IF)	Abcam	ab150169
Alexa 647 goat anti mouse (used at 1:800 in IF)	Invitrogen/ life technologies	A21235
Rabbit anti-myc (used at 1:1000 in WB)	Abcam	ab9106
mouse anti-GFP (used at 1:2500 in WB)	Clontech	632381
goat anti-rabbit IRD800 (used at 1:10000 in WB).	LI-COR Biosciences	925-32210
goat anti-mouse IRDye800 (used at 1:10000 in WB).	LI-COR Biosciences	925-32211
Anti-myc made in mouse (used at 1:200 in IF)	self-made	N/A
Alexa568 goat anti mouse (used at 1:400 in IF)	Invitrogen/ life technologies	A11031
Alexa 488 (anti-mouse/anti-rabbit), 1:500	Invitrogen	
Alexa 568 (anti-mouse/anti-rabbit), 1:500	Invitrogen	
HRP-Cy5 (conjugated antibody), 1:250	Jackson ImmunoResearch)	
Atto647 (anti-mouse) 1:500 used for STED	Atto-Tec	

Chemicals, Peptides, and Recombinant Proteins		
siRNA smart pool mouse arl8a	Dharmacon	68724

Experimental Models: Cell Lines		
HEK 293T cells	ATCC	
Hela cells	ATCC	

Experimental Models: Fly strains		
w1118 as wild type	Bloomington	
OK6-GAL4, UAS-BRP-D3-Straw (UAS-BRP is a truncated BRP from aa 473-1227)	Sigrist lab, see (Fouquet et al., 2009)	
UAS-Lamp1-GFP	Krämer lab (UT Southwestern, Dallas, TX, USA)	
UAS-BRP-D3-GFP/OK6-GAL4;	Ok6-Gal4: Bloomington # 64199	
UAS-Spinster-RFP/+;	Sweeney lab (Univ. of York, UK)	
OK6-GAL4,UAS-BRP-D3-Straw/UAS-Arl8-GFP	UAS-Arl8-GFP: Sigrist lab	
OK6-GAL4/UAS-Lamp1-GFP	as above	
Pbac(RB)Gie^{e00336}/ Pbac(RB)Gie^{e00336}	Bloomington # 17846	
OK6-GAL4/UAS-D3-Straw, Pbac(RB)Gie^{e00336}	as above	
OK6-GAL4/UAS-Arl8; Pbac(RB)Gie^{e00336}/ Pbac(RB)Gie^{e00336}	as above	
OK6-GAL4/UAS-Arl8	as above	
UAS-BRP-D3-Straw/OK6-GAL4,UAS-Rab7-GFP	UAS-Rab7: Bloomington # 42705	
UAS-BRP-D3-Straw/OK6-GAL4,UAS-Rab7-GFP	as above	
OK6-GAL4/UAS-Arl8-GFP	as above	
UAS Spinster/+, OK6-GAL4-UASDicer2/+	UAS-Dicer2: VDRC	
UAS Spinster/+, OK6-GAL4-Dicer2/+	as above	

OK6-GAL4-Dicer2/UAS-Arl8-RNAi	UAS-Arl8-RNAi: VDRC # 26085	
OK6-GAL4-UAS-Dicer2/UAS-VPS39-RNAi	UAS-VPS39 RNAi: VDRC # 40427)	
OK6-GAL4/+; Pbac(RB)Gie^{e00336}/ Pbac(RB)Gie^{e0033}	as above	
Aplip-1^{ex213}	(Siebert et al., 2015)	
UAS-Neurexin-GFP	(Owald et al., 2012)	
UAS-Neurexin-GFP; OK6-GAL4	as above	
UAS-Neurexin-GFP; OK6-GAL4; *Aplip-1*^{ex213}/*Aplip-1*^{ex213}	(Owald et al., 2012; Siebert et al., 2015)	
OK6 GAL4; UAS-ATG8-GFP	Sigrist lab	
OK6 GAL4; UAS-ATG8-mCherry	as above	
OK6 GAL4; UAS-ATG8-GFP-mCherry	as above	
OK6 GAL4; UAS-ATG8-GFP/UAS-Spinster-RFP	Sweeney lab (Univ. of York, UK)	

Oligonucleotides		
Fwd (KpnI): 5'-GACTGGTACCGAATGTTGGCCCTCATCAACAGGATCCTC-3'	MWG	
Rev (NotI): 5'-AGTGCGGCCGCCAACGACTTTGGCTTTTCGAATGTTGAATTAAC-3'	MWG	

Recombinant DNA		
Gateway entry vector pENTR4 (Invitrogen)		
pUASt-destination vector		

GFP-Basson 95-3938	Eckardt D. Gundelfinger (LIN, Magdeburg)	(Dresbach et al., 2006)
Arl8b-HA pcDNA3	This study	N/A

Software and Algorithms		
ImageJ and Fiji	(Schindelin et al., 2012)	
Other		
Built in scripts for Fiji	See Appendix	

Results

Results

Establishing kymograph analysis as a tool to quantify axonal transport from intravital imaging series

Kymographs (from greek *wave writing*) are a tool to represent the spatial coordinate over time in a 2D spatial graph, changing the time dimension to one spatial axis. Kymographs are very useful to visualize and quantify changes in position of a moving object and are therefore highly suitable for demonstrating and analyzing axonal transport.

Neurexin is a good candidate to study axonal transport because is presynaptic transmembrane protein that promotes synaptogenesis via its interaction with its postsynaptic partner Neuroligin (Muhammad et al., 2015; Owald et al., 2012). For the purpose of analyzing Neurexin axonal transport (labeled with Neurexin-GFP), two ImageJ/Fiji macros were written, the first one to convert a video recording into a kymograph, and the second one to analyze the kinetic properties of the trajectories obtained from the kymographs. Hereafter, both macros will be described. The full code together with the protocol on how to use is detailed in the appendix section.

The first macro, called “Kymograph”, converts a video recording consisting of multistacks (3 coordinates, x,y,z) into a single image, the kymograph, with two dimensions (x,y). As we are only interested in the movement of our vesicles along the “x” axis, we can discard the displacement on the “y” axis and use it to represent time. To do so, a single line is traced along the axonal path. This line is called the kymoline, and only the signal below it will be taken into account (Fig. 1 A). The next step then is to plot an intensity profile of that line over different time points (Fig. 1 B). It is important to note that the width of kymoline can be adjusted, the thicker the line is the more signal (and background) will be plotted. Ideally the line should be around the diameter of the tracking object to neither loose signal nor include too much background. Afterwards, the intensity profile is converted into an image of 1 single pixel in height and as long in pixels as the length of the kymoline.

When this process is repeated at different time points and the 1 pixel high images are stacked one under each the kymograph is formed. The dimensions of the kymograph are then as follows: height corresponds to the number of time points (stacks) the original recording had, and the length corresponds to the length of the kymoline. If the original data have a frequency acquisition comparable to the velocity of the tracking object, then

the kymograph will appear as a a continuous line (compare Fig. 1 B with Fig. 2 A). What the kymograph macro does in summary is, from a given image and a given kymoline: 1) plot the intensity profiles of every frame, 2) convert each of them into a single dimensional image, and 3) stack them together into one single image so trajectories become discernible.

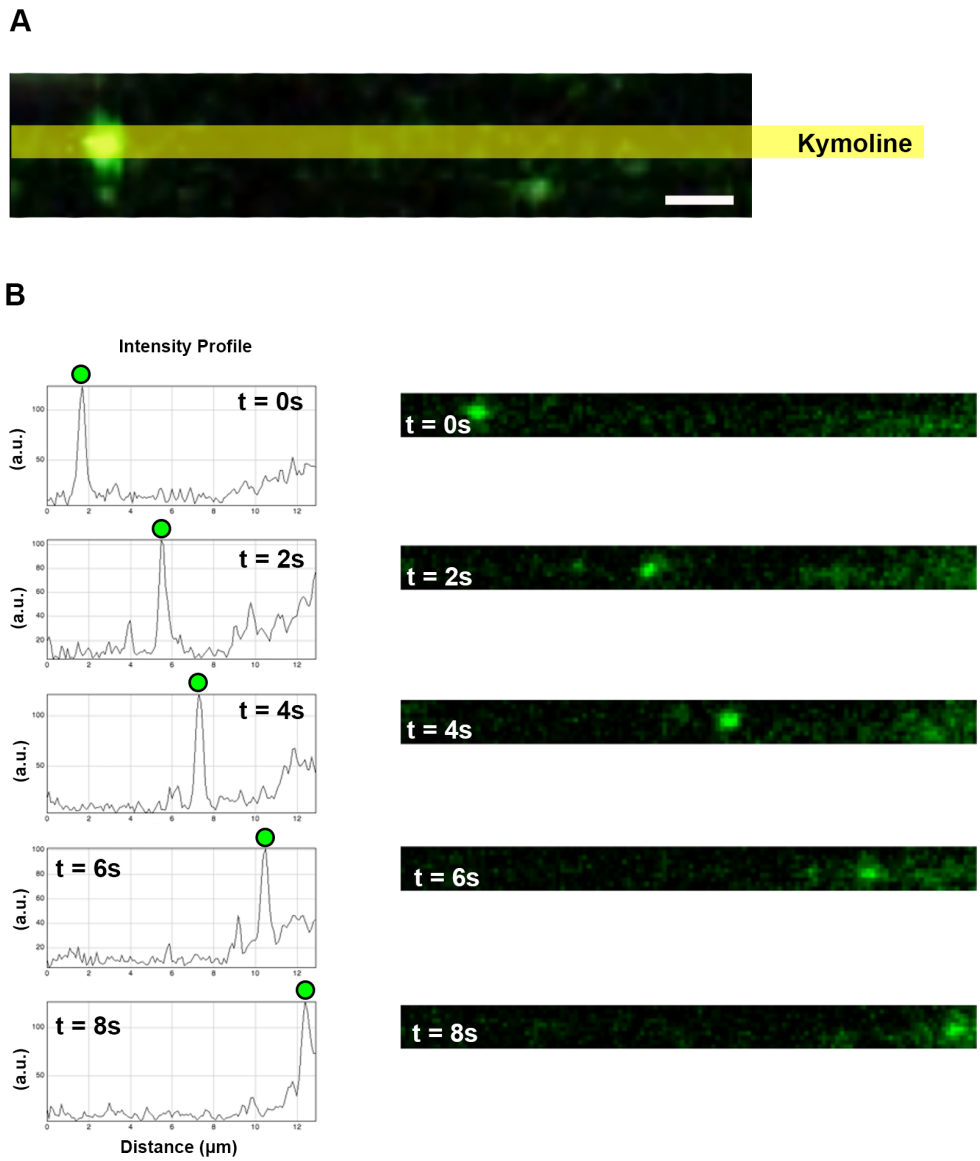

Fig. 1 | 2D representation of transport events using kymographs.
(A) Example recording of a Neurexin vesicle. First frame with the kymoline traced in yellow. Scale bar 400 nm. **(B)** Representation of the intensity profiles at different time points to show how the profiles can track the movement of the cargo (right), and how different pictures put together can give an idea of movement (left).

The second macro, called "*Velocities*", extracts all the kinetic parameters from a kymograph. The "Velocities" macro does not have the metadata for the kymograph image,

so it has to be introduced manually. By inserting the pixel size the macro will know the actual distance in micrometers from side to side of the kymograph. By adding the period of image acquisition, the macro will know what is the time difference between each horizontal line of the kymograph.

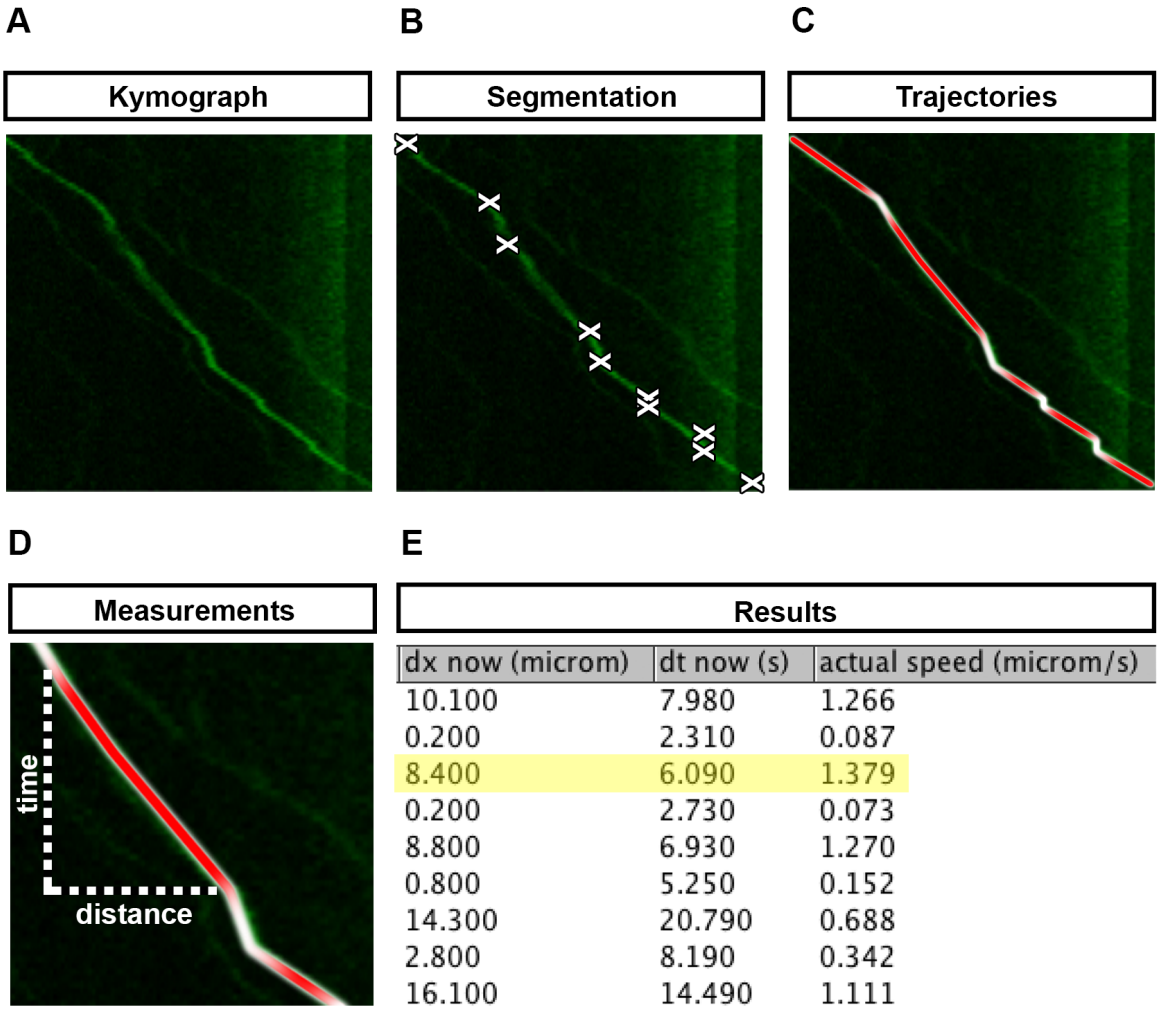

dx now (microm)	dt now (s)	actual speed (microm/s)
10.100	7.980	1.266
0.200	2.310	0.087
8.400	6.090	1.379
0.200	2.730	0.073
8.800	6.930	1.270
0.800	5.250	0.152
14.300	20.790	0.688
2.800	8.190	0.342
16.100	14.490	1.111

Fig. 2 | Measurement of velocities from a kymograph using the "Velocities" macro. **(A)** Kymograph of Neurexin transport . **(B)** Kymograph with segmented trajectories to measure the different speeds. **(C)** Different fragments of the trajectory colored for clarification. **(D)** Measurements of a Neurexin vesicle moving. The x axis corresponds to distance and the y axis to time. **(E)** Results of the velocity analysis for the depicted trajectory (A). Every row corresponds to one of the segments defined in (A). Velocity can be measured as velocity=distance/time. In yellow the segment highlighted (D), where the velocity was 1.370 micrometers/s. Note that the following segment (white), where the line was almost vertical, the velocity is close to 0 micrometers/s.

Moreover the macro cannot distinguish from anterograde or retrograde trajectories, so they have to be traced and saved separately and the direction has to be indicated.

To manually trace the trajectories the segmented line tool was used to mark every point where the trajectory changes velocity, and saved as a ROI. The code is written in such a manner that it will save all the trajectories from one kymograph image together as an output file. Consequently, all the trajectories in one direction can be saved in a single ROI file. After that, running the "Velocities" macro will give two outputs. The first one is a list of parameters (for details see Appendix), the most important are:

- dx now (microm): Distance in micrometers between two points of the same trajectory
- dt now (s): Time diference in seconds between the two points of one trajectory
- actual speed (microm/s): Given velocity at the interval of time between two points

These three parameters are given for every segment of one trajectory (Fig. 2 E).

The second output file contains the ROI ID, the total time the trajectory has been traced within the kymograph and the average speed. In addition, it contains the total number of trajectories per kymograph, and their relative frequency, that is, how many vesicles have been traced during the total time frame of the kymograph (Appendix).

Neurexin axonal transport is slowed down in *aplip-1* mutants

After the publication from our lab describing the role of the transport adaptor Aplip-1 in axonal transport (Siebert et al., 2015), we wanted to investigate whether Neurexin transport was disrupted in *aplip-1* mutants. After in vivo imaging Neurexin transport in *aplip-1* null mutants we could see that its transport was indeed severely affected, showing many partially stationary vesicles. We then performed analysis of the trajectories to compare velocity distributions in control and mutant animals. By just visual inspection, it seemed that in general Neurexin trajectories were "slower" in absence of Aplip-1. By analyzing many trajectories using the code described previously (See Appendix), we were able to obtain enough quantitative data to make a comparative analysis (Fig. 3 A-B).

The first observation of this analysis was that although the mean velocity for anterograde and retrograde Neurexin was 1 µm/s, the distribution was quite wide and

ranged from 0.2 to 3 µm/s [4]. As explained in the introduction, Aplip-1 can bind Dynein as well as Kinesin, but not simultaneously. By completely removing Aplip-1 one could expect to see anterograde and retrograde transport being affected to the same extend. It could also be possible, that Aplip-1 function was more important for one of the motors (Kinesin or Dynein) and in the mutant situation the equilibrium would be disrupted in favor of the other motor.

Our results revealed two things. First, *aplip-1* mutants showed an important reduction of Neurexin velocities for both anterograde and retrograde cargoes. The frequency distribution was in both cases shifted to velocities closer to 0 (Compare Fig. 3 A and B, and C with D). Second, there was an increase of non-moving trajectories. In control axons, Neurexin trafficking remained static around 20% of the time in both anterograde and retrograde, and only rarely showed (<5%) changes in direction (Fig. 3 E-F). However, in the absence of Aplip-1 this was severely affected. To start with, it was no longer always possible to categorize cargoes as anterograde or retrograde, because there were many stationary vesicles. Therefore, we defined a criterion to be able to compare them: trajectories that had an overall anterograde displacement greater than 10 µm were classified as anterograde cargoes, and vesicles which moved longer distances than 10 µm in retrograde mode were categorized as retrograde (trajectories that had a lower displacement than 10 µm were not analyzed). After doing so, we quantified for how long each group was not moving. We found that anterograde trajectories were stationary for almost 50% of the time (Fig. 3 E) and more than 50% for the ones classified as retrograde (Fig. 3 F). The absence of the Aplip-1 appeared to have a mild effect also on the probability of changing direction. This was more clearly seen in anterograde transport where the *aplip-1* mutants showed retrograde motion (-) around 7% of time, even if this hardly occurred in control situations.

Taken together, these results demonstrated a role of Aplip-1 in the regulation of both anterograde and retrograde transport. Moreover, our data indicated that Aplip-1 regulates the transitions between anterograde and retrograde trafficking, which is in accordance with previous results obtained for the mammalian orthologue JIP-1 (Fu and Holzbaur, 2013). Further experiments could investigate how exactly the transitions between anterograde and stationary movement are affected. Do interruptions of anterograde motion occur more often or they occur at the same frequency but vesicles remain for longer times static? A combination of both mechanisms could explain our

[4] Trajectories between +0.2 and -0.2 µm/s were considered stationary and therefore out of analysis.

reliminary results, but additional and more detailed examination is required. Quantifying the run length of the trajectories as well as the duration of the breaks and comparing them between control and *aplip-1* null will enable a deeper understanding of this process.

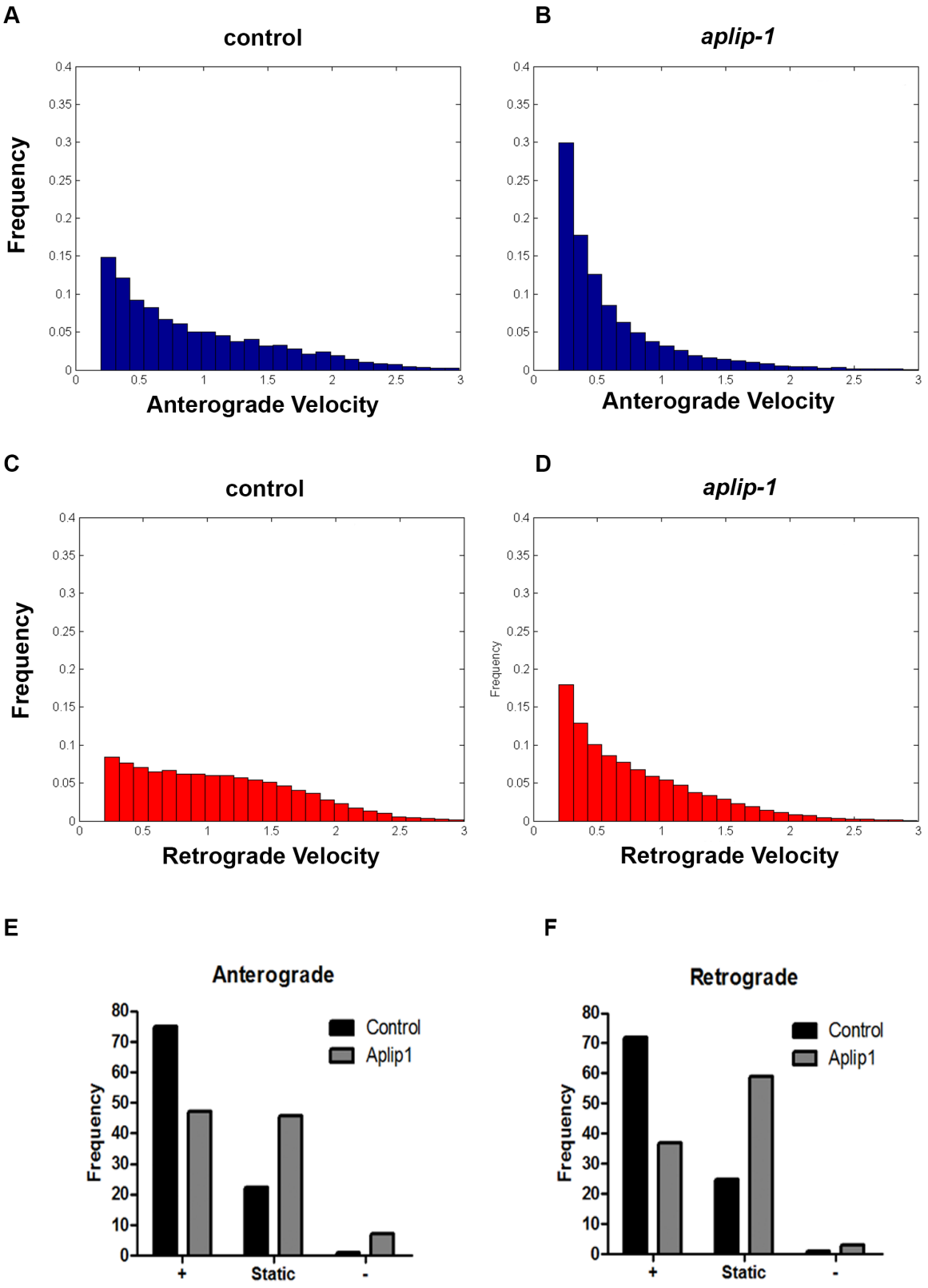

Fig. 3 | Neurexin in vivo transport is severely slowed down in absence of the Aplip1 transport adaptor.

Analysis of Neurexin-GFP transport in axons of third instar larvae. Comparison of the kinetic parameters between control (OK6; UAS-Neurexin-GFP) and *aplip-1* null (*aplip1*^{ex213}/*aplip1*^{ex213}) **(A)** Frequency distribution of anterograde velocities in control flies (n=6). **(B)** Frequency distribution of anterograde velocities in *aplip-1* mutants (n=6). A shift towards slower velocities can be clearly observed. **(C-D)** Frequency distribution of anterograde velocities in control flies and aplip-1 mutants revealing a shift towards slower velocities (control n=6, *aplip-1* n=6). **(E-F)** Categorization of the trajectories in different modes revealed very similar distribution between anterograde and retrograde but disruption in *aplip-1* mutants. Velocities were considered positive (+) if they moved forward at a speed above 0.2 µm/s, negative (-) below -0.2 µm/s, and static between 0.2 and -0.2 µm/s. **(E)** Comparative categorization between control and *aplip-1* mutants shows how stationary and negative trajectories are increased in *aplip-1* background, whereas positive are severely reduced (n=6). **(F)** Retrograde trajectories of Neurexin-GFP are predominantly forward in control situation, but predominantly stationary in the absence of Aplip-1 (n=6).

Axonal transport of synaptic proteins and degradative compartments: an intravital analysis

An increase in autophagy protects from age-induced memory impairment. In order to get a better understanding of how AZ proteins could be degraded we used the in vivo imaging setup described in the materials and methods to characterize the axonal transport of several proteins of degradative compartments (Füger et al., 2007). These included:

- Lamp1 and Spinster, two marker proteins of lysosomes (Rohrer et al., 1996; Sweeney and Davis, 2002)
- Rab7, a marker of late endosomes (Bucci et al., 2000; Zhang et al., 2009)
- ATG8, marker for autophagosome (Geng and Klionsky, 2008; Mochizuki et al., 2011; Toda et al., 2008).

Some of the questions we wanted to answer were: To what extent are these proteins found in neurons? Are they only in the cell bodies of motoneurons or do they also reach the synaptic terminal? If so, how are they transported? Are they transported anterogradely, retrogradely or both? Can this transport be analyzed? How do these

different degradation proteins interact with each other? And most importantly, how do they interact with the AZ proteins?

After imaging the before mentioned proteins, we saw that all of them showed bidirectional transport in the axons of motoneurons (Fig. 4 A-D). Most interestingly, the transport of proteins from the recycling pathway did not differ much from the transport of synaptic proteins like Neurexin, Bruchpilot or Synaptotagmin-1 (Fig. 4 F-H). With the exception of ATG8-GFP, all these proteins showed bidirectional transport. More frequently, Rab7, Spinster and ATG8 would also have non-moving cargoes (visualized in the kymographs as vertical lines)[5] but this was also observed for the Nrx, BRP and Syt-1, albeit less frequently. Of special interest is the fact that ATG8 could only be seen transported in the axon when labeled with the red fluorophore mCherry (Fig. 4 D). ATG8-GFP could not be observed moving in the axon (Fig. 4 E). This construct is designed in such a manner that the GFP is located in the luminal compartment of the autophagosome so that it can report acidification (Fig. 7 B). Thus, we concluded that autophagosomes that are transported along the axon are acidified. The same was expected for the Lamp1-GFP construct, which has been designed and used in the past to monitor non functioning and therefore non acidic lysosomes (Pulipparacharuvil et al., 2005; Rohrer et al., 1996). However, we observed abundant bidirectional transport of GFP-positive Lamp1-cargoes, indicating that at least a fraction of Lamp1 is transported in non-acidified compartments (Fig 1. A).

[5] For references on how kymographs were produced or quantified see the Appendix.

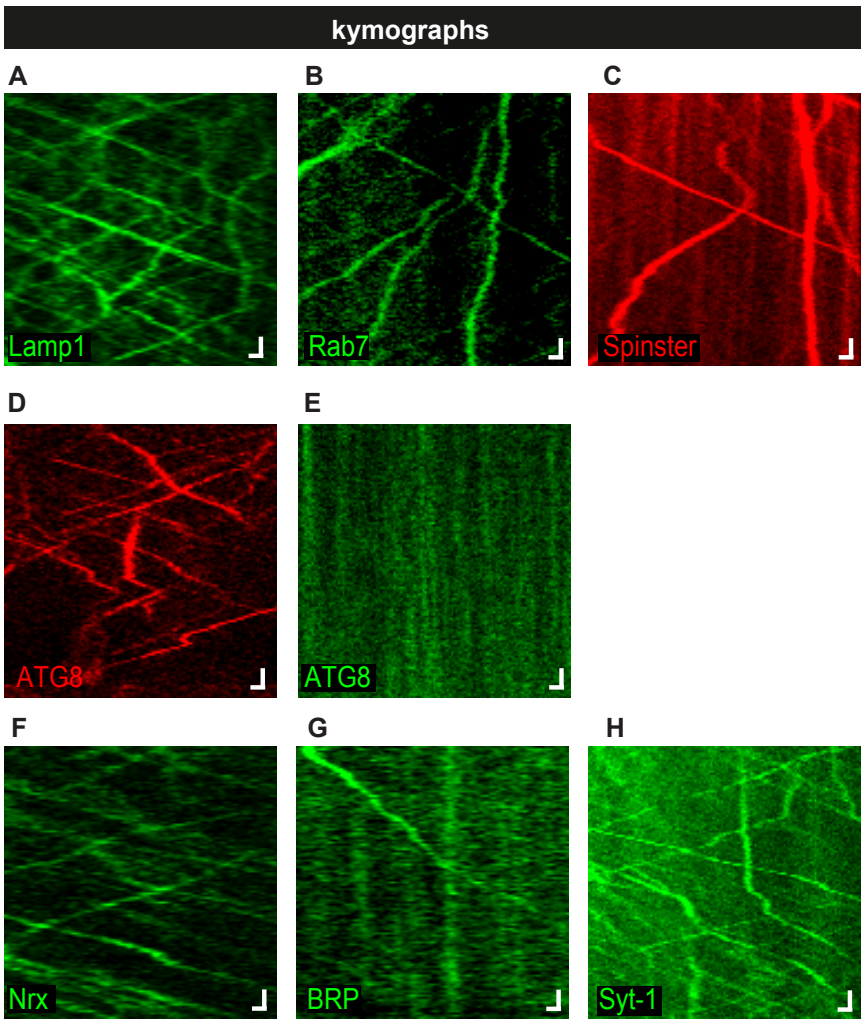

Fig. 4 | *Intravital imaging of* Axonal transport of degradation markers and synaptic proteins.

Live confocal imaging of motoneuron axons of intact Drosophila 3rd instar larvae expressing markers of the recycling pathways as well as synaptic proteins. **(A)** Kymograph of Lamp1-GFP (marker of lysosomes) positive cargoes moving along the axon of motoneurons. **(B)** Rab7-GFP (marker of late endosomes) cargoes moving along the axon in both directions and with some stationary vesicles not moving. **(C)** Kymograph of Spinster-RFP labeled lysosomes being transported along the axon in both directions and with stationary lysosomes. **(D-E)** Kymographs of ATG8 **(**marker of autophagosomes) with mCherry (D) or GFP (E). Note that in D there is transport of autophagosomes in both directions whereas with ATG8-GFP no trajectories could be observed because acidified autophagosomes bleach the GFP. **(F)** Kymograph showing the trajectories of the transmembrane protein Neurexin-GFP, **(G)** the AZ scaffold protein BRP tagged with GFP and **(H)** the SV protein Syt-1. Scale bars: 2 µm and 2 s.

In vivo analysis of AZ protein axonal co-transport

The AZ cytomatrix is composed of several proteins that are assembled together in order to allow synaptic transmission (Wilhelm et al., 2014). Before AZ scaffold components arrive at synapses these proteins need to be transported along the axon (local translation at the presynapse could also be important (Akins et al., 2009; Kim and Jung, 2015; Liu-Yesucevitz et al., 2011). In order to understand whether AZ proteins were transported in a pre-assembled state, we investigated whether AZ components would be co-transported within axons towards synaptic terminals. To do that we tested Unc13A, Unc13B and RBP co-transport with BRP. Positively, we were able to identify 2 principal components of the AZ to co-transport with BRP.

RBP and Unc13A have been reported to be in close proximity to BRP in the AZ, however, it was unclear whether they are co-transported together or whether they instead arrive separately at synaptic terminals with their already assembled AZ. Our kymographs showed clear evidence that RBP and BRP are anterogradelly co-transported, obviously forming a common cargo (Fig. 5 A). No co-transport events could be observed for Unc13B (not shown), which could be because they are transported separately or becausewe were not able to see it. Instead, when combination of Unc13A and BRP was tested, cotransport was observed (Fig. 5 B). This indicated that Unc13A, RBP and BRP are transported in preassembled functional units.

In *C. elegans*, SV and AZ scaffold proteins have been shown to undergo extensive co-transport (Wu et al., 2013). In mice, AZ and SV proteins previously have been postulated to be axonally transported either as pre-assembled clusters (Bury and Sabo, 2011; Tao-Cheng, 2007) or in distinct vesicular structures with (Shapira et al., 2003) and without an electron-dense core of unknown cell biological identity (Maeder et al., 2014; Yonekawa et al., 1998). To resolve this important issue in our preparation, we first tested whether or not AZ and SV proteins were co-transported. We monitored the axonal transport of the presynaptic AZ scaffold Bruchpilot (BRP, a large multidomain protein that couples release-ready SVs to presynaptic calcium channels (Hallermann et al., 2010; Kittel et al., 2006a; Kittel et al., 2006b) and of the essential SV calcium sensor Synaptotagmin 1 (Jahn and Fasshauer, 2012; Südhof, 2013; Zhou et al., 2017), in live *Drosophila* larvae. We generated transgenic flies co-expressing red fluorescent protein-tagged truncated BRP, this labels the endogenously transported BRP (Petzoldt et al., 2014) together with Synaptotagmin 1-GFP (Zhang et al., 2002). Anterogradely moving BRP punctae in most cases contained Synaptotagmin-1 (Fig. 5 C). AZ and at least some SV proteins are, thus, co-transported in axons of *Drosophila*.

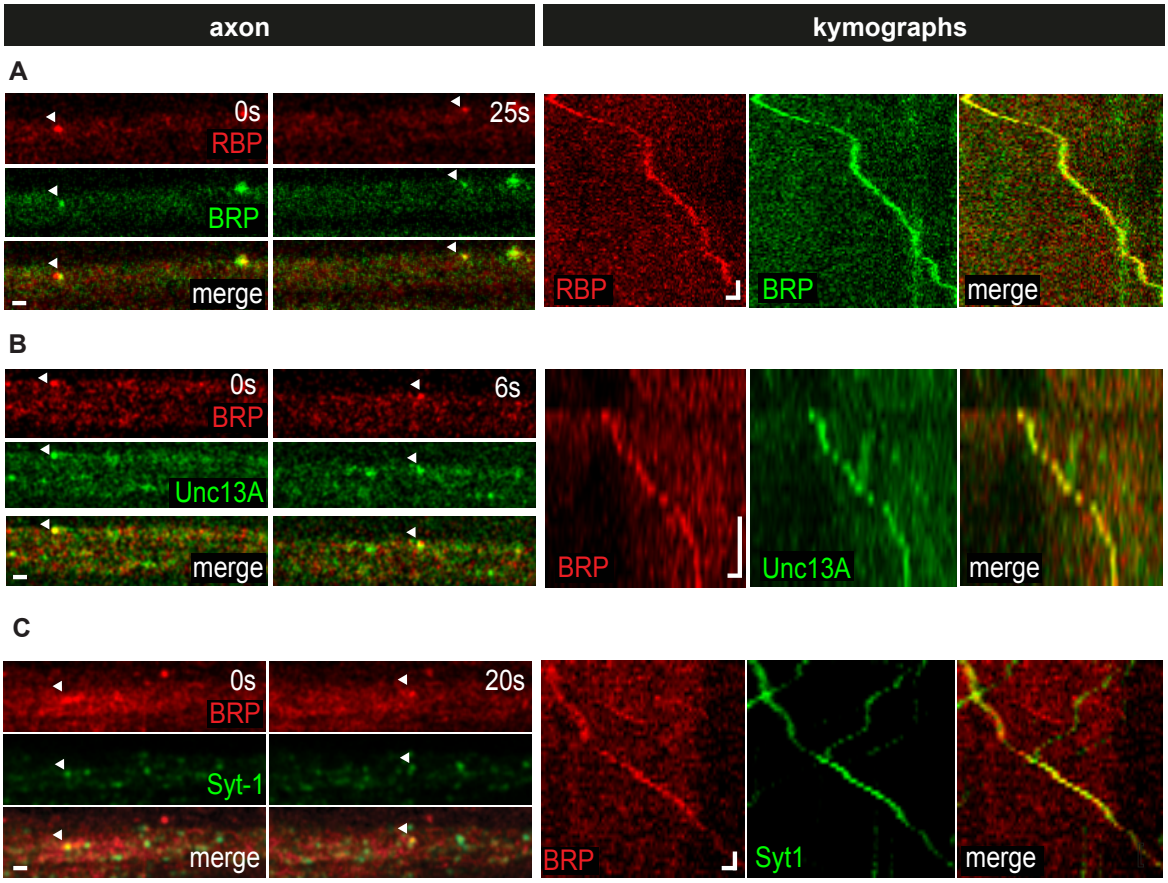

Fig. 5 | Co-transport of AZ component with SV proteins

(A) Stills (left) and kymographs (right) showing co-transport of RBP and BRP. **(B)** Stills (left) and kymographs (right) showing a co-transport event between BRP and Unc13A. **(C)** BRP and Syt-1 (marker of SV) co-transport together in anterograde cargoes (stills left, kymographs right). Scale bar single frames 2 µm, kymographs 2 µm and 2 s.

Autophagosomes form, fuse with lysosomes and acidify at the synaptic terminal

Our hypothesis was that the late endosomal-lysosomal pathway might play a role in recycling AZ material. To address whether this would be case, we co-expressed markers of the recycling pathway together with AZ proteins. To do so we concentrated on retrograde cargo, understanding that at least some of it corresponds to proteins that are being recycled. To test the late endosomal branch we used Rab7, which is an established marker of late endosomes (Bucci et al., 2000; Harrison et al., 2003; Zhang et al., 2009). We could identify retrograde BRP being transported in Rab7 positive cargoes (Fig. 6 A). Most interestingly we were able to observe some lysosomal markers transporting with anterograde BRP (Fig. 8) (This unexpected result is discussed more in detail in the following chapter.)

To continue understanding the relationship between the degradation pathway and AZ protein recycling, we analyzed the autophagosome reporter ATG8-GFP at NMJ terminals by intravital imaging. As mentioned before, no axonal transport of discrete ATG8-GFP positive cargo could be observed, consistent with the idea that axonal transport of ATG8 might happen at acidic compartments (Fig. 4 D-E). The ATG8-GFP signal at the NMJ was equally diffused GFP at the terminal (Fig. 6 A, min 0).

However, upon recordings of 10min, among the disperse GFP signal some punctuated structures could be observed at the terminal (Fig. 6 B, 9min). This newly formed autophagosomes were mostly immobile and therefore appear as vertical lines in kymographs (Fig. 7 A). Longer recordings gave more information about their dynamics. After formation, autophagosomes typically remain quiet for periods of times between 5 to 30 minutes. Some of these autophagosomes disappeared during the recordings (Fig. 6 B, min 20, min 22), and we hypothesized that this could be due to the acidification of the autophagosome, resulting in GFP quenching.

To test that, we co-expressed ATG8-GFP with Spinster-RFP as a marker of lysosomes (Sweeney and Davis, 2002). By time lapse imaging of NMJ terminals for time lapses of 30 minutes, some Spinster-RFP positive vesicles could be observed entering the terminal. After entering the terminal, the lysosome moved anterogradelly until eventually fusing with one autophagosome, labeled with ATG8-GFP. Multiple events of fusion could be observed with the same autophagosome (Fig. 7 A). These fusions occurred not only with the most proximal autophagosome (and therefore the first one to be encountered) but instead lysosomes could bypass (or miss) several autophagosomes before fusing with one (Fig. 7 A). Upon fusion with Spinster, the autophagosomes GFP signal decreased (Fig. 7 B), indicating that at least some Spinster-RFP is labeling acidified lysosomes. After fusion and acidification, autophagosomes entered retrograde motion at slow speeds and with low processivity (not shown), an observation that to some extend fits the reports of the group of Prof. Erika Holzbaur (Fu and Holzbaur, 2013).

We next co-expressed BRP together with AT8-GFP to see if similar events of colocalization (as in Rab7, Fig. 6 A) could be observed. The lack of visible ATG8-GFP axonal transport made it impossible to visualize retrograde axonal co-transport, and although BRP and ATG8-GFP were imaged at the NMJ for periods of time of 30 minutes, red signal inside the autophagosomes could not be observed (not shown). Further experiments are needed to better understand how degradation of AZ proteins occurs and their relationship with the autophagosomal-lysosomal pathway.

Finally, we analyzed the acidification behavior of autophagosomes in more detail. Here, we used the ATG8 co-labeled with GFP and mCherry. By measuring the ratio of GFP to mCherry signal we could determine how acidification occurs (Fig. 7 B-C). Our results showed a slow acidification of autophagosomes that lasted between 20 to 45 minutes before GFP signal was not visible anymore (Fig. 7 B). This process, we speculate, correlates with the fusion of acidic lysosomes that could be observed previously (Fig. 7 A). It is worth mentioning that in some occasion autophagosomes "dissolved" without apparent fusion of lysosomes (Fig. 7 A, middle vertical line), suggesting that the formation of an autophagosome can be reverted at some point. These data in part are still preliminary but show the potential of *in vivo* imaging for monitoring degradation at the NMJ, and future experiments will hopefully help understand these very relevant mechanisms in more detail.

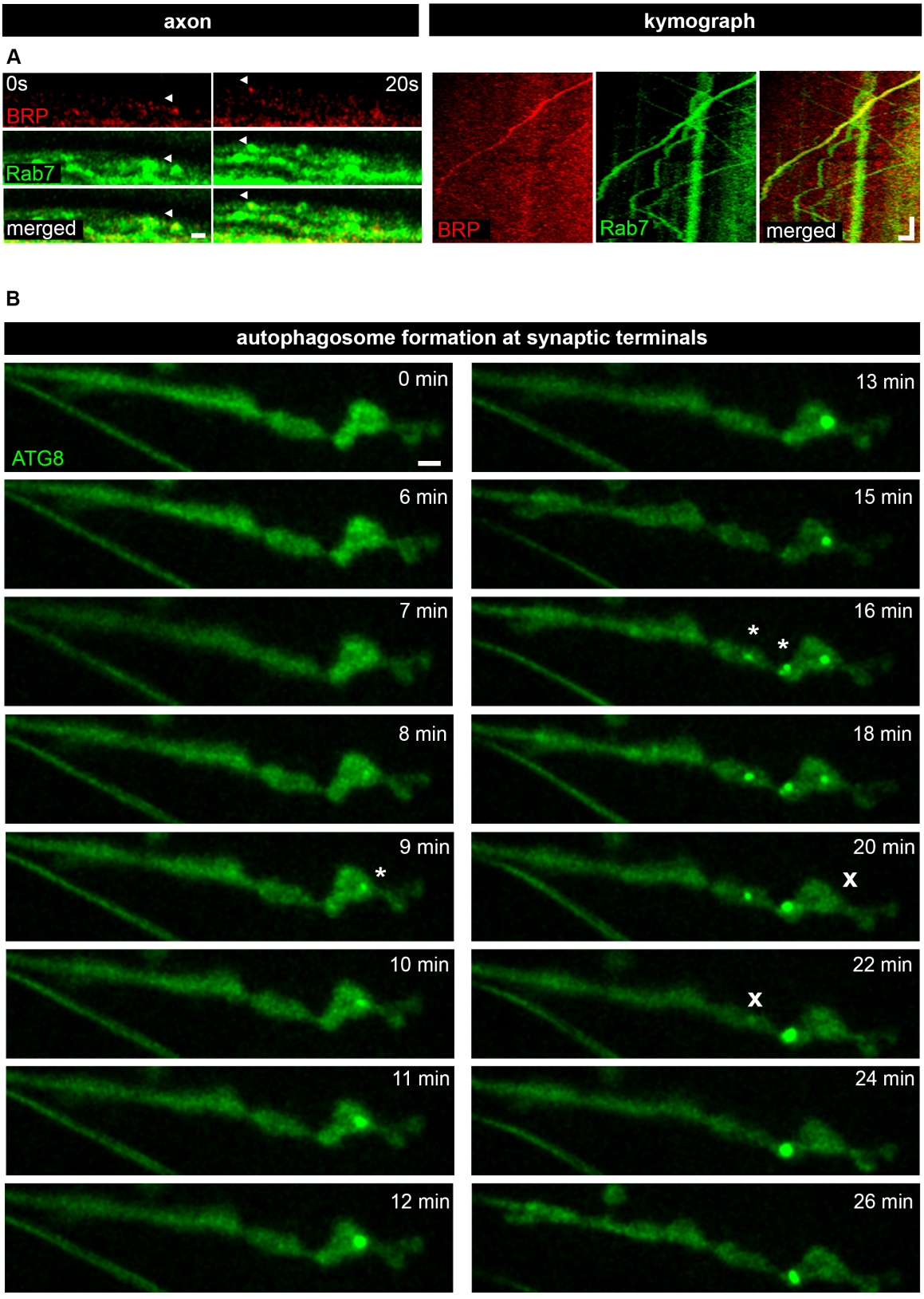

Fig. 6 | BRP co-transports with Rab7 and autophagosome forms at NMJ terminal

(A) Kymograph of Rab7-GFP (marker of late endosomes) positive cargoes moving retrogradelly along the axon of motoneurons together with BRP. Scale bar single frames 2 µm, kymographs 2 µm, 3 s. **(B)** Autophagosome formation at the synaptic terminal. 16

images showing the process of autophagosome formation by imaging ATG8-GFP. After around 10 minutes of in vivo recording muscle 26 of 3rd instar larvae expressing ATG8-GDP under motoneuronal driver, formation of autophagosome coul be observed (min 9, asterisk). The autophagosome was visible during 10 minutes after which the signal decreased because of acidification (min 20, cross). During the time other autophagosomes formed in the same terminal (min 16, asterisks), and collapsed (min 22, cross) or stayed visible for longer times. Scale bar 3 µm.

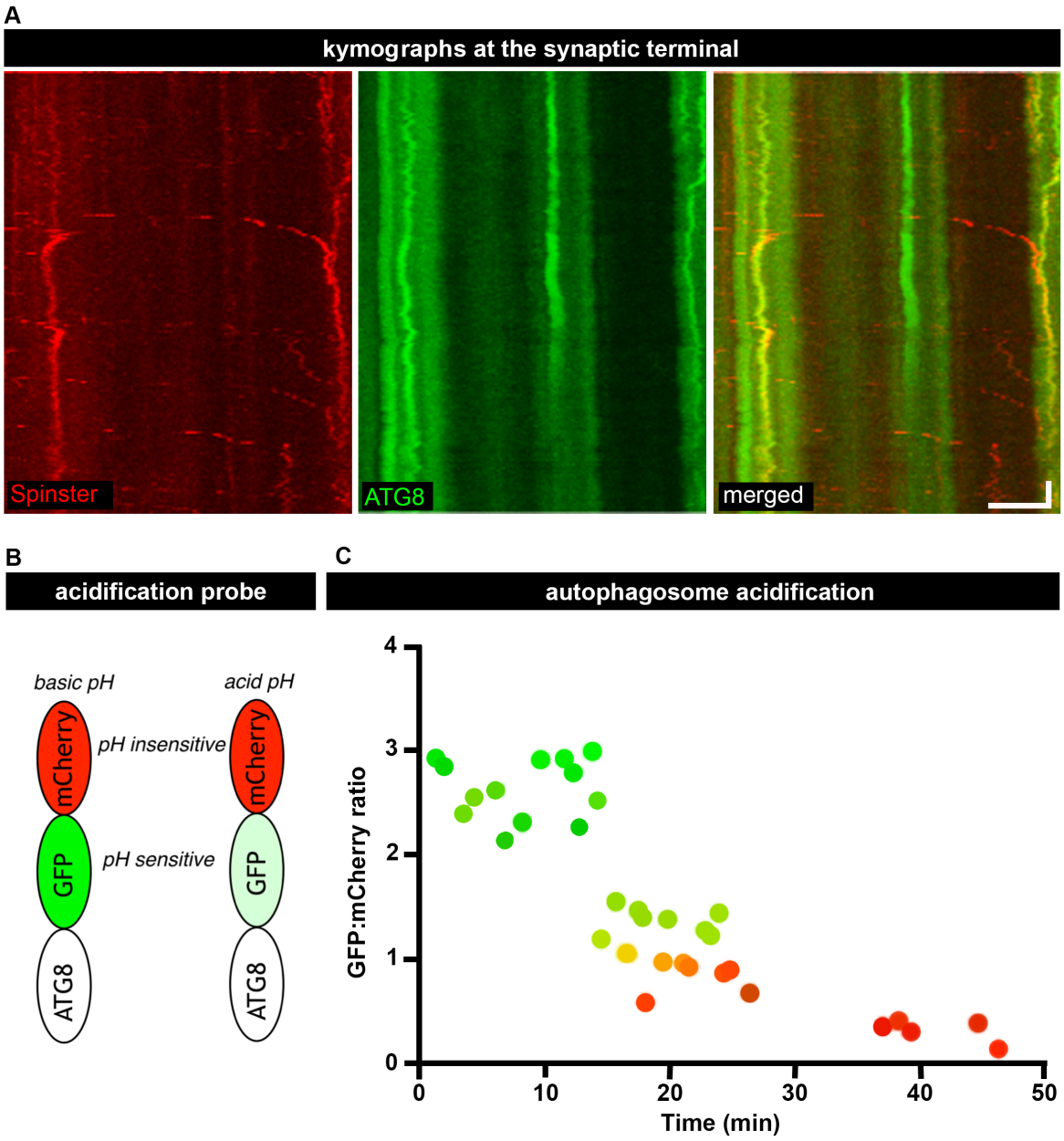

Fig. 7 | Lysosome fuses with autophagosomes and autophagosomes acidify at synaptic terminals.

(A) Kymographs of the synaptic terminal showing lysosome fusion with autophagosomes by coexpressing two probes: ATG8-GFP to label autophagosomes and Spinster-RFP to

label lysosomes. Almost horizontal lines of Spinster can be seen entering the NMJ (moving left to right) and fusing with autophagosomes. Scale bars 10 µm, 20 s. **(B)** Cartoon illustrating the ATG-GFP-mCherry construct used for monitorizing acidification; at non acidic pH the markers emits light in green and red, at lower pH, GFP is quenched and the signal becomes predominantly red. **(C)** Quantification of GFP-mCherry ratio of a recently formed autophagosome (n=1). As it can be seen the ratio decreases as the autophagosome acidifies, until being almost completely red after 45 min.

Markers of the degradation pathway co-transport with AZ proteins

As mentioned, to our surprise we had found that BRP anterograde cargoes were co-transported with lysosomal markers.

This was quite an unexpected result because the anterograde BRP cargoes that go from the cell soma to the synaptic terminal should not be in degradative compartments. Since very little is known about the nature of the cargoes that transport AZ precursor material to the synapse, we started to speculate that biogenetic cargo destined for forming AZs might be associated with lysosomal markers. To test that, we analyzed the BRP axonal transport together with other markers of the lysosomal pathway. We found that not only Lamp1, but also Spinster, another lysosomal marker, co-transported with BRP (Fig. 8 A-B).

To test if this was specific for BRP or could be the case for other synaptic proteins we performed the same experiment but this time using the synaptic vesicle marker: Syt-1 (instead of BRP). We also observed co-transport events of Syt-1 with the lysosomal marker Spinster (Fig. 8 C).

Microtubule-based anterograde transport of lysosomes in neurons (Farias et al., 2017) is mediated by Arl8, a small Ras-related GTPase, which connects lysosomes to kinesin motors (Farías et al., 2017; Rosa-Ferreira and Munro, 2011) such as Unc-104 (Kinesin-3), a protein required for axonal transport of presynaptic vesicle proteins to synapses (Klassen et al., 2010). Strikingly, BRP in most cases co-localized and was co-transported with Arl8-GFP in axons (Fig. 8 D). BRP and Rab7 co-transported together while moving retrogradelly (Fig. 6 A), however we could not find that they do co-transport anterogradelly (Fig. 9 A). We confirmed that in *Drosophila* Arl8-GFP is co-transported anterogradelly with the lysosomal marker Spinster-RFP in axons (Fig. 9 B). These

observations suggest that AZ and SV proteins undergo axonal co-transport in lysosome-related organelles.

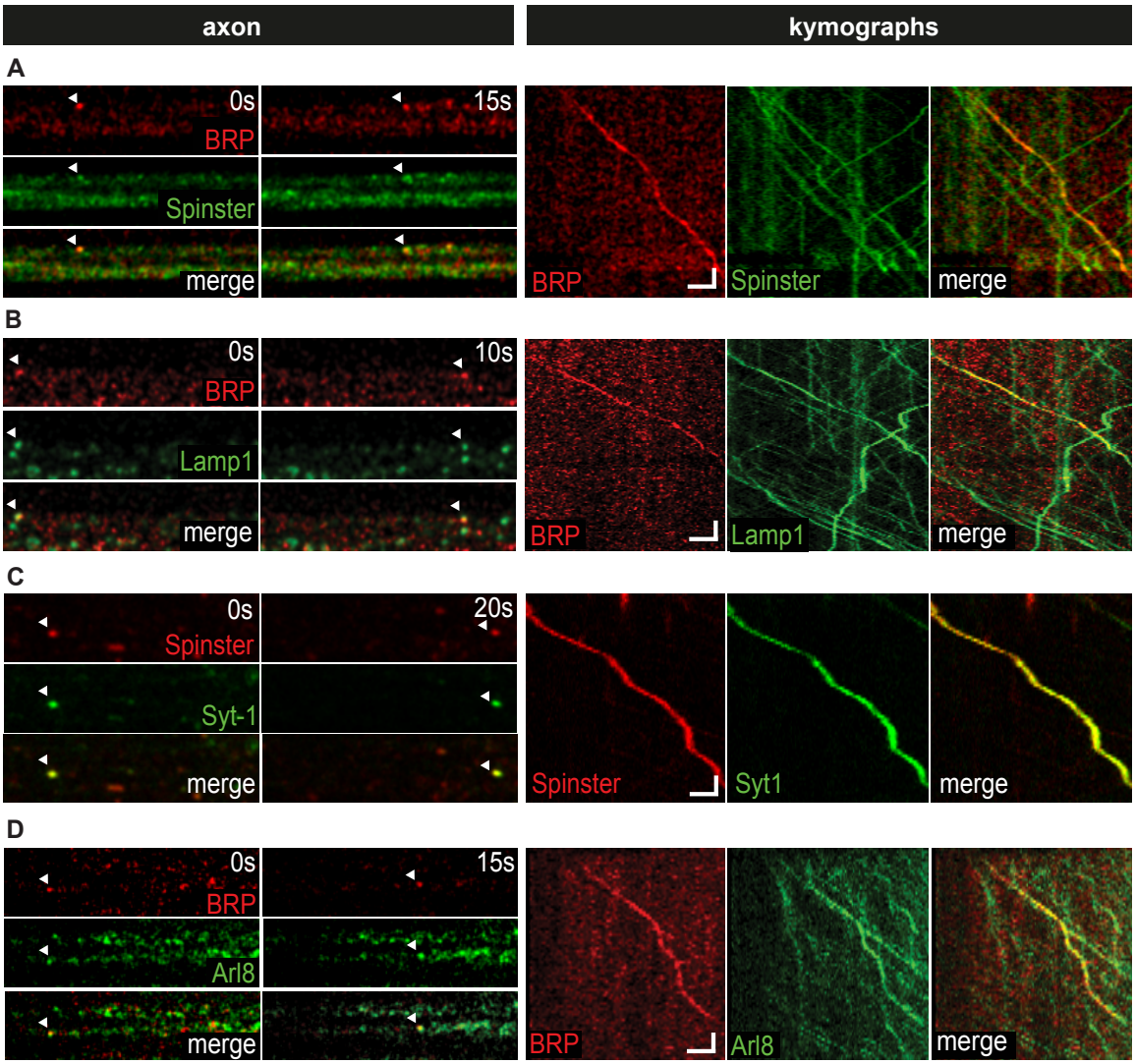

Fig. 8 | Axonal co-transport of AZ and SV proteins in presynaptic lysosome-related vesicles (PLVs).

(A-D) Anterograde co-transport of Bruchpilot (BRP) and Synaptotagmin-1 (Syt-1) with lysosomal markers and synaptic vesicle markers in Drosophila motoneuron axons in vivo. Single frames and kymographs of (A) co-transport of BRP-GFP (red) and Spinster-RFP (green), (B) BRP-RFP (red) and Lamp1-GFP (green) (C) Spinster-RFP (red) and Syt-1-GFP (green) and (D) BRP-RFP (red) and Arl8-GFP (green). Scale bar single frames 2 µm, kymographs 2 µm and 2 s.

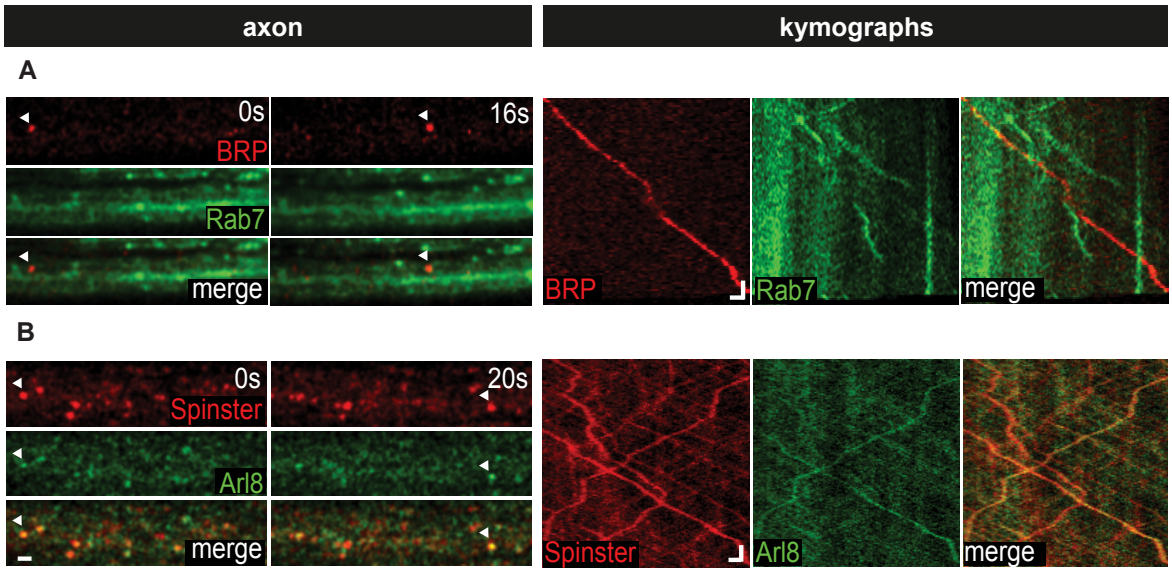

Fig. 9 | Presynaptic lysosome-related vesicles (PLVs) are distinct from Rab7-positive endosomes.

(A) Anterograde transport of BRP and the late endosomal marker Rab7. Live confocal imaging of intact 3rd instar larvae co-expressing fluorescent tagged BRP-short and Rab7. Single frames (left panel) and kymograph (right panel). Anterograde transport of BRP-RFP (red) cargoes appears not coupled to Rab7-GFP antergrade transport (green). **(B)** Anterograde transport of the lysosomal marker Spinster and the lysosomal adaptor Arl8. Live confocal imaging of intact 3rd instar larvae co-expressing fluorescent tagged Spinster and Arl8. Single frames (left panel) and kymograph (right panel) showing co-transport of Spinster-RFP (red) and Arl8-GFP (green). Scale bars: 2 µm and 2 s.

Axonal co-transport of AZ and SV proteins depends on the lysosomal kinesin adaptor Arl8

To further explore the mechanisms of axonal co-transport of AZ and SV proteins via lysosome-related vesicles we analyzed the localization and function of the lysosomal kinesin adaptor Arl8. At larval neuromuscular junction synapses Arl8-GFP and endogenous BRP labeled with specific antibodies displayed a partially overlapping punctate distribution (Fig. 10 A, confocal). Super-resolution imaging by two color stimulated emission depletion microscopy (gSTED) revealed a population of rather uniformly sized Arl8-positive vesicles located in close apposition to the BRP-positive AZ scaffold (Fig. 10 B, STED), consistent with a role for Arl8-mediated transport of lysosome-related vesicles in presynaptic assembly.

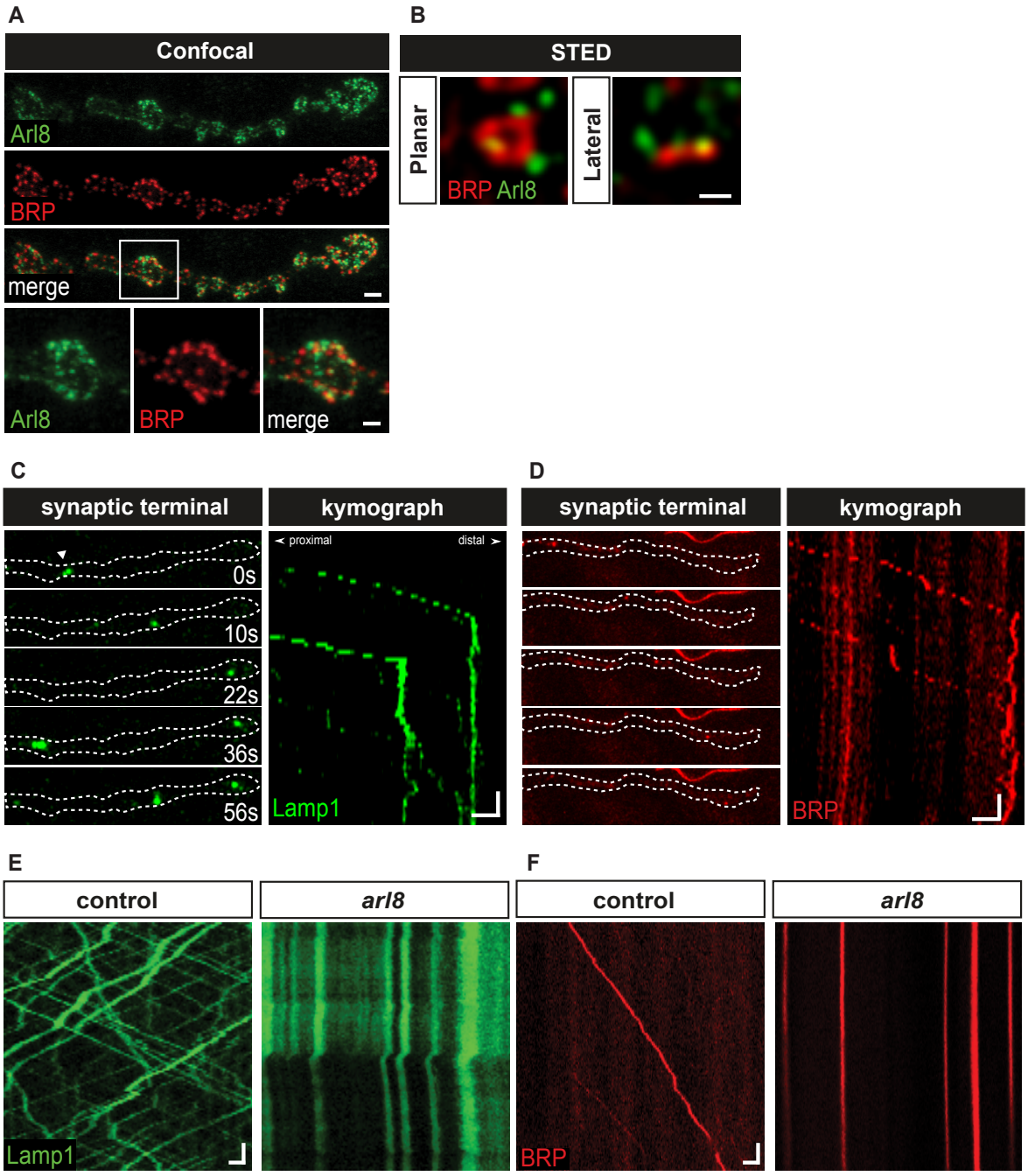

Fig. 10 | Arl8-mediates presynaptic delivery of PLVs.

(A-B) Arl8 localizes to vesicles surrounding the presynaptic AZ scaffold. **(A)** Confocal images showing the localization of Arl8-GFP containing PLVs at and around BRP-containing synapses at NMJs. **(B)** gSTED images (planar and lateral) of larval *Drosophila* NMJs from Arl8-GFP transgenic animals stained for GFP and endogenous BRP. Scale bars: 2 µm (confocal) and 200 nm (STED). STED images were taken by Dr. Astrid Petzoldt. **(C)** Presynaptic delivery of Lamp1-GFP vesicles to presynaptic terminals. Shown are still images at different time points and representative kymograph from live imaging of Lamp1-GFP containing PLVs in *Drosophila* motoneurons. Lamp1-GFP vesicles (PLVs) are seen to enter the NMJ from the axon (t=0, t=36 s) and move into the distal presynaptic

terminal (t=22, t= 56 s). **(D)** Presynaptic delivery of BRP-RFP (red) to the synaptic terminal. To the right still images at different time points and corresponding kymograph to the left showing anterograde cargo entering the terminal and after reaching it, staying quiet. Scale bars: 2 μm and 4 s. **(E, F)** Loss of Arl8 in *arl8* null mutant flies abolishes anterograde transport of PLVs containing Lamp1- GFP **(E)** and BRP-RFP **(F)**. Kymographs with control larvae (left) and *arl8* null mutant (right). Scale bars: 2 μm and 4 s.

If these Arl8 positive cargoes are transporting BRP and Syt-1 to the synapse, we would expect to see these cargoes not only at the axon but also arriving at the NMJ synaptic terminal for delivery. In order to be able to see arriving cargoes at the NMJ we followed the SPAIM (simultaneous photobleaching and imaging) protocol described by (Wong et al., 2012). Briefly, the method consists of bleaching the synaptic terminal completely to delete any fluorescent signal that is already present at the NMJ. After observing some cargo entering the NMJ the proximal part of the synaptic terminal is bleached by increasing the laser intensity again in order to bleach new cargoes arriving and facilitating therefore the tracking of the smaller number of cargoes that already entered. The simultaneous bleaching is most important when dealing with cargoes that are very abundant, like Lamp1, and less with cargoes that have a lower turnover.

When we did the experiment using Lamp1-GFP we could indeed track presynaptic delivery of Lamp1-GFP vesicles to nerve terminals (Fig. 10 C). We were also able to observe some BRP moving vesicles entering the NMJ at a much lower rate (Fig. 10 D). As one can see in the still images, but more clearly in the kymograph, Lamp1 vesicles entered the synaptic terminal and continued moving anterogradelly until reaching the last or second last bouton, where the vesicles stopped and remained quiet. This process was relatively easy to observe with the Lamp1 marker, not so much when labeling BRP. After hours of recording now and then one BRP positive cargo could be tracked. This is in accordance with BRP having a slow turnover at the AZ. Nevertheless, the cargoes that could be tracked behaved in a similar manner as those of Lamp1, they entered the NMJ terminal and upon finding a specific spot (more often at the terminal bouton) they stopped anterograde motion and remained still. We conclude that by stationing at these specific boutons they can provide new material to the AZ. However, it is not possible to determine whether this takes place via fusion of the plasma membrane.

These results suggest that Lamp1/BRP-containing vesicles correspond to lysosome-related organelles (Marks et al., 2013) that are transported to the presynapse via Arl8-linked kinesin motors.

To put this model to the test we analyzed whether the observed co-transport of lysosomal markers and motile BRP punctae was dependent on Arl8 function. Indeed, we found that genetic loss of *arl8* greatly reduced the anterograde motility of Lamp1-GFP and, importantly, also of BRP-RFP cargo (Fig. 10 E-F). Kymographs clearly showed how in wild-type (WT) larvae there was abundant transport in both directions of Lamp1-GFP puncta. However, in the larvae lacking Arl8 this transport was almost completely abolished and there were only stationary cargoes to be seen. Similar is the case of BRP, whereas in WT animals there were few anterograde (Fig. 10 F) and retrograde (not shown) cargoes, in the absence of Arl8 these cargoes failed to move and could be seen as stationary in the axonal segments close to the motoneuron cell bodies. Our data identified anterogradelly targeted presynaptic AZ precursor vesicles as Arl8-positive lysosomal vesicles, akin to secretory lysosomes found in other cell types, most prominently in melanocytes and cytotoxic T cells (Marks et al., 2013). These organelles hereafter referred to as presynaptic lysosome-related vesicles (PLVs) depend on Arl8 for anterograde axonal transport and may be required for presynaptic biogenesis.

Arl8-mediated delivery of PLVs is required for presynaptic biogenesis and synaptic function

If PLVs indeed represented precursor organelles for the presynaptic co-assembly of AZ and SV components, stalling their axonal transport and delivery as seen before (Fig. 10 E-F) should greatly impact presynaptic biogenesis. To probe this we analyzed NMJs from wild-type and *arl8* mutant 3rd instar larvae. In comparison to WT, NMJs from *arl8* mutant larvae were visibly smaller as can be seen with the presynaptic marker HRP (Fig. 11 A). The *arl8* mutant NMJs were not only severely reduced in size but had also anomalously small, almost non existing, presynaptic boutons (Fig. 10 A). We quantified the total NMJ area in control larvae versus *arl8* and observed a reduction to almost half of its area (Fig. 11 B).

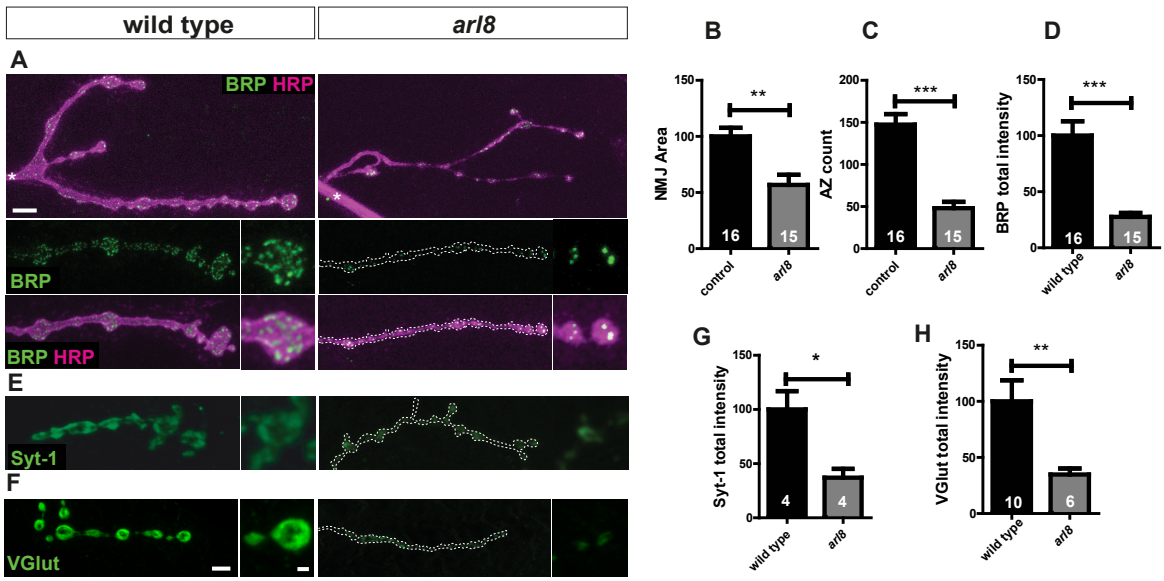

Fig. 11 | Arl8-mediated delivery of PLVs is required for presynaptic biogenesis and synaptic function.

(A-H) Defective presynaptic biogenesis in absence of Arl8-mediated PLV delivery. **(A)** Reduced AZ count and BRP levels at *arl8* mutant NMJs. Confocal images of wild-type (WT) and *arl8* mutant NMJ synapses of *Drosophila* 3rd instar larvae stained for BRP (green) and HRP as axonal membrane marker (magenta). Top panel, overview. Bottom panel and insets on the right represent zooms. *arl8* mutant NMJs display small boutons with drastically reduced numbers of active zones (AZs). **(B-D)** Quantification of representative data shown in **(A)**. **(B)** In *arl8* mutants the NMJ area is reduced to 57% of that in WT [µm2] (HRP area of the maximum projection). **(C)** Absolute numbers of presynaptic AZs/ NMJ (WT 147.38 ± 12.6, *arl8* mutant 48.13 ± 7.4) and **(D)** total BRP sum intensity/ NMJ (WT 100 ± 12.8, *arl8* mutant 27.6 ± 3.5) are severely reduced. n=16 (WT) and 15 (*arl8* mutant) NMJs. **(E-H)** Reduced levels of SV proteins synaptotagmin 1 (Syt-1) (WT 100 ± 16.8, *arl8* mutant 37.05 ± 8.1; n=4 NMJs) **(E, G)** and the vesicular glutamate transporter (VGlut) (WT 100 ± 18.8, *arl8* mutant 34.6 ± 5.4; n=10 (WT) and 6 (*arl8*)) **(F,H)** at *arl8* mutant NMJs. Scale bars, 5 µm (upper), 4 µm (lower) and 1 µm (zoom). Data in **(G)** and **(F)** are quantifications of representative examples displayed in **(E)** and **(F)**. Experiments were performed together with Dr. Astrid Petzoldt and Dr. Anela Vukoja.

Furthermore, the number of AZs and the total intensity of BRP were dramatically reduced in *arl8* mutant NMJs (Fig. 11 C-D) Thus, inhibition of anterograde axonal transport of PLVs in absence of Arl8 results in severe defects in presynaptic biogenesis, most notably a near complete loss of AZ proteins such as BRP from presynaptic boutons, eventually resulting in the death of *arl8* mutant larvae at the late larval stage (Vukoja,

2014). Given that SVs undergo exo-endocytic cycling at the AZ and that the AZ protein BRP and the SV protein Synaptotagmin 1 are co-transported in PLVs along the axon to the presynapse (Fig. 8) we probed whether loss of *arl8* might affect the delivery of other presynaptic components, most notably SV proteins. We found *arl8* mutant NMJs to contain strongly reduced amounts of SV proteins such as Synaptotagmin-1 (Fig. 11 E, G), the Vesicular Glutamate-transporter (vGlut) (Fig. 5 F, H). Cysteine-String Protein (CSP), and Synapsin (Fig. 12 D, E). The levels of endocytic proteins that orchestrate SV recycling and reformation (Haucke et al., 2011; Kononenko and Haucke, 2015; Murthy and Camilli, 2003; Podufall et al., 2014) including Dynamin, Dap160/ intersectin, and Stoned B (StnB) were also reduced (Fig. 12 A-C, F-H).

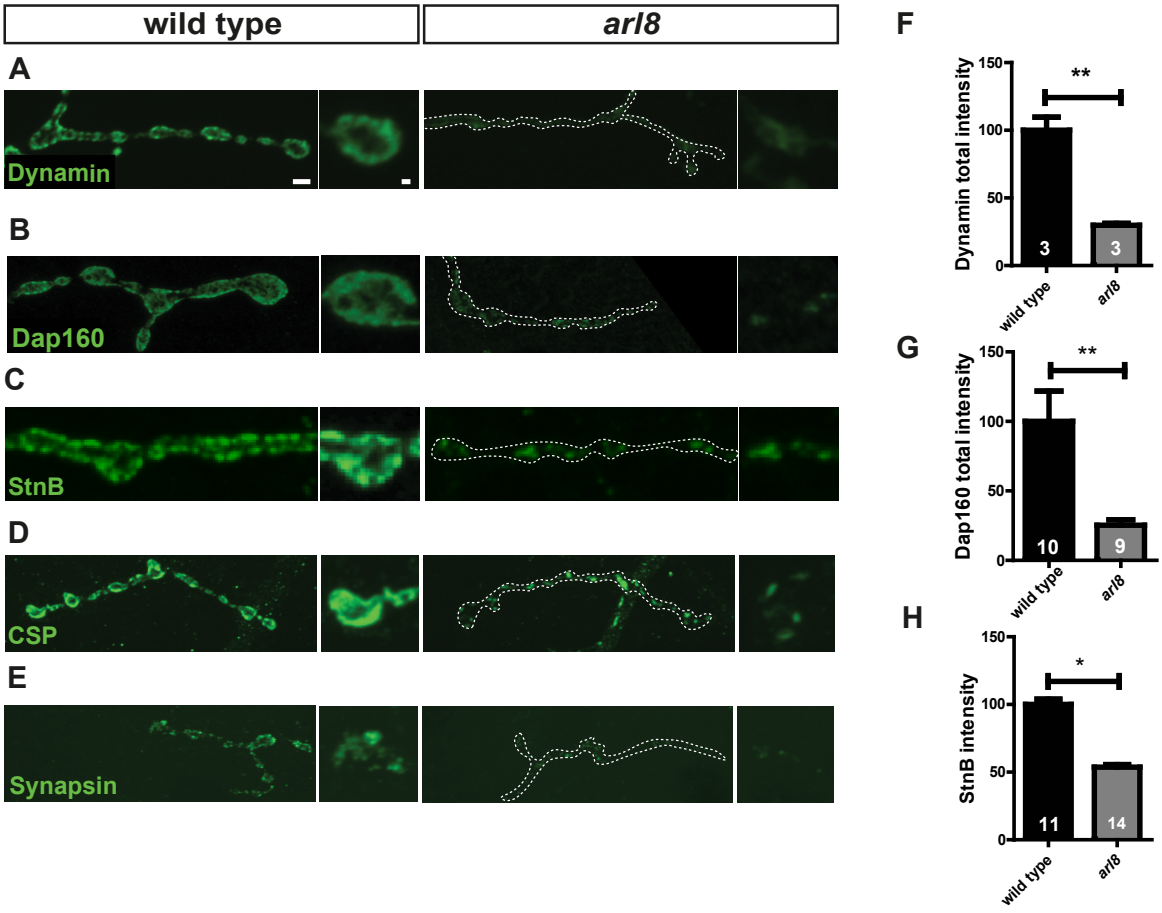

Fig. 12 | Arl8-mediated PLV delivery is required for presynaptic biogenesis and synaptic function.

(A-F) Defective presynaptic biogenesis in absence of Arl8-mediated PLV delivery. **(A-C)** Drastically reduced levels of endocytic proteins at the *arl8* mutant NMJs. Confocal images of wild-type (WT) and *arl8* mutant NMJ synapses of *Drosophila* 3rd instar larvae stained for dynamin (green) **(A)**, dap160/ intersectin (green) **(B)**, stoned B (green) **(C)**. **(D-E)** Reduced levels of SV proteins at the *arl8* mutant NMJs. Confocal images of wild-type (WT) and *arl8* mutant NMJ synapses stained for cysteine-string protein (green) **(D)**,

synapsin (green) **(E),** Scale bars are 4 µm for the overview and 1 µm for the zoom. **(F, G, H)** Quantification of representative data shown in (A-C). In *arl8* mutants the total dynamin total intensity/NMJ (WT 100.0 ± 9.728; *arl8* mutant 29.8 ± 1,44 (n=3)), Dap160 total intensity/NMJ (WT 100 ± 21,80 (n=10), *arl8* mutant 25,26 ± 3,88 (n=9) and stoned B total intensity/NMJ (WT 100 ± 3,97 (n=11), *arl8* mutant 53 ± 1,89 (n=14)) are severely reduced. Experiments were performed together with Dr. Anela Vukoja.

At this point, the question rose if Arl8 could be required for proper microtubule formation or patterning. If so, then the observed *arl8* phenotype would not be due to a defect in PLV transport but it would be rather a general transport phenotype. To test that, we stained WT and *arl8* mutant NMJs with Futsch, a microtubule associated protein and Ankyrin2, which also binds to microtubule and contributes to NMJ developing. Our stainings (Fig. 13A-B) revealed that the cytoskeleton of *arl8* larvae was not affected. This experiment discarded that the reduced amount of AZ and SV proteins at the synaptic terminal were secondary to some cytoskeletal defect.

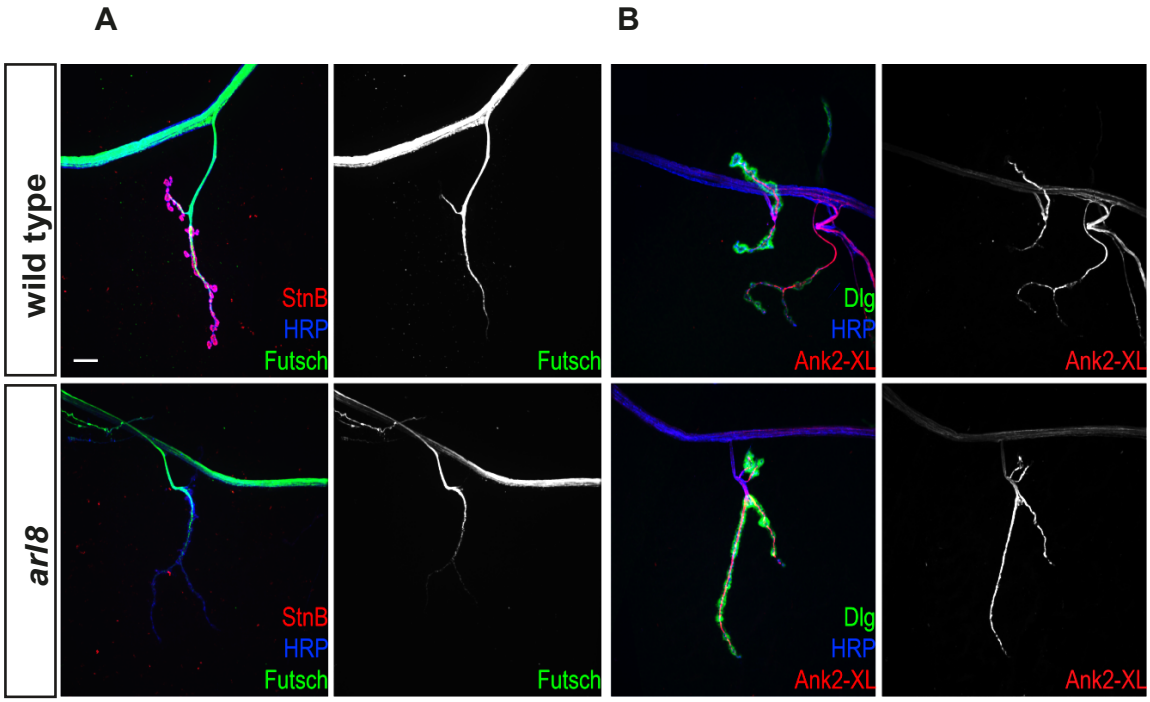

Fig. 13 | The cytoskeleton of *arl8* mutant motoneurons remained widely intact.
(A-B) NMJs at muscle 4 of *arl8* mutant and wild type larvae immunostained against **(A)** Futsch, HRP, StonedB (StnB) and **(B)** disc large (Dlg), Ankyrin2-XL (Ank2-XL) and HRP are shown. Futsch, Ankyrin2-XL and disc large are all largely unaffected in mutant larvae (compare upper and lower panels). In stark contrast, StonedB was almost completely absent from the mutant NMJ. Scale bar: 10µm. Experiments were performed by Dr. Anela Vukoja.

A presynaptic role of Arl8 for proper formation of NMJ terminals

The Arl8 mutant was generated by the insertion of a PiggyBac element (Fraser et al., 1983; Kudo et al., 2017). To verify that this insertion was abolishing specifically Arl8 expression, we tested for Arl8 mRNA levels via RT-PCR in control and PBac(RB)Gie^{e00336} homozygous flies. We found that in fact the insertion produced a null mutant since no traces of Arl8 could be detected, in comparison the wild type flies gave a band corresponding to the expected weight of Arl8 (Fig. 14 A). Control primers where used for AP-2 and gave a positive band in both Arl8 null and control animals (Fig. 14 A).

Furthermore, Arl8 is expressed in all cell types, therefore its complete depletion is probable to cause effects not only in motoneurons. To check for specificity we generated transgenic *Drosophila* containing a UAS Arl8 construct (described in the Introduction). We designed an experiment to detect whether expressing Arl8 alone in motoneurons was sufficient to rescue the phenotype. For that, the UAS Arl8 construct was expressed under the OK6-GAL4 line, which is known to drive expression specifically in motoneurons. The genotype of the stock further referred as "rescue" was then the following: OK6-GAL4/UAS-Arl8; PBac(RB)Gie^{e00336}/ PBac(RB)Gie^{e0033}. Importantly, we found that overexpression of Arl8 alone in motoneurons could rescue the Arl8 phenotype. The loss of AZ and SV proteins had wild type levels after presynaptic re-expression of native Arl8 (Fig. 14 B-D), indicating that it was a cell-autonomous and neuron-specific phenotype.

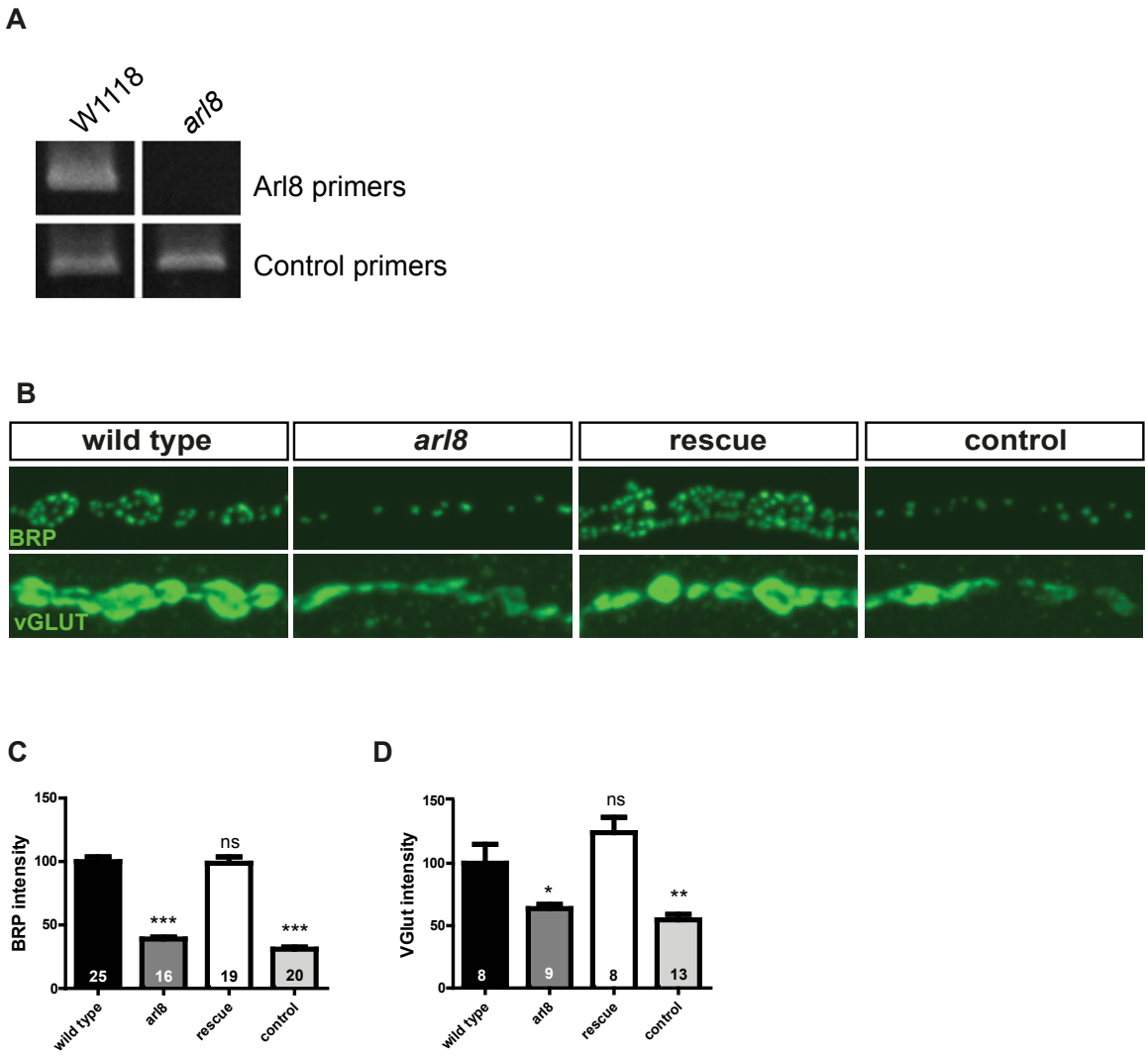

Fig. 14 | Arl8 presynaptic expression rescues Arl8 phenotype.

(A) Whole wild type and homozygous PBac(RB)Gie^{e0033} larvae were used to isolate total mRNA which was then transcribed into cDNA in a RT-PCR reaction. Thus prepared cDNA was subsequently used as a template for a PCR reaction to probe for presence of *arl8* cDNA or *AP-2 sigma* cDNA (control). Whereas *AP-2 sigma* cDNA is detectable in probes of animals of both genotypes, *arl8* cDNA is present only in wild type animals and is undetectable in homozygous PBac(RB)Gie^{e0033}. (B) Loss of presynaptic components can be rescued by presynaptic re-expression of Arl8-GFP implying a cell-autonomous and specific *arl8* mutant phenotype. Confocal images of wild-type (WT), *arl8* mutant, presynaptic rescue and rescue-control (driver only) NMJ synapses of *Drosophila* 3rd instar larvae stained for BRP (green, upper panel) and VGLUT (green, lower panel) showing a rescue of both synaptic components to WT levels compared to the *arl8* mutant and the rescue-control. Scale bar: 4 µm. (C-D) Re-expression of Arl8 in motoneurons rescues defective presynaptic biogenesis in *arl8* mutants. Quantification of representative data shown in (B). The BRP total intensity is reduced in the *arl8* mutants compared to WT (WT 100 ± 18.63 (n=25), *arl8* mutant 38.85 ± 6.21 (n=16), while the presynaptic rescue

show WT levels (99.17 ± 21.81 (n=19)) and is increased compared to the rescue-control (31.09 ± 7.11 (n=20)). Similar results were quantified for VGLUT (WT 100 ± 42.92 (n=8) *arl8* mutant 63,67 ± 10,09 (n=9), rescue 124,51± 34,68 (n=8), rescue-control 54,71 ± 16,127 (n=13). Statistics: All graphs show mean ± SEM. Mann-Whitney test for two groups, One-way ANOVA for more than two. * P<0.05, ** P<0.01, *** P<0.001, n.s. for not significant. Experiments were performed together with Dr. Anela Vukoja and Dr. Astrid Petzoldt.

Arl8 and the HOPS complex cooperate in presynaptic biogenesis

To further verify that the observed Arl8 phenotype was a presynaptic effect, we overexpressed and RNAi lines from the Vienna stock collection that specifically target Arl8 mRNA and thereby block its translation into protein (Dietzl et al., 2007). Using this method, we were able to deplete Arl8 levels only in motoneurons, while the rest of tissues and cell types kept expressing Arl8 at their usual levels. Consistently, when Arl8 expression was downregulated specifically in motoneurons, defective presynaptic biogenesis including depletion of BRP was also observed (Fig. 15 A-C). [6]

We then used another RNAi line against the HOPS complex to see if we could phenocopy the Arl8 depletion effects. HOPS stands for homotypic fusion and protein sorting tethering complex. The HOPS complex is a multi-subunit complex conserved from yeast to mammals that regulates late endosome and lysosome fusion (Khatter et al., 2015). It is formed by 6 Vacuolar sorting proteins (VPS): VPS11, VPS16, VPS18, VPS33, VPS39 and VPS41. We did a small RNAi screen against these proteins to see if they could be related to the Arl8 pathway. Unfortunately, there were no RNAi lines available for all the subunits, so we could only test the depletions of VPS16, VPS18, VPS33 and VPS39. VPS16, VPS18 and VPS33 RNAi lines showed no phenotype (not shown), indicating either that a) the RNAi lines did not work or were not strong enough to show a phenotype or b) that their suppression could be compensated. Most interestingly, the depletion of the VPS39 subunit showed a phenotype that resembled to that of the *arl8* mutants. As it can be seen (Fig. 14 A), NMJs of larvae expressing the VPS39-RNAi line in motoneurons showed very thin synaptic terminals, resembling to the *arl8* mutant (Fig.

[6] Note that the control group, is a control for the driver line, to discard that is not the OK6-GAL4 construct that is rescuing the Arl8 deficit (its exact genotype is OK6-GAL4/+; PBac(RB)Gie^{e00336}/ PBac(RB)Gie^{e0033}).

11 A for comparison) and very similar to the Arl8 RNAi line (Fig. 15 A). Quantification showed that BRP mean intensity was reduced to the half, and the number of AZ was also reduced, having the AZ density (AZ/NMJ area) of 67 compared to Control, 100. The reduction of BRP intensity as well as AZ density was similar to the Arl8-RNAi line.

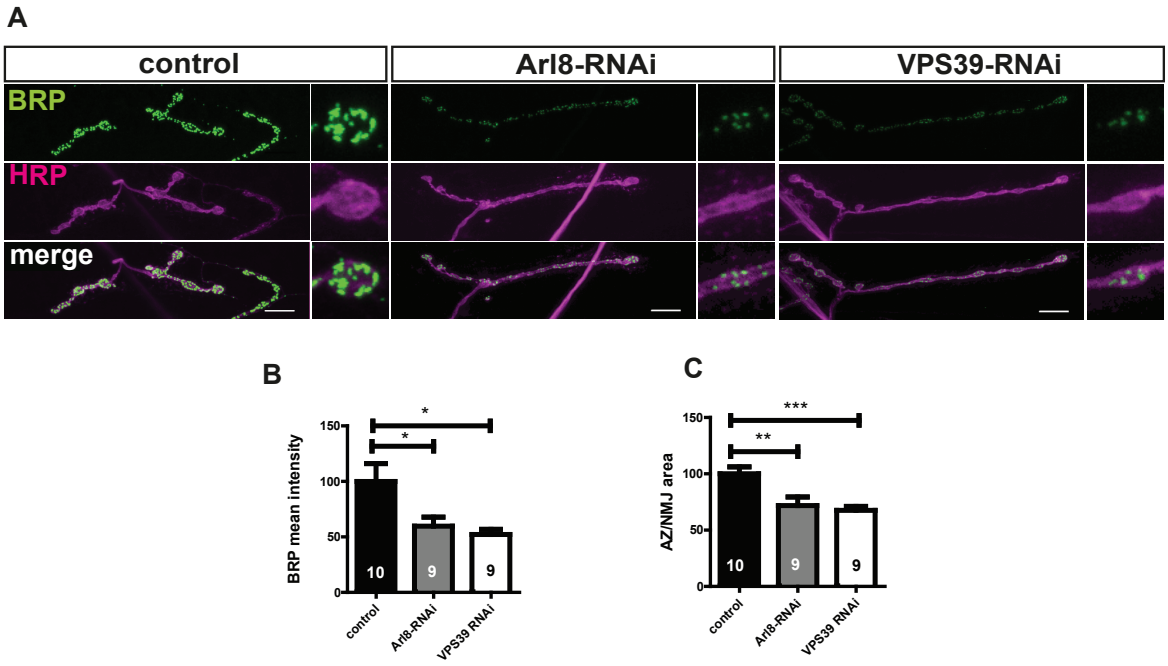

Fig. 15 | Defective HOPS complex phenocopies Arl8 knockdown and ultrastructural characterization of the *arl8* mutant.

(A) Confocal images of control (driver-line only, left panel), Arl8-RNAi (middle panel) and VPS39-RNAi (right panel) NMJ synapses of *Drosophila* 3rd instar larvae stained for BRP (green, top panel and HRP (magenta, central panel). Scale bar: 10 µm. Both Arl8 and VPS39 knockdown display thinner NMJs with small boutons and reduced numbers of AZ (see b). **(B-C)** Quantification of representative data shown in (A). Total BRP intensity/ NMJ (100 ± 22.91 (n=10), Arl8-RNAi 29.95 ± 6.51 (n=9), VPS 39-RNAi 41.43 ± 6.606 (n=9)) and absolute numbers of presynaptic AZs normalized to the NMJ area (control 100.0 ± 6.16 (n=10), Arl8-RNAi 71.86 ± 7.61 (n=9), VPS39-RNAi 67.57 ± 3.47 (n=9)) are severely reduced, with an equal reduction level for VPS39 knock-down compared to the Arl8-RNAi. Experiments performed together with Dr. Astrid Petzoldt.

Arl8 mutants: extremely thin terminals with severe electrophysiological defects but with the AZ structure conserved

Taking into account the remarked morphological modifications found on the *arl8* mutants presynaptic terminals as well as the drastic reduction of BRP and SV markers (Syt-1, VGlut and CSP) found using confocal microscopy, we performed electron microscopy (EM) on NMJ of both *arl8* mutant larvae and control. EM images confirmed the substantial reduction of bouton size in *arl8* mutants (Fig. 16 A). The terminals were much thinner and the quantification also revealed a decreased number of total synaptic vesicles. Interestingly, however, normalized to the bouton area the number of synaptic vesicles was not changed in *arl8* mutants.

To further address how synapses get compromised by the absence of Arl8, we wanted to see if the few AZs that can still form in the *arl8* mutants would be rather normal or would be also affected in ultrastructural or functional terms. Obviously, a drastic reduction of BRP transport might *per se* result in a reduced size of AZ scaffolds. If Arl8 main role is to deliver BRP to the terminal, less BRP would mean less but otherwise normal AZs, i.e., the machinery for AZ assembly should remain intact and thereby the system will just produce normal active zones with normal architecture but just fewer. On the other hand, if Arl8 plays a role in one of the assembly steps the architecture would be affected. Such is the case of proteins previously reported in the Sigrist lab like Neurexin or Spinophilin (Muhammad et al., 2015). Then, not only will the NMJ have less AZs as already shown, but also these will be defective.

Looking at our images obtained with confocal microscope we could not resolve differences in AZ size. Did that mean the AZs in *arl8* mutant are same or are there differences but they are below confocal resolution? To test that, we used super resolution STED microscopy. BRP puncta that are visualized in confocal imaging are actually rings whose diameter can be measured in STED microscopy. As it can be seen (Fig. 16 E) also in STED *arl8* mutants did not show the typical boutons and had fewer AZ. However, the average ring size did not differ between control and *arl8* mutant (Fig. 16 F). Control rings were 159 nm, same as in *arl8* null background. From these results we could conclude that Arl8 is important for BRP transport indeed, but does not play a role in the assembly of the BRP scaffold assembly.

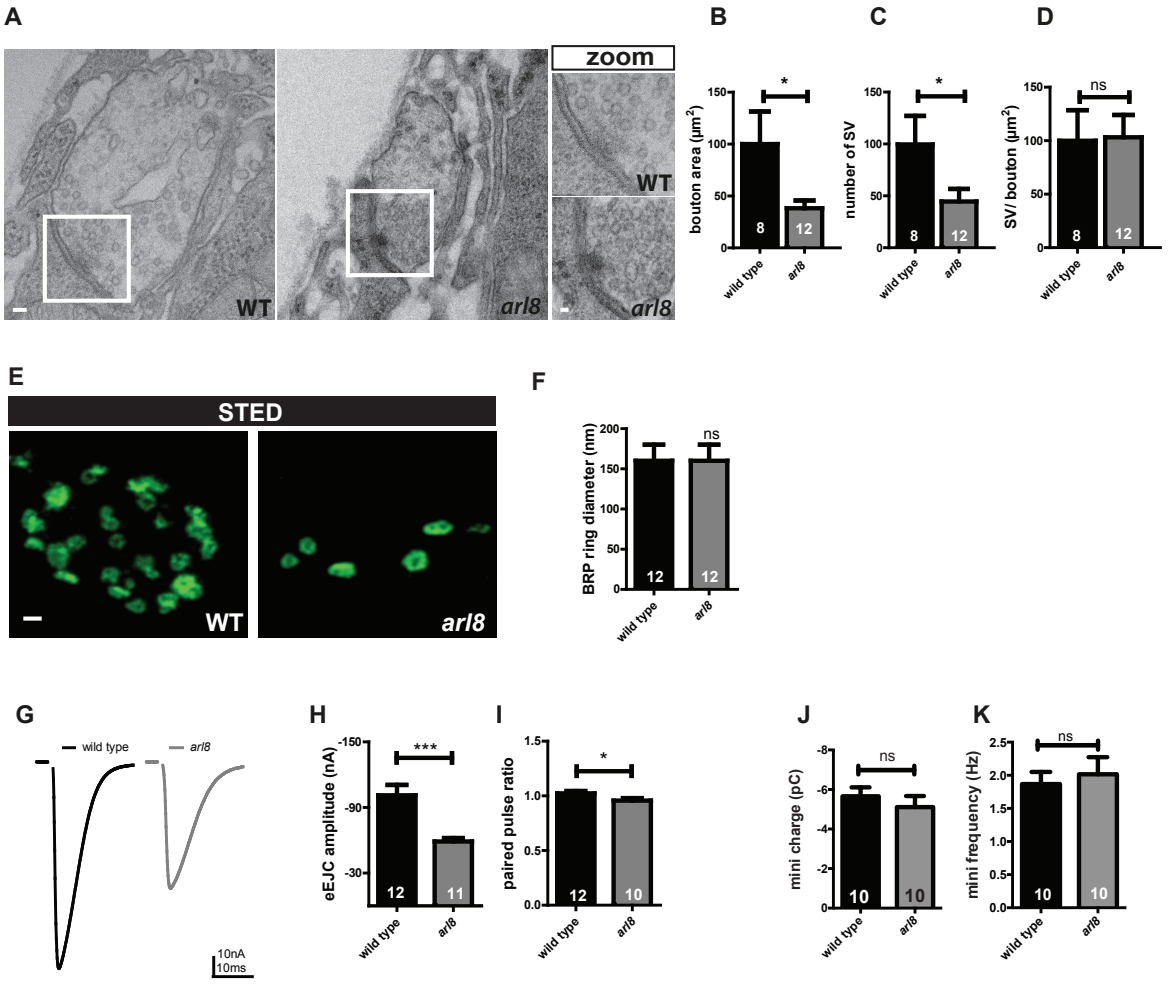

Fig. 16 | Shrunk boutons with severe electrophysiological defects but with the AZ structure conserved.

(A) Electron micrographs of wild-type (WT) and *arl8* mutant boutons of *Drosophila* 3rd instar larval NMJs depicting an entire bouton (left panels) and a zoom (right panels). Presynaptic ultrastructure and SV accumulation are not affected in the *arl8* mutant. Scale bar 70 nm in overview and 20 nm in zoom. **(B-D)** Quantification of representative data shown in (A). Bouton area is severely reduced in the *arl8* mutant (WT 100 ± 31.46 with n=8, *arl8* mutant 38.24 ± 7.47 µm2, n=12) with a proportional reduction in SV numbers (WT 99.50 ± 27.62 µm2, *arl8* mutant 44.50 ± 12.20 µm2), although the SV density was not affected (WT 100 ± 28.56 µm2, *arl8* mutant 103.2 ± 20.88). **(E)** Images and **(F)**, quantification of the BRP ring diameter at *Drosophila* neuromuscular junctions with superresolution light microscopy (STED) for wild type (159±22 nm (n=12)) and *arl8* mutant (158±26 nm, (n=12). Scale bar: 100 nm. **(G-I)** Defective presynaptic biogenesis in absence of Arl8 impairs evoked neurotransmission. **(G-H)** Two electrode voltage clamp electrophysiological recordings show reduced evoked excitatory junctional current (eEJC) amplitudes at *arl8* mutant synapses (WT -101.09 ± 9.4 nA, n=12 and *arl8* mutant -58.79 ± 3.1 nA n=11 NMJs), **(I)** while only minor changes in the paired pulse ratio (30 ms ISI) were

observed (WT 1.02 ± 0.02 s n=12, *arl8* mutant 0.95 ± 0.02 s, n=10 NMJs). **(J-K)** Mini amplitude remained unchanged (WT -0.76 ± 0.02 nA, n=10, *arl8* mutant -0.74 ± 0.02 nA, n=10 NMJs) and mini frequency was not significantly different (WT 1.87 ± 0.18 Hz n=10, *arl8* mutant 2.01 ± 0.25 Hz, n=10 NMJs). EM data were acquired together with Dr. Anela Vukoja and Christine Quentin. Eric Reynolds performed the electrophysiological analysis.

Next, we wanted to test for electrophysiological defects in *arl8* mutant. Defects in SV and AZ protein transport and presynaptic biogenesis might *per se* impair neurotransmission (Kittel et al., 2006a; Wagh et al., 2006). To test that we performed two electrode voltage clamp electrophysiological recordings in *arl8* mutants. Indeed, evoked excitatory junctional currents (eEJCs) were reduced in *arl8* mutants compared to controls (Fig. 16 G-H). Mutant *arl8* larvae also showed a small but significant reduction in the paired pulse ratio (Fig. 16 I), a parameter for short-term plasticity (Hallermann et al., 2010). Mini amplitude was not affected nor was mini frequency that had similar values to control (Fig. 16 J-K).

The reduction of eEJC can be well explained by the reduced number of synaptic release sites per NMJ. Mini amplitude is not altered consistent with the Glutamate receptor fields having wild type levels (not shown). This indicates that the residual set of AZs that form at the terminal function properly, which is also corroborated by the normal ultrastructure (Fig 15 E-F) and the unchanged SV vesicle density (Fig. 16 D) of the *arl8* mutants. Mini frequency typically scales with the number of AZs per terminal, in this case it remains unanswered why is not affected in *arl8* mutants.

Arl8 overexpression in motoneurons promotes biogenesis

We demonstrated so far that Arl8 co-transports with BRP and is needed for proper AZ protein delivery at the synapse. Next, we wanted to challenge our results by an independent approach. If PLV transport by Arl8 indeed mediates presynaptic biogenesis, gain of Arl8 function, e.g. by overexpression, might result in increased delivery of presynaptic components and, thereby, a facilitation of evoked neurotransmission. To test this hypothesis we used the same UAS Arl8 line and same driver (OK6 GAL4) used for the rescue experiments, but this time we overexpressed it in a wild type background and kept the flies at 29 ºC to boost more the transcription. This genotype (OK6-GAL4/UAS-Arl8) from hereon is referred to as Arl8 OE. Note that Arl8 OE still contains two copies of

the *arl8* locus in every tissue, but on top of that has an extra Arl8 sequence that will be overexpressed in motoneurons only.

As predicted, an increase in Arl8 copy number facilitated delivery of BRP to presynaptic boutons (Fig. 17 A-B). We observed slightly bigger junctions and the quantification of total BRP intensity was increased as well (Fig. 17 B). Under Arl8 OE the NMJs had also more AZ but only slightly and was not significant (Fig. 17 C).

We again prepared samples for superresolution in order to check whether BRP ring diameter was affected or not. The results showed a slightly increase in diameter (Fig 12. D) but was not significant (Control 159 nm, Arl8 OE 170 nm) (Fig 12. E), further indicating that Arl8 does not play a role in the assembly process of BRP.

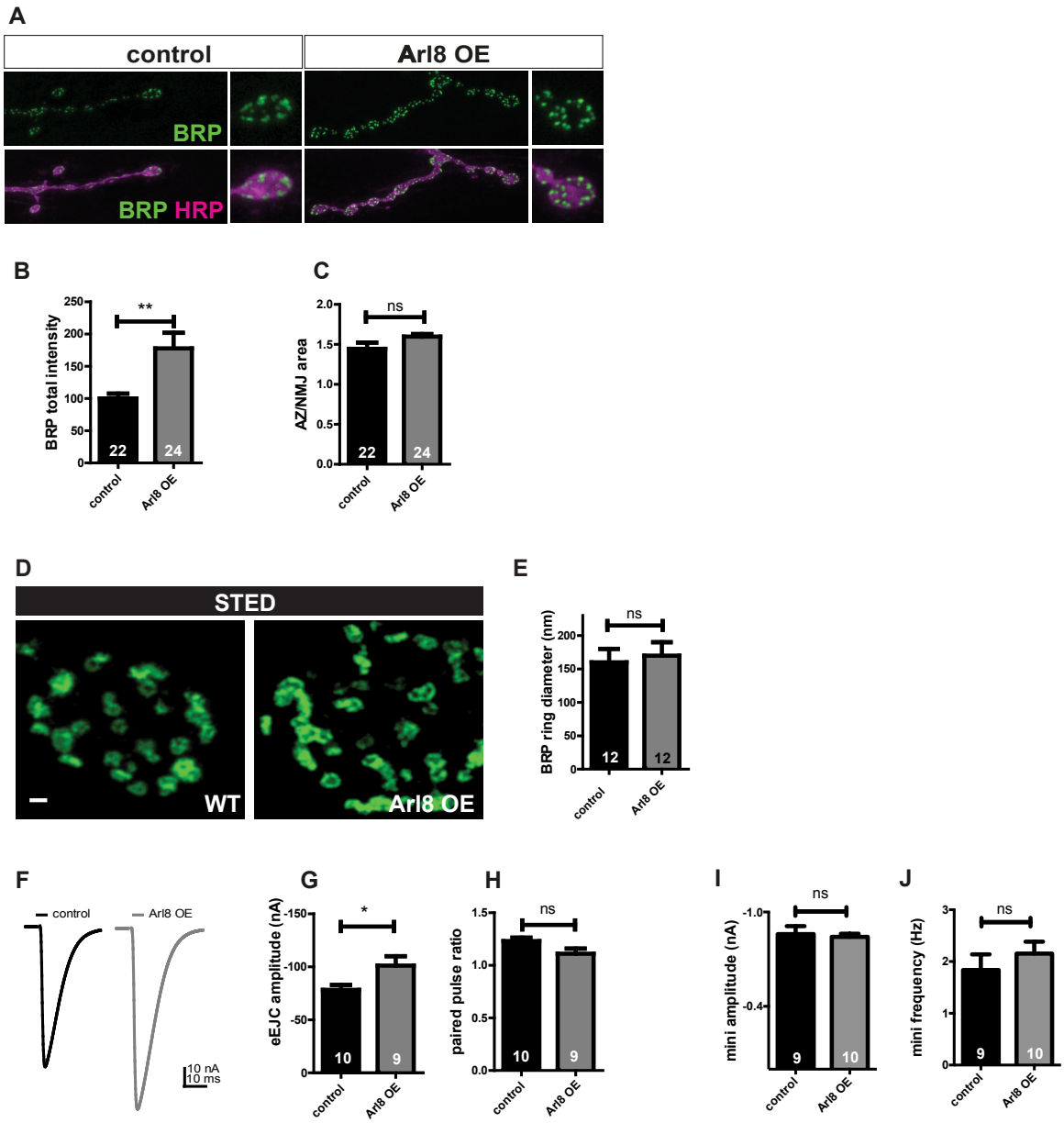

Fig. 17 | Elevated Arl8-mediated anterograde transport of PLVs facilitates presynaptic biogenesis and neurotransmission.

(A, B) Elevated PLV delivery in Arl8-overexpressing NMJs facilitates presynaptic biogenesis. **(A)** Confocal images of NMJs from control and transgenic *Drosophila* larvae overexpressing Arl8 (Arl8 OE) reveal increased BRP levels. Scale bars: 4 and 1 µm (zoom). **(B-C)** Quantification of representative data shown in (A). BRP total intensity: WT 100 ± 7.5 n=22, Arl8-OE 177 ± 24.18 n=24. **(D)** Images and **(E)**, quantification of the BRP ring diameter at *Drosophila* neuromuscular junctions with superresolution light microscopy (STED) for control (159±22 nm (n=12)) and Arl8 overexpression (170±25 nm, (n=12)), showed non-significant effects on ring diameter. Scale bar: 100 nm. **(F-H)** Increased PLV

delivery facilitates neurotransmission. **(F)** Two electrode voltage clamp electrophysiological recordings show **(G)** increased eEJC amplitudes at Arl8 overexpressing synapses (control: -78.24 ± 4.61 nA n=10, Arl8-OE -101.0 ± 8.85 nA n=9). **(H)** unaltered paired pulse ratio in synapses from transgenic flies (control 1.231 ± 0.03 s n=10, Arl8 OE 1.110 ± 0.05 s n=9). **(J-K)** Mini amplitude remained unchanged (WT -0.86 ± 0.05 nA, n=10, Arl8 OE -0.84 ± 0.01 nA, n=10 NMJs) and mini frequency was not significantly different (WT 1.84 ± 0.3 Hz n=9, Arl8 OE 2.15 ± 0.23 Hz, n=10 NMJs). Statistics: All graphs show Mean ± SEM. Mann-Whitney test. *P<0.05, ** P<0.01, *** < 0.001, n.s. for not significant. Arl8 OE confocal data were acquired and analyzed together with Dr. Astrid Petzoldt. Eric Reynolds performed the electrophysiological recordings.

Electrophysiological recordings of Arl8 OE larvae, most interestingly, showed elevated evoked neurotransmission (Fig. 17 F-G), whereas the paired pulse ratio, mini amplitude and frequency remained unchanged (Fig. 17 H-J).

All together, we have been able to show that Arl8 gain-of-function is capable of increasing the amount of BRP that is transported to the synapse and this facilitates synaptic activity without modifying the AZ scaffold architecture. Therefore Arl8 is sufficient to boost neurotransmission by facilitating transport of PLVs and presynaptic biogenesis.

Axonal co-transport of AZ and SV proteins in PLVs hippocampal neurons

The machinery for presynaptic neurotransmitter release is evolutionary highly conserved from invertebrates to mammals (Haucke et al., 2011; Schoch and Gundelfinger, 2006; Südhof, 2012). We therefore asked whether the role of Arl8 in presynaptic biogenesis in *Drosophila* is conserved in the mammalian nervous system, using cultured hippocampal neurons as a model (see Methods). We monitored the axonal transport of presynaptic AZ proteins in developing mouse hippocampal neurons co-expressing GFP- or mCherry-tagged variants of the AZ scaffold Bassoon (Bsn) (Dresbach et al., 2006; Maas et al., 2012) together with the lysosomal markers Lamp1 or Arl8. Analysis by live imaging revealed a striking co-localization and co-transport of GFP-Bsn with Lamp1 or Arl8 (Fig. 18 A-B), suggesting that presynaptic biogenesis in hippocampal neurons occurs by axonal transport of PLVs, similar to what we had observed in *Drosophila* (compare with Fig. 8).

Consistent with this hypothesis, fluorescence recovery after photobleaching (FRAP) experiments revealed the delivery of Lamp1- and Bsn-containing PLVs to presynaptic boutons (Fig. 18 C), similar to what was seen at *Drosophila* NMJs (compare Fig. 10 C-F). Moreover, overexpression of Arl8 facilitated axonal transport of GFP-Bsn, as evidenced by its depletion from the neuronal soma and axon initial segment (AIS) when compared to control neurons (Fig. 18 D). Conversely, when the expression level of Arl8A, one of the two mammalian isoforms of Arl8 expressed in the brain (Rosa-Ferreira and Munro, 2011) was reduced, we observed a partial accumulation of GFP-Bsn in the neuronal soma and the AIS (Fig. 18 E). These results indicate that the role of Arl8-mediated anterograde transport of PLVs in presynaptic biogenesis is similar in invertebrates and mammals. That means not only that PLVs and the machinery here described appeared in evolution at least as long ago as the common ancestor from invertebrates and mammals but also that there has been evolutionary pressure to conserve it.

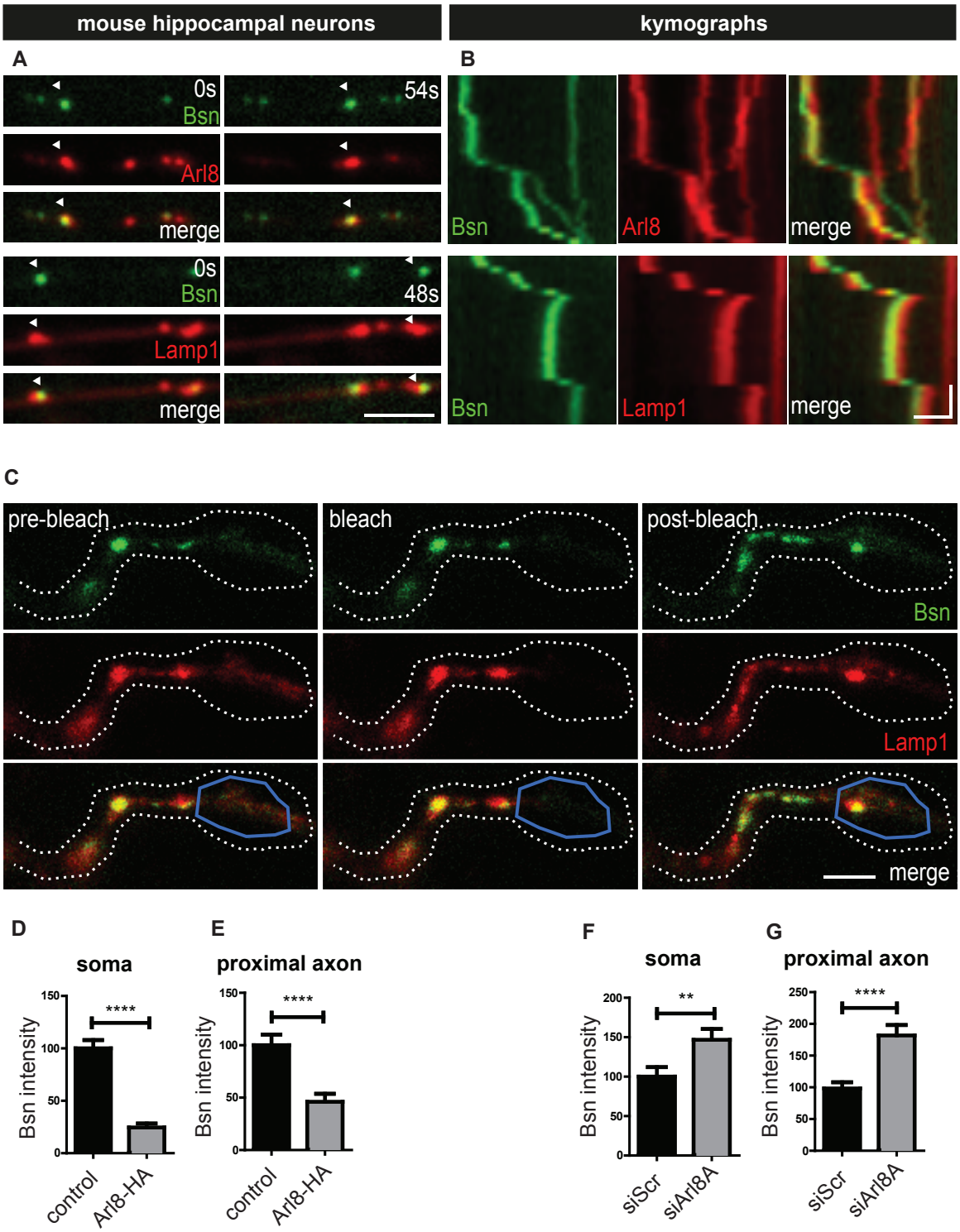

Fig. 18 | Axonal co-transport of AZ and SV proteins in PLVs in mouse hippocampal neurons.

(A,B) Anterograde transport of the AZ scaffold Bassoon (Bsn) with lysosomal markers Lamp1, and Arl8 in axons of hippocampal neurons. Live confocal imaging of living mouse hippocampal neurons (DIV9) co-expressing GFP-Bsn (95-3938) with lysosomal markers Arl8B-mCherry or Lamp1-mCherry. (A) Single frames and (B) kymographs illustrating co-transport of GFP-Bsn (95-3938) (green) and Arl8B-mCherry or Lamp1-mCherry (red)

along the axon. (A) Images on the left marks the position of the trafficking organelle at time point 0, images on the right mark the position of the trafficking organelle after 48 s or 54 s. Scale bar, 2 µm. (B) Kymographs depict the trajectories of GFP-Bsn (95-3938) co-transported with Arl8B- mCherry (upper panels) and Lamp1-mCherry (lower panels). Scale bar, 1 µm, 12 s. (C) Presynaptic delivery of GFP-Bsn (95-3938) / Lamp1-mCherry vesicles to presynaptic terminals visualized by fluorescence recovery after photobleaching (FRAP) experiments. Single frames from live-imaging of mouse hippocampal neurons (DIV6) co-expressing Lamp1-mCherry and GFP-Bsn (95-3938). Left panels: Axon terminal highly co-positive for PLVs (Lamp1) carrying AZ cargo GFP-Bsn (95-3938). Middle panels: Fluorescence within the axon terminal was bleached in the red and the green channels (ROI marked in blue). Right panels: Illustrate *de novo* delivery of Bsn/ Lamp1-containing PLVs. Scale bar, 5 µm. (D) Arl8 overexpression in hippocampal neurons facilitates PLV-mediated transport of GFP-Bsn (95- 3938) from soma and proximal axons. Quantification of representative data shown in Fig. 18 C. Levels of Bsn in soma of control neurons are normalised to 100. GFP-Bsn (95-3938) levels were decreased in the soma (control 100 ± 8, Arl8 OE 25 ± 4 each N=60 neurons from n=3 independent experiments) and proximal axon (control 100 ± 10, Arl8 OE 46 ± 8 each N=60 neurons from n=3 independent experiments) of Arl8 overexpressing neurons compared to control transfected neurons. Mann-Whitney test was used for statistical analysis, **** $p < 0.0001$. (E) Reduced PLV transport in hippocampal neurons partially depleted of Arl8A results in accumulation of GFP-Bsn (95-3938) in neuronal somata and the proximal axon. Quantification of representative data shown in Fig. 18 D. Depletion of Arl8A led to increased GFP-Bsn (95-3938) levels in the soma (siScr 100 ± 12 N=75 neurons from n=4 independent experiments, siArl8A 147 ± 14 N=79 neurons from n=4 independent experiments) and proximal axon (siScr 100 ± 10 N=75 neurons from n=4 independent experiments, siArl8A 181 ± 17 N=79 neurons from n=4 independent experiments) compared to scrambled siRNA-treated control neurons set to 100). Mann-Whitney test was used for statistical analysis, **** $p < 0.0001$, ** $p = 0.0021$. Quantifications presented as mean ± SEM. Data are shown for illustration and were provided by Dr. Christoph Ott and Dennis Vollweiter, within the framework of our collaboration.

AZ and SV protein-containing PLVs accumulate in neuronal somata of *arl8* mutants

So far we had evidence from Drosophila larvae that Arl8 is important to deliver cargo to the synaptic terminal and when larvae lacked Arl8 there was an important deficit of AZ and SV proteins at the presynapse. We had seen also how axonal transport of BRP as well as Lamp1 was severely affected in Arl8 mutants, with the almost total absence of anterograde cargo moving (Fig. 10 E-F). At the same time, we observed paired phenotypes in cultured hippocampal neurons from mice. There, accumulation of AZ proteins in the neuronal soma and AIS of neurons depleted of Arl8A was observed (Fig. 18) together with a corresponding reduction of Bassoon intensity from the soma and AIS when Arl8 was overexpressed in hippocampal neurons (Fig. 18).

These results together suggested us that in the absence of Arl8 function, PLVs and therefore also the AZ proteins contained in them may accumulate in the cell bodies of motoneurons from *arl8* mutant animals. To test that, we decided to look at the Ventral Nerve Cord (VNC) of wild-type larvae and compare them with *arl8* mutants.

Analysis of larval brains from WT showed that BRP was not equally distributed along the VNC. The BRP signal was very high in the area that corresponds to the Neuropile, and almost nothing in the area where the cell bodies of motoneurons are located. A more detailed and closer look at it, however, unveiled small dot like structures that are indeed present in the motoneuron cell bodies of wild type animals. When the VNC of *arl8* mutants was scanned, it was very clear that there was a very important accumulation of BRP in this same region. As it can be seen in (Fig. 19 A) and was quantified in (Fig. 19 B) there is a two fold increase in BRP signal in *arl8* mutants (227.3 ± 35.14) compared to wild type (100 ± 18.48). That was a clear indication that in the absence of Arl8, PLVs and their protein cargo cannot be shipped out from the cell body and consequently accumulate in the cytoplasm.

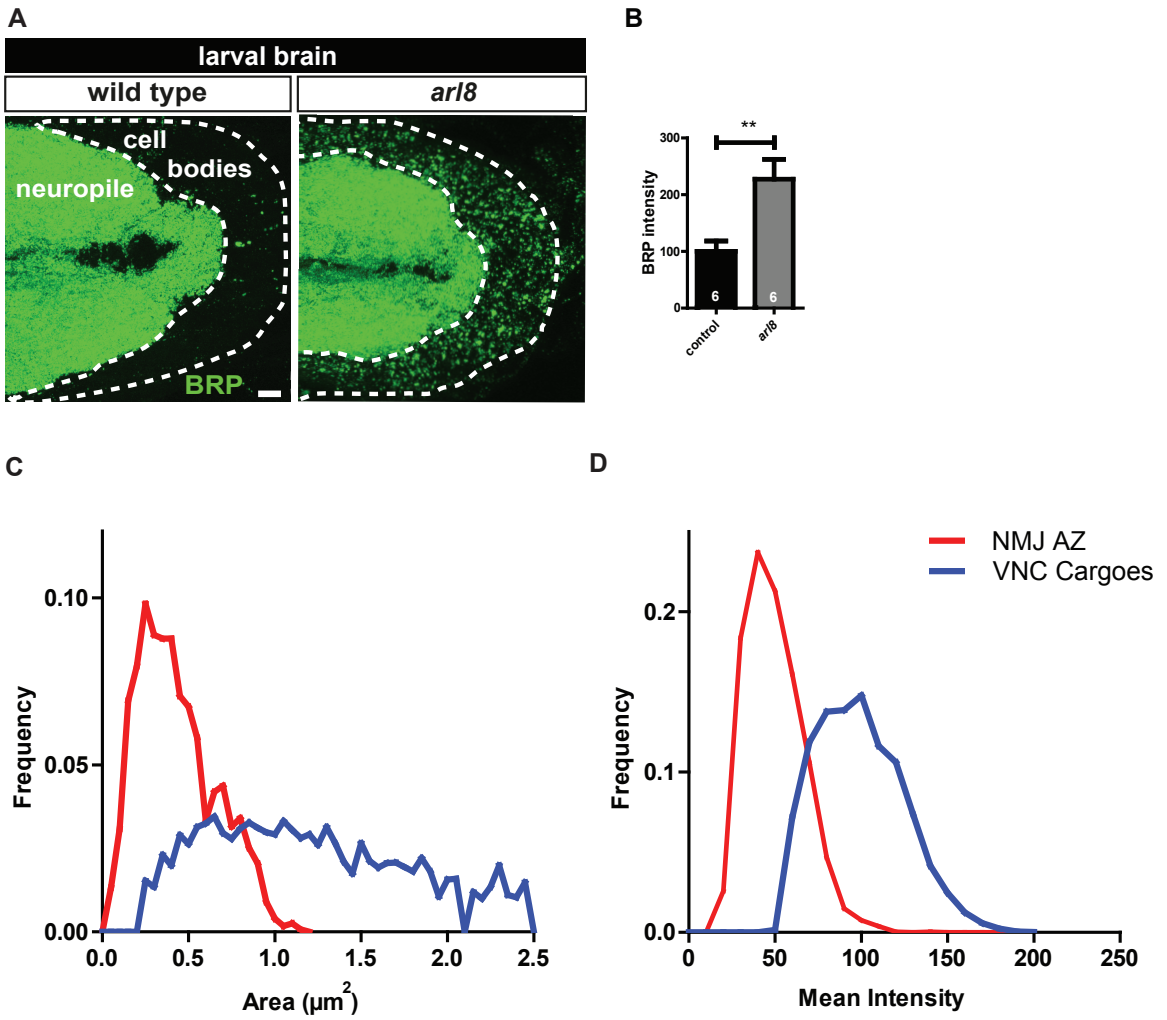

Fig. 19 | BRP accumulates in neuronal somata of *arl8* mutants.

(A,B) Accumulation of BRP in motoneuron somata of *arl8* mutant *Drosophila* larvae. **(A)** Confocal images of ventral nerve cords (VNCs) from wild-type (WT) and *arl8* mutant *Drosophila* larvae immunostained for BRP. Note the dramatic accumulation of BRP at the VNC cortex (delineated by dotted lines). Scale bar 100 µm. **(B)** Quantification of representative data shown in (A). WT (mean normalized to 100): 100 ± 18.48, *arl8* mutant: 227.3 ± 35.14. Data are mean ± SEM. Mann-Whitney test, ** P<0.01. **(C)** Quantification of the area of the cargoes accumulating in (A) compared to BRP AZ size distribution of WT NMJ terminals plotted as a Histogram (n=3 *arl8* VNC and n=3 WT NMJs). **(D)** Similar to (C) but showing frequency distribution of mean intensity of each cargo (n=3 *arl8* VNC and n=3 WT NMJs).

One hypothesis that seemed plausible would be that these accumulations could correspond to AZ packages. On one hand it could be that AZs form ectopically, this has been reported to be the case of *srpk79D* mutant axons (Siebert et al., 2015), but in the Arl8 it would happen one step earlier, that is in the cytoplasm. That seems unlikely

because i) even that in less amount, they are also found in wild type and ii) because they are way too abundant. On the other hand, it could be that these accumulations coincide with AZ packages that are just the building blocks of the future AZ. That would imply that the AZ are to some extend already preassembled in cargoes at the cytoplasm and when they arrive at the synaptic terminal they can be easily incorporated to an existing AZ or form a new one from scratch. This second option was also favored by the fact that some of the AZ components have been reported to be co-transported, like it is the case of BRP and RBP (Fig. 5 A)(Siebert et al., 2015), and also Unc13A and Syt-1 together with BRP in this thesis (Fig. 5 B-C).

To test whether this was the case, we measured the area of BRP accumulations found at the VNC and compared them to the ones of single AZs found at the NMJs. If they correspond to AZ packages they should have the same size. What we found was that AZs had a relatively narrow size distribution peaking at 0.45 μm^2 whereas the accumulations seen at the VNC were much bigger, with 80% of the cargoes at the VNC were bigger than 0.6 μm^2 (Fig. 19 C). When we measured the intensity of BRP dots at the VNC we obtained similar results (Fig. 19 D). The relative intensity in the VNC cargoes was on average two fold higher than the ones of a single AZ at the NMJ (Fig. 19 D). These results taken together seem to indicate that these accumulations do not correspond to preassembled AZ packages, but rather they contain the amount of protein for more than one AZ. However, to really be able to say that, we would need a better understanding on what the PLVs do when they arrive at the synaptic terminal, and how exactly is the process and the stoichiometry of the construction of new AZ (or remodeling of old ones) performed.

Next, we wanted to see whether the accumulation of BRP in the VNC was also followed by the proteins found in lower amounts at the NMJ. For that we tested Dap160, VGlut and also the AZ scaffold associated release factor Unc13A. And indeed, a similar accumulation was observed for these proteins (Fig. 20 A-F). Interesting to notice was how VGlut accumulation was found not all over the area corresponding to motoneuron cell bodies, but only in a delimited area: this area corresponds to the cell bodies of glutamatergic motoneurons, the only ones that use Glutamate as neurotransmissor and thus express VGlut. The rest of motoneurons surrounding do not express VGlut and therefore did not show immunoreactivity (Compare Fig. 20 E left and right panels).

To additionally check for specificity of the Arl8 phenotype, we used again the Arl8 RNAi line and this time we imaged the VNC. Not surprisingly we saw that there was an increase in BRP signal in the area where the motoneuron cell bodies are located. Note

that in this case the accumulation is restrained to some neurons again. The OK6-GAL4 driver line is not a pan-neural driver line and therefore Arl8 RNAi is only expressed in motoneurons. The surrounding cells do not accumulate BRP because their Arl8 is not suppressed.

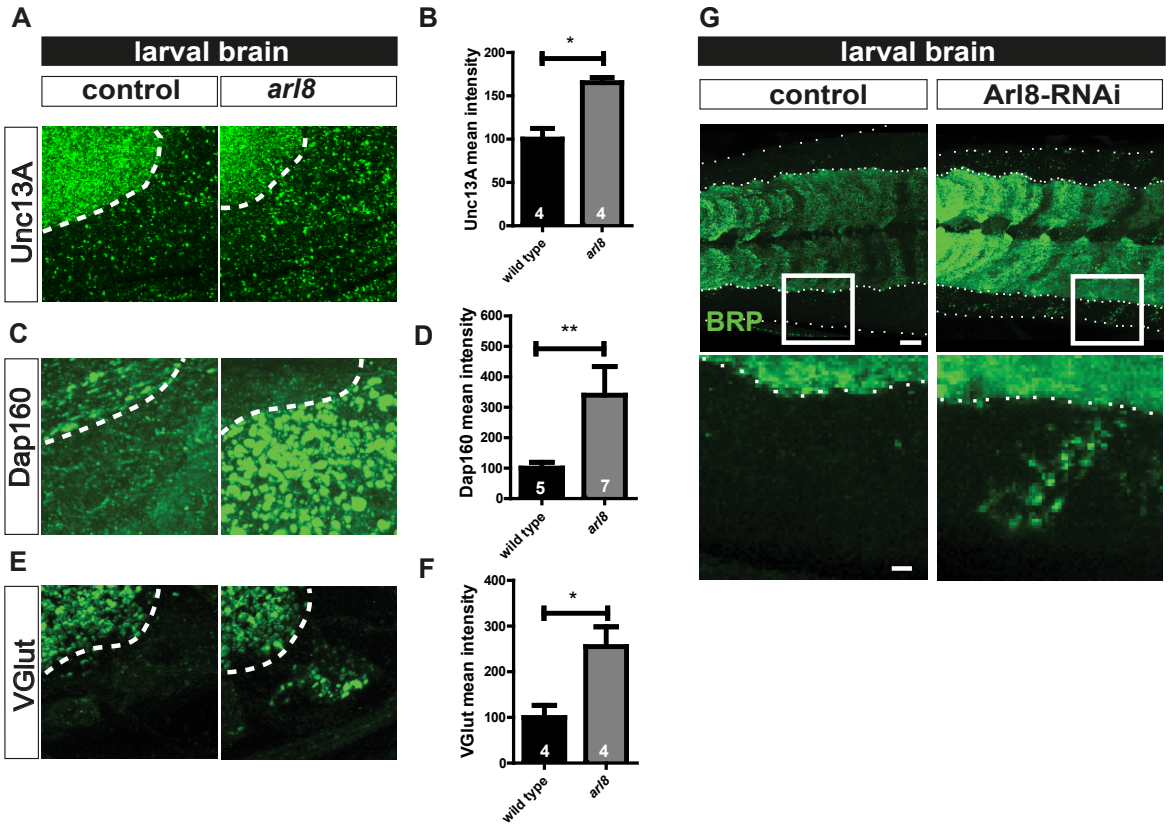

Fig. 20 | Accumulation of presynaptic protein containing PLVs in the neuronal soma of *arl8* mutants.

(A,C,E) Accumulation of several major presynaptic components in motoneuronal somata of 3rd instar *Drosophila arl8* mutant larvae. Confocal images of VNC (white dashed line indicates the border between neuropil and motoneuronal soma) from wild-type (WT) and *arl8* mutants with a strong accumulation of **(A)** UNC13A (green), **(C)** Dap 160 (green), **(E)** VGlut (green) in absence of Arl8. Scale bar, 100µm. **(B,D,F)** Quantification of representative data shown in (A,C, E). A strong increase can be observed for **(B)** UNC13 mean intensity (WT=100 ± 12.46, *arl8* mutant 165.2 ± 5.87 (n=4)), **(D)** Dap160 total intensity (WT=100 ± 19.35 (n=5), *arl8* mutant 339.6 ± 94.26 (n=7)) and **(F)** VGlut mean intensity (WT=100 ± 26.33 (n=4), *arl8* mutant 255.3 ± 43.27 (n=4)). **(G)** Spatially restricted downregulation of Arl8 by RNAi caused a strong accumulation of BRP in stripes representing motoneuronal somata. Confocal images of the wild-type (WT) and *arl8* mutant motoneuronal somata stained for BRP (green). Top panel for overview (scale bar, 150 µm) and bottom panel for zoom (scale bar, 30 µm), WT left panel, Arl8-RNAi right panel. Dr. Astrid Petzoldt characterized the Arl8 RNAi line.

Accumulation of large vesicles distinct from SV within motoneuron cell bodies

To better define the nature of the cargoes that transport BRP, Syt-1 and contain Lamp1 and Spinster we performed Electron Microscopy (EM) on VNC samples of wild type and *arl8* mutants. So far we had seen:

1. Arl8 is needed for delivery of BRP and other AZ proteins to the synaptic terminal
2. Arl8 mutants show immobile Lamp1 and BRP cargoes within motoneuron axons
3. BRP and other AZ proteins accumulate at the cell bodies of motoneurons

By doing EM we wanted to address the following questions. If BRP and Syt-1 are transported in PLVs, is it possible to identify them morphologically at the VNC? In *arl8* mutants, are PLVs formed and not shipped out, or maybe PLVs cannot form and the BRP accumulation is because they cannot find their cargo. Would it be possible to see an accumulation of morphologically distinct vesicles that would correspond PLVs at the VNC of *arl8* mutants?

Electron microscopy allows to image samples much below the resolution of light microscopy due to the shorter wavelength of electrons (See Materials and Methods for further details). In collaboration with the group of Thorsten Mielke from the Max Planck for Molecular Genetics and their EM facility we scanned VNC samples of wild type larvae and compared them to *arl8* mutants.

We found that the overall morphology of the motoneurons was not very much affected. In wild type animals, motoneurons are round with a round nucleus, in *arl8* however both look a bit wrinkled and wizened but they are similar in size and otherwise look normal (not shown).

A closer look at the cytoplasm revealed a massive accumulation of vesicles in the cytoplasm of *arl8* mutant motoneurons. These vesicles, we categorized as our PLVs could be also found in wild type animals but to a much lower degree. In both cases, but easier to see in *arl8* mutant images because of the high abundance of vesicles, the PLVs ranged from quite clear filling to more of a dense core. We speculate that this might be related to the maturation process of the PLVs.

To better categorize these vesicles as PLVs we measured their diameter. SV have a characteristic and well defined diameter of 40 nm (Zhang et al., 1998). One possibility

we wanted to exclude or verify is that the accumulation of vesicles at the VNC are in fact Synaptic Vesicles that either cannot be transported out of the cell body or that in an aberrant manner form there because of the abundance of material that is not shipped out. For that we measured the cargoes accumulating at the cell bodies of motoneurons at the VNC and compared them with identifiable SV that are to be found at the synapses of the neuropile. The results confirmed that our cargoes were not SV. Indeed the PLVs had an average diameter of 70 nm (Fig. 21 C), compared to the below 40 nm average diameter of the SV found at the neuropile.

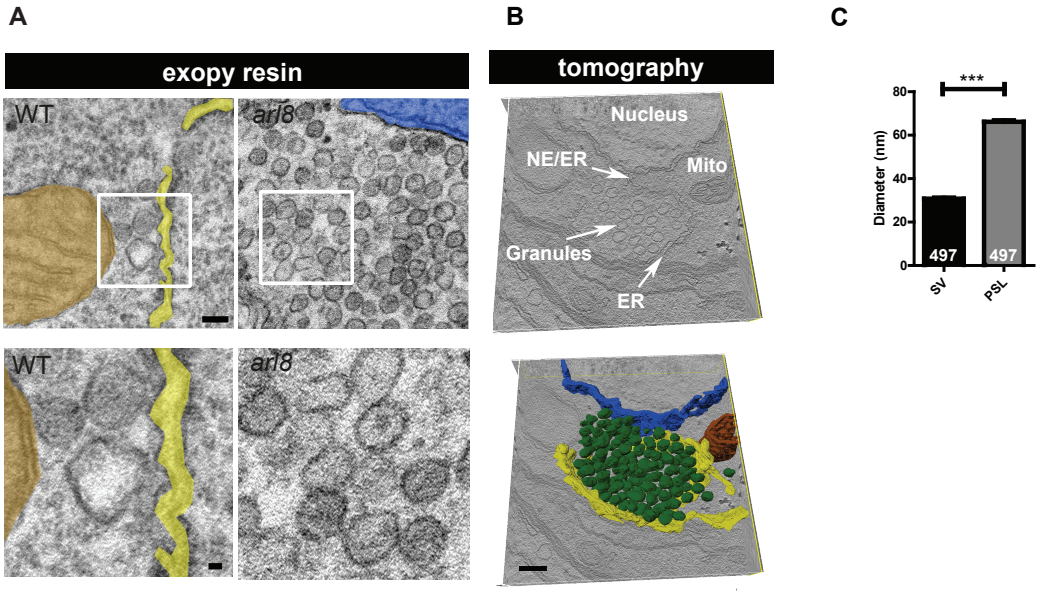

Fig. 21 | PLVs accumulate in the neuronal somata of *arl8* mutants.

(C) Electron micrographs of neuronal somata from wild-type (WT) and *arl8* mutant larval brains. Blue, nucleus; brown, mitochondria; yellow, endoplasmic reticulum. Note the massive accumulation of PLVs with or without electron-dense cores in neuronal somata of *arl8* mutants (right). In somata from WT animals (left) PLVs were very rarely detected. Scale bar, 100 nm (top), 20 nm (bottom). **(D)** 3D electron tomography analysis of PLV accumulations in neuronal somata. 3D tomogram segmentation from *arl8* mutant neuronal soma reveals a striking accumulation of spherical organelles (PLVs). PLVs show a specific morphology and are clearly distinct from other organelles. Blue: nuclear envelope, brown: mitochondrion, yellow: ER, green: PLVs. Scale bar, 300 nm. **(E)** Mean diameter of PLVs and synaptic vesicles (SVs) from the same preparation. PLV, 66.19 nm ± 0.59 (n = 497 vesicles); SV, 30.74 nm ± 0.41 (n = 497 vesicles). PLVs are, thus, distinct from SVs. EM embedding and image acquisition was performed in collaboration with Dr. Dmytro Puchov and Svea Hohensee.

We have so far shown that BRP accumulations in the soma of motoneurons correlated with a striking accumulation of homogeneously sized 70 nm in diameter vesicular structures of varying electron density, consistent with prior reports of both clear (Yonekawa et al., 1998) and electron-dense vesicles (Shapira et al., 2003; Zhai et al., 2001) as presynaptic transport packets. To reveal the relationship of these vesicles to other organelles we used electron tomography to reconstruct neuronal somata (Fig. 21 B). This analysis demonstrated that PLVs form a closely packed perinuclear array (Fig. 21 B), consistent with recent light microscopy data (Dresbach et al., 2006; Maas et al., 2012), that was distinct from other organelles such as SVs (Fig. 21 A-C), the endoplasmic

reticulum or mitochondria and bore no resemblance to the Golgi complex or to Golgi-derived dense core vesicles.

PLV accumulation at the VNC correlates with BRP and VGlut immunoreactivity

On one hand immunofluorescence light microscopy had revealed that presynaptic proteins like VGlut, BRP and Syt-1 accumulated at VNC in absence of Arl8. On the other hand EM revealed that there were vesicles of a defined size accumulating in the same region. What we wanted to know next is, are BRP and Syt-1 sitting on these vesicles and therefore we have identified the cargo that transports them? Or on the contrary, BRP accumulates at the VNC but not really on the vesicles we observe with EM, but elsewhere? The second hypothesis would mean Arl8 is transporting the vesicles and also BRP, but not together. The first hypothesis would mean that BRP is transported in a membranous cargo, that is 70 nm on average in diameter and it would imply PLVs are the long sought-after axonal transport packets for assembly of the presynapse.

To test that, we turned to correlative light and electron microscopy (CLEM) to characterize the organelles at the molecular and ultrastructural level at the same time. CLEM combines the advantages of light microscopy (LM) with the advantages of electron microscopy. It allows seeing biological processes that are easier to identify with LM without losing resolution that can be obtained with the higher resolution EM provides. In other words, it combines the two strengths of each technique.

We therefore did CLEM in VNC samples of *arl8* mutant larvae and checked whether our synaptic proteins VGlut and BRP were accumulating together with PLVs. As expected we found that BRP and VGlut immunoreactivity was enriched in the areas of the motoneuron cell body where there was an accumulation of vesicles, as it can be seen in (Fig. 22 A-B).

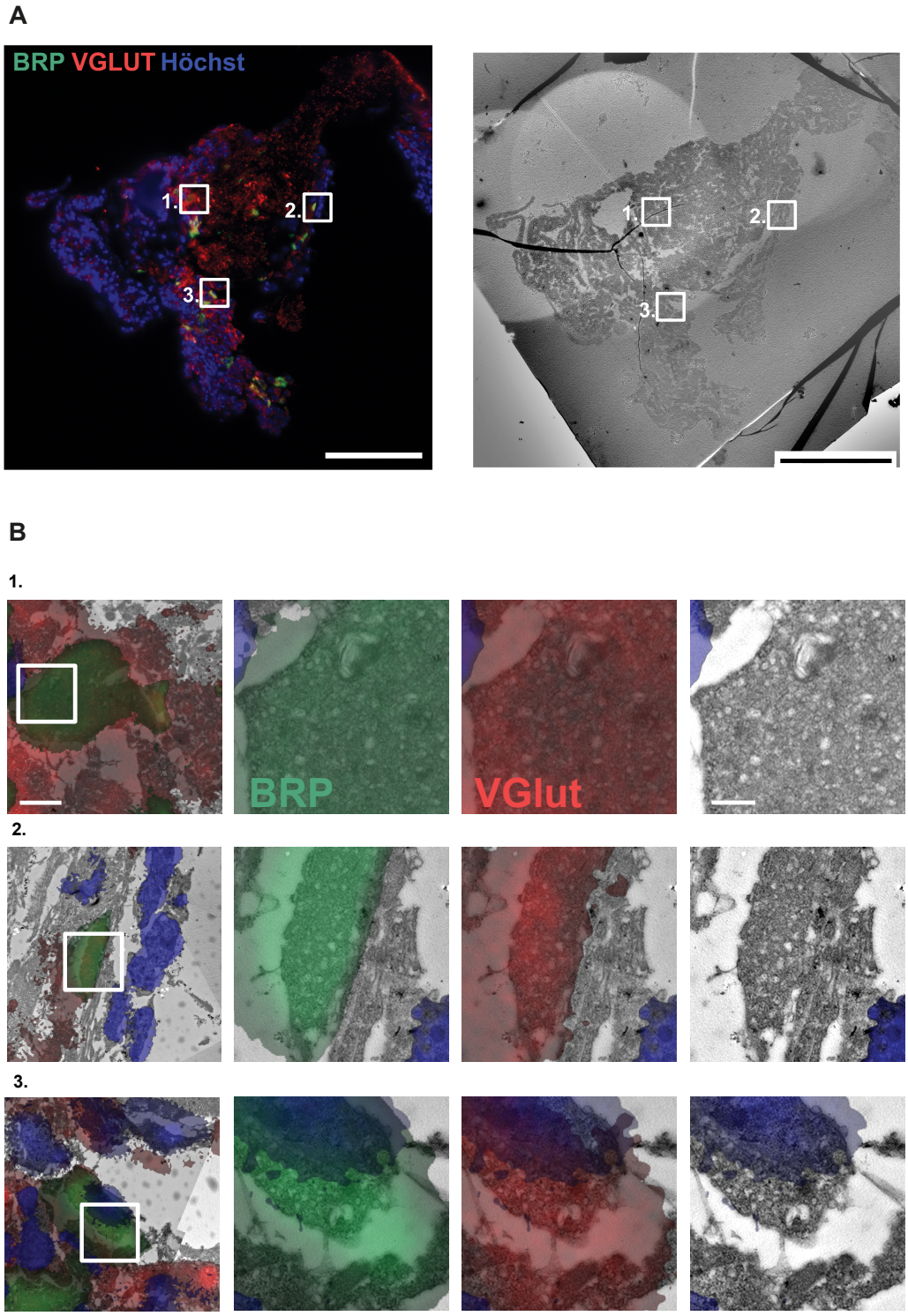

Fig. 22 | Correlative Light Electron Microscopy of *arl8* mutant VNC.

(A) Light microscopy image of semithin frozen section through the *arl8* mutant brain stained for BRP ("last- 200 antibody", 488) and Hoechst, and corresponding electron micrograph of ultrathin section. **(B)** Inserts i, ii, iii show blow-ups of the aligned light and electron microscopy images. Note that intense green BRP signal is associated with PLVs found in somata of neurons. Scale bars for light and EM: 50 µm, for second row scale bar

is 5 µm and for the third is 0.5 µm. EM embedding and image acquisition was performed in collaboration with Dr. Dmytro Puchov and Svea Hohensee.

To further test our hypothesis we performed immunogold labeling in EM samples. Briefly, 10 nm diameter gold particles were coupled to a secondary antibody that recognized the epitope, and they could be visualized as very dense punctae in the ultrathin Tokuyasu sections (Tokuyasu, 1973). Again we stained both the VNC of control and *arl8* mutant larvae. In both genotypes we could see specific presence of gold particles in the same area where vesicles were found. This was best seen in the *arl8* mutant VNC because of the prominent accumulation of vesicles and because there were more BRP accumulating too (Fig. 23 A). As it can be seen in (Fig. 23 A) gold particles labeling BRP and Syt-1 located preferentially to the area where also vesicles accumulated. As we were expecting, the BRP accumulations in neuronal cell bodies correlated with the accumulation of morphologically identifiable organelles in *arl8* mutant neurons at the ultrastructural level.

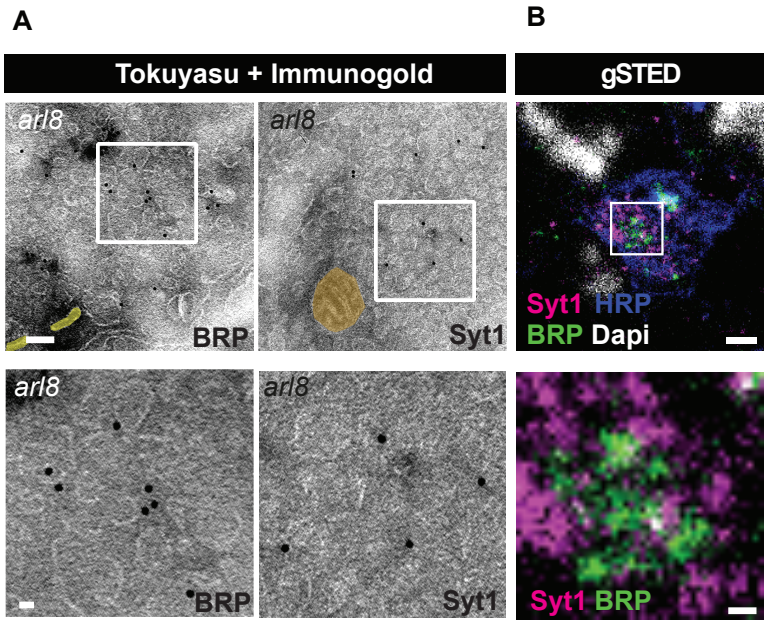

Fig. 23 | Immunogold on Tokuyasu samples reveals BRP and Syt-1 in PLVs.
(A-B) PLVs contain SV markers and are associated with AZ proteins. **(A)** Frozen ultrathin sections according to Tokuyasu from neuronal somata of WT and *arl8* mutant larval brains stained for BRP or synaptotagmin 1 (Syt-1) and decorated with 10 nm immunogold particles. Scale bar, 100 nm (top), 20 nm (bottom). **(B)** Multicolor gSTED microscopy of immunolabelled ultrathin sections (150 nm) from neuronal somata of WT and *arl8* mutant

larval brains stained for HRP (blue as a membrane marker), BRP (green), and synaptotagmin 1 (Syt-1, magenta). DAPI stained nuclei are shown in white. BRP is directly apposed to Syt-1- containing PLVs. Scale bar 100 nm. Tokuyasu samples were done in collaboration with Dr. Dmytro Puchov and Dr. Martin Lehamn acquired the STED images on the ultrathin sections.

Moreover, we also performed dual-color super-resolution imaging with gSTED microscopy in the ultrathin preparations and we could see how Synaptotagmin-1 containing vesicles are clustered around BRP punctae (Fig. 23 B).

All these data taken together further corroborate the first hypothesis of BRP and Syt-1 being transported together in the 70 nm diameter cargo vesicles that could be seen using EM resolution. These cargoes are transported by Arl8 and share resemblances with lysosomes and hence we named them Presynaptic Lysosome-derived Vesicles.

Discussion

Discussion

In the first part of this thesis we presented the tools we established to represent and analyze axonal transport using kymographs. These tools have been useful to quantitatively characterize Neurexin axonal transport in wild type and *aplip-1* mutant background. At the same time, they helped us to visualize processes related to the recycling pathways in neurons, and through them, we discovered a new and unexpected role of lysosomes for synaptic biogenesis.

The collective data presented in the second part of my thesis based on live imaging of *Drosophila* larvae, genetic analysis, electrophysiology as well as super-resolution light and electron microscopy revealed an unexpected role for a new lysosomal related organelle. We have identified and characterized a new type of vesicle that transports precursors of SV and AZ proteins and that is needed for synaptic biogenesis. This new cargo named Presynaptic Lysosome-derived Vesicle (PLV) has been identified both in Drosophila larvae and in developing hippocampal neurons of mice, indicating that this is an ancestral trait of neuronal axonal transport and that the mechanism has been evolutionary conserved across the animal kingdom. All our data presented here suggest that PLVs represent the long sought-after precursor organelles for presynaptic biogenesis (Ahmari et al., 2000).

Analysis of Neurexin axonal transport with Kymographs

The long-range transport of Neurexin from the cell soma is required for proper active zone formation and maturation (Owald et al., 2010, 2012; Muhammad et al., 2015). In the present work we have established the tools to quantify axonal transport and we have compared axonal transport of Neurexin in wild type versus the *aplip-1* mutant, known for displaying axonal aggregates of synaptic proteins (Siebert et al., 2015). Our results indicate that Aplip-1 is needed for proper processivity of both anterograde and retrograde transport of Neurexin, and we have found that *aplip-1* mutants display more stationary cargoes. These findings are in accordance with previous published works for the Aplip-1 orthologue in mammals, JIP-1, which has been found to interact with both Kinesin and Dynein (Fu and Holzbaur, 2013). Future experiments could use the tools here presented to analyze other axonal transport mutants and/or try to understand better the connection between regulation of Kinesin and Dynein and defects in synapse assembly or synaptic function.

Autophagosome formation and acidification at the synaptic terminals

Recent publications have highlighted the link between autophagy and synaptic maintenance and homeostasis (Gupta et al., 2013; Liang and Sigrist, 2018). In this regard, we tried to gain understanding on the process of autophagy at the synaptic terminal of Drosophila motoneurons by in vivo characterizing proteins of the lysosomal-autophagosomal pathway.

Image acquisition over long periods of time was able to report for *de novo* formation of autophagosomes at synapses. Interestingly, autophagosomes not only form at NMJ but they also undergo maturation. Indeed we were able to see how acidic lysosomes arrive to the synaptic terminal too. Co-expression of lysosomal markers with autophagosomal proteins could reveal fusion events between them. Indeed we were able to show how lysosomes enter the synaptic terminal and move anterogradelly until fusing with an autophagosome. Furthermore, using a double-labeled probe for the autophagosomal protein ATG8 we were able to evaluate the acidification of these autophagosomes. Acidification is one of the key steps for autophagosome maturation and protein degradation, and depends on lysosomal fusion (Maday et al., 2012; Moreau et al., 2011). How degradation is regulated in neurons is under discussion (Jin et al., 2007). With the double tagged ATG8 we were able to show that after lysosome fusion autophagosomes acidify in a time window of 30-40 minutes (reported by a decrease in GFP/RFP ratio).

These important findings motivate for future experiments. It would be interesting to see how autophagosome *de novo* formation as well as maturation are affected in previously described mutants of the degradation pathway like Spinster, Lamp1 or Sytanxin-17 (the SNARE protein for lysosome autophagosome fusion). This could as well extend to Aplip-1, or it could be compared in different dietary conditions, as well as used as an assay for drug regulation of the process.

Definition of a new cargo

Presynaptic assembly requires anterograde axonal transport of synaptic proteins from the cell soma of neurons to the synaptic terminals (Klassen et al., 2010). This transport is a challenge for neurons because the distance until the synaptic terminal is up to two or three dimensions greater than usual cellular transport. Moreover, the synapse is a highly specialized structure that requires specific synaptic proteins like BRP or Syt-1 as

well as ubiquitious organelles like mitochondria. How this processed is organized and regulated is still fairly poorly understood.

While actually trying to comprehend better how AZ proteins are recycled via degradation pathways, to our surprise we found anterograde BRP co-transported with markers of the lysosomal pathway. Lamp1 and Spinster proved to be on the same organelle as BRP is. Investigating further into organelle identity we found that Syt-1, the SV marker, was transported together with BRP and it could be observed also with the lysosomal markers, demonstrating that AZ, SV and lysosomal proteins are to be found in a previously not described cargo we named PLV.

Many of the most important players of the presynapse scaffold have been identified in the last years. All these proteins accomplish fine tune synapse transmission by interacting with each other, and the stoichiometry of these proteins is fundamental for proper function. How exactly this stoichiometry is achieved, remains unclear. Recent studies have shed light on it at the synapse level. For example, Syd-1 has been shown to stabilize Neurexin at the presynaptic NMJ to control synapse formation. Syd-1 mutants have smaller terminals with fewer but bigger AZs. On the other hand, negative regulators of AZ assembly have been as well described. Spinophilin can bind to Neurexin C-Terminal part and promote its disassembly, in an antagonistic manner to Syd-1. As expected, Spinophilin mutants have more but smaller AZs. In this thesis, we show that this process can be regulated upstream of it, already before the cargoes can leave the cell soma (Muhammad et al., 2015; Owald et al., 2010, 2012).

Previous studies by the group of Prof. Dr. Craig Garner (Maas et al., 2012; Shapira et al., 2003; Zhai et al., 2001) suggested that in vertebrates, AZ proteins are transported on Dense core vesicles of around 80 nm. These vesicles, named PTV for Piccolo-Bassoon Transport vesicles, were described to transport Piccolo, Bassoon, ELKS2, Syntaxin, Unc13, RIM and N-Cadherin to nascent synapses. Interestingly, PTVs were not found to transport SV markers such as Synaptobrevin II, Synaptophysin and Synaptotagmin. Furthermore, they could establish that on average, the protein content of two or three vesicles would be sufficient to form a new AZ. In this thesis we have shown that PLVs share similarities with PTVs, but also found some differences. Similarities are that our PLVs are also responsible for transporting Bassoon, as experiments from mice hippocampal neurons showed, and transport BRP (ELKS homolog in *D. melanogaster*). PLVs when analyzed from 3D reconstruction from EM, had a 70 nm diameter and we observe some of them to have a dense core, some of them not. Our hypothesis is that this

difference in density could be related to different stages of maturation, being the denser ones the most mature. Differences in electron density may be accounted for by species-specific differences in protein content between *Drosophila* and mammalian neurons too. Another non-exclusive possibility is that neurons may be able to regulate PLV cargo content depending on the developmental stage, the type of synapse, or their physiological status (Sigrist and Schmitz, 2011), resulting in pleiomorphic vesicles of similar size, but variable AZ and SV cargo protein content. This would allow neurons to adapt presynaptic biogenesis to their needs for delivery of AZ, SV, or endocytic protein components. However, at this stage, it cannot be completely ruled out that there are other vesicles different than PTVs accumulate too. The main difference between PTVs and PLVs is that we have described PLVs as organelles related to lysosomes. Our results, although taken with caution at the beginning because they were unexpected, could be confirmed with live imaging, confocal fixed samples and EM. One could argue that since the insect homolog of Bassoon or Piccolo has not been found, talking of PTVs in *D. melanogaster* is too far reaching. However, we have demonstrated by using two distant animal models that the core mechanism of PLVs is conserved from insects to mammals. We could show how BRP in the fly and Bassoon in mice, are transported together with Lamp1, marker of lysosomes. We report too that Arl8, the motor adaptor for lysosomes, co-transports with AZ markers in both organisms and it is required for proper AZ protein delivery to the synapse. How exactly PLVs relate to PTVs remains to be determined.

Interestingly, other lysosome-related organelles have lately been shown to play a role in other biological process a part from degradation. In a recent study, a secretory lysosome-related organelle-based mechanism could be identified to mediate lumen formation during epithelial tube anastomosis in *Drosophila* (Caviglia et al., 2016). This process shares many similarities with PLVs transport: it depends on MT cytoskeleton and motor proteins, it transports membrane and proteins into the plasma membrane, the vesicles are related to the recycling pathway and curiously enough there is and Arl protein, Arl3, involved. All this suggests that the function of secretory lysosomes in the biogenesis of specialized membrane compartments may not be restricted to the nervous system but is a wide used mechanism.

PLVs deliver synaptic proteins to the synapse

Our data support the view that the presynapse is made, at least in part, as a pre-assembled functional unit with its main components, i.e. AZ and SV proteins and possibly others (e.g. endocytic proteins), being transported on a common organelle that delivers its

content to the presynapse (Ahmari et al., 2000) and, therefore, attest to the notion that vesicular transport of presynaptic AZ and SV proteins is mediated by a single type of transport organelle, the PLVs. Additionally, using in vivo imaging, we have been able to show how PLVs arrive to the synapse both in mice and flies. Interestingly, PLVs are delivered in a similar manner than DCV had previously been described (Wong et al., 2012), indeed PLVs arrive to the synaptic terminal and probably, after finding an appropriate site for unloading cargo or fusing, they remain static for some time. How this site is determined is still not known. (Wong et al., 2012) proposed a system of sporadic capture of cargoes during transport, a mechanism that is completely compatible with our findings, but sill poorly understood. Since PLVs (and DVC) have to deactivate the Kinesin motors to remain static, the process is likely to be orchestrated via motor adaptors or via a mechanism similar to the tug of war, where Kinesin and Dyein would reach an equilibrium that allows the motor to stop its motion and remain quiet (Müller et al., 2008).

It is noteworthy that a fraction of presynaptic proteins still arrives at the *arl8* mutant terminal, despite the extraordinary reduction of axonal transport. One likely explanation lies in the complexity and redundancy of axonal transport mechanisms in neurons (Füger et al., 2012). Using super resolution STED microscopy we could resolve the AZ ultrastructure and we observe that these remaining AZs in *arl8* mutants look wild type. This is the case when Arl8 is overexpressed as well. Taken together, these results indicate that Arl8 plays a role in the transport of AZ material but not at the level of cytomatrix assembly. This result is not definitive, as so far we have only looked at BRP ring diameter as a measure of AZ integrity. It could well be that other factors like RBP or Unc13-A are affected. A more detailed analysis using two color STED to visualize on the same sample different AZ markers will hopefully elucidate these unanswered questions.

The relative scarcity of arriving PLVs at the terminal makes it hard to study cargo delivery at comparable level to the studies that have used ANF as a marker for DCV. However, it will be really interesting to see to what extend PLVs delivery behaves similar to DCV, and even more interesting would be to see how the remaining AZ components arrive to the synapse in absence of Arl8. Do they follow same rules, or since they are transported differently they also behave differently? It could well be that Arl8, as a motor adaptor, plays a role in delivery too, or maybe it does not. Further experiments are required to resolve this question. Spinning disk confocal microscopy, compared to the standard confocal microscopy used in this work, could help getting closer to these questions. Spinning disk microscopy allows for higher temporal resolution and higher sensitivity and is therefore very suitable for in vivo imaging (Su et al., 2015).

Arl8 and HOPS, and other regulators

We have shown that anterograde axonal transport of PLVs requires the Ras-related GTPase Arl8, which may couple PLVs to kinesin motor proteins. Consistent with this model we find have investigated the relationship between Arl8 and the HOPS complex. The HOPS complex has been reported to mediate lysosome fusion (Balderhaar and Ungermann, 2013; Jiang et al., 2014; Takáts et al., 2014) and it is known that this Arl8 controls the assembly of HOPS into lysosomes (Khatter et al., 2015). The HOPS complex is a heterohexamer, however which role of every subunit plays is only partially understood. To compare the effects of the HOPS complex with these from the *arl8* phenotype we attempted to deplete HOPS from motoneurons. Unfortunately we could only find a functional RNAi line against one of the subunits, VPS39, and not for the rest. Using specific depletion the VPS39 subunit of the HOPS complex, we obtained a comparable result than when depleting Arl8 with the same technique. Not surprisingly, specific presynaptic down-regulation of Arl8 by RNAi also causes defective synaptic biogenesis and downregulation of VPS39 leads to a similar phenotype. This further confirmed the tight relationship between lysosomes and PTVs. Coming experiments could investigate the effects of depletion of the other subunits, via generation of functional RNAi lines or a mutant line. Most important would be to characterize the phenotype of the VPS41 subunit, first because it is solely found in the HOPS complex (other subunits might be found on other complexes) and secondly because it is the subunit that directly binds to Arl8 (Khatter et al., 2015).

PLVs axonal transport, a mechanism that can be tuned by adjusting Arl8 levels

We have seen that axonal transport is a key process for neuronal survival as well as proper function. It is remarkable the wide spectra of phenotypes one encounters when analyzing related mutants. On one side we have the tremendous effects of *khc* or *imac* mutants, which result in embryonic lethality. Following, we have the *arl8* phenotype, in which lethality is delayed until third instar larvae. *arl8* mutants have severely reduced synaptic terminals; very thin and without the typical boutons. Only few active zone are left, and although the individual remaining AZs seem to be healthy for the indicators analyzed (BRP ring diameter and SV/bouton) the overall synaptic transmission is seriously declined. After seeing that when depleting Arl8 levels by RNAi we obtained a milder phenotype, we decided to challenge the system by boosting Arl8 levels. Certainly, RNAi is

not as effective as a null mutant, and whereas the *arl8* allele produces no Arl8 protein at all, the Arl8 RNAi flies can still translate some leaking mRNA into protein, which explains the milder phenotype. Failure of axonal transport is a key factor in the development and progression of neurodegenerative disorders such as Alzheimer's disease (Julien and Millecamps, 2013; Vicario-Orri et al., 2015), therefore our findings that Arl8 overexpression can upregulate axonal transport are of great significance. Our results show how gain of Arl8 function is sufficient to increase the delivery of presynaptic components and facilitate evoked neurotransmission. As we have shown, this result was achieved without modifying the ultrastructure of single AZ. For future experiments it will be interesting to investigate in more detail if Arl8 overexpression can rescue synaptic defects caused by other mutations. First candidates could be genes that have been identified to have axonal transport defects like *aplip1* or *srpk79D* (Siebert et al., 2015), and see the resulting phenotype of combining these mutants with Arl8 overexpression.

Unpublished data of ongoing experiments in the lab, suggest that proteins like Aplip1 have a phenotype beyond regulators of transport and play a role in synaptic plasticity and learning. Therefore future experiments could assay for plasticity phenotypes of Arl8 overexpression in combination with *aplip1* or other proteins that can tune neurotransmitter release like Unc13A and Unc13-B.

Accumulation of cargoes at the VNC

One of the most satisfactory results of this work was to be able to find in the cell bodies the PLVs components that were missing at the synapse (BRP and Bassoon and SV markers). It was not obvious that this would be the case. Supporting evidence was the fact that we could observe hardly any cargo moving in *arl8* mutant background. It seemed plausible that the terminals did not obtain normal levels of presynaptic components because they failed to leave the VNC in the first place and were stalled there, but alternative hypothesis were as valid. One option could be that PLVs are not produced at all, or it could be that after not being shipped out they are recycled and degraded. With EM analysis of motoneuron cell bodies we could confirm that not only the proteins were stalled but the whole organelle, PLVs, were retained in the cell soma in big numbers. To confirm that the vesicles found with EM and the protein accumulation detected with immunohistochemistry were the same entity we performed two independent approaches.

First CLEM confirmed that the regions were the PLVs were accumulating were positive for SV and AZ markers. Second, frozen ultrathin sections were decorated with

gold particles identifying BRP and Syt-1 on PLVs, following the Tokuyasu protocol (Tokuyasu, 1973). Previous attempts at identifying AZ material together with cargoes using these techniques were not very successful in our hands because of the low abundance of PLVs in the cell somas of WT flies. Opportunely, the *arl8* phenotype with the huge accumulation of PLVs at the soma was the ideal situation to proof the power of the CLEM and Tokuyasu approaches. We hope that our results, and the capacity to use *arl8* mutants as controls will bring insightful answers to other subjects where the techniques could be useful.

Another most remarkable result of the VNC phenotype is the wide range of proteins that we could see to accumulate. From active zone marker Bruchpilot, periactive zone scaffolding protein Dap160 or the SV constituent CSP. One objection that can be expected is to say that our Arl8 phenotype is not a result of PLVs being stalled but is more of a general axonal transport deficit. Indeed Arl8 has been reported to activate unc-104 (Klassen et al., 2010), and is also needed for the transport of degradative lysosomes. Importantly, we argue that the phenotype here reported is due to PLVs and not a secondary effect of unc-104 malfunction or lower lysosomal function. Evidence for that is the fact that we could not observe any accumulation of mitochondria at the VNC in our EM samples, suggesting that a gross morphological defect was not the probable cause of the observed phenomenon. Ongoing experiments are trying to confirm that mitochondria transport is unaffected by in vivo analyzing transport of mitochondria in *arl8* mutant axons and comparing it to wild type.

To conclude, we propose that PLVs represent a specialized form of neuronal secretory lysosomal vesicles (Luzio et al., 2014; Marks et al., 2013) similar to those found in other cell types such as hematopoietic cells and melanocytes, where they mediate the secretion of chemical signals or enzymes or promote lipid turnover and facilitate membrane growth and repair (Blott and Griffiths, 2002; Luzio et al., 2007; Reddy et al., 2001; Setty et al., 2008). How the PLV-based presynaptic biogenesis pathway is segregated from 1) the conventional lysosomal pathway for protein and lipid degradation and 2) other pathways for axonal transport, is an open question. Future studies will be needed to address these open questions.

Acknowledgements

Acknowledgements

Foremost I would like to thank my supervisor, Prof. Dr. Stephan Sigrist for giving me the opportunity twice to work with him, first during my Diploma thesis and later for my PhD. My life has changed completely since I moved to Berlin and started working with him, and I am therefore very grateful.

Second I would like to thank everyone who has been around me in the last almost 5 years, for your support and friendship. Without you this work would not have been possible. I would specially like to thank my mother and my father, my sister and my two brothers. I would like to thank all my old friends from Barcelona and more recent friends from Berlin, although many have become already old friends.

I would also like to express my most sincere gratitude to all the collaborators of this project, starting with Prof. Dr. Volker Haucke with whom I am so fortunate to have collaborated. I am also in debt with all the colleagues from the Sigrist group, for their scientific discussions and for making the time in the lab more pleasant. I would like to specially thank Suneel, Varun, Karzan and Husam because they immediately became my friends when I first join the lab. Also to Dominique, Niraja, Anatoli, Eric, Thorsten, Eva and everyone in the Mitte lab for the good times we had doing science, and outside the lab.

Of course this work would have been possible with Anela, who started the project and thanks to her initial discoveries this project exists. Also to Astrid, Chrissi, Dima, Svea, Martin, Dennis and Christoph for their great contributions to the project.

Last I would like to thank Prof. Dr. Reinhard Lipowsky for his interest in this project. To Angelo and the IMPRS for their support and for funding the project. And Florian and Mehmet, and everyone in Golm for their contributions, and the fun.

Appendix

Appendix

Protocol for the Fiji macros “Kymograph” and “Velocities”

This protocol explains step by step the process of obtaining a kymograph and acqurining kinetic parameters of the trajectories plotted. For an introduction on kymographs, for what are they useful, and the concept behind using htem, see the chapter “Results - Kymographs as a tool to quantify axonal transport”.

Part 1: The code

```
//MyKymo v1.7 was written by Ulises Rey (AG Sigrist) as a tool for his PhD thesis.
//Based on a plugin by J. Rietdorf (http://imagej.net/Multi_Kymograph)


//define variables period and pixelsize. below are the ones by defect
var pixelsize=0.1
var period=0.340
var Direction="Anterograde"

----------------------------------------------------------------------------------------
function kymograph() {

	instack=getTitle();
	run("Set Slice...", "slice="+1);
	plotdata=getProfile();
	width=lengthOf(plotdata);
	height=nSlices;
	newimg="name=Kymograph width="+width+" height="+height+" slices=1";
	run("New...", newimg);kymo=getTitle();
	selectImage(instack);

	setBatchMode(true);
	for(j=1; j<nSlices+1; j++) {
		run("Restore Selection");
		plotdata=getProfile();
		selectImage(kymo);
		for(i=0; i<width; i++) {
			setPixel(i,j-1,round(plotdata[i]));
		}
		selectImage(instack);
		run("Next Slice [>]");
	}
	selectImage(kymo);
	setBatchMode(false);
}
----------------------------------------------------------------------------------------
macro 'Kymograph Action Tool - C000T1d13KT9d13y' {

	kymograph();
}
----------------------------------------------------------------------------------------
macro 'Kymograph - [c]' {

	kymograph();
}
----------------------------------------------------------------------------------------
function velocities(mode) {

print ("Vesicle ID"+"\t"+"Total time (s)"+"\t"+"average speed");
```

```
roiManager("Deselect");
// for every ROI
for (n=0; n<roiManager("count"); n++){


        //print(roiManager("count"));
        sum_dx=0;
        sum_dt=0;

//print("ROI n is "+n);
selectWindow("ROI Manager");
roiManager("select", n);
getSelectionCoordinates(x, y);
        //Array.print(x);
        //Array.print(y);
roiManager("Rename", "ROI "+n);

//print("                    roi is "+Roi.getName);

        //for every point in a single ROI
        for (i=0; i<x.length-1; i++){
        //print("point number"+i);

                //sets distance
                //print("Direction is "+Direction);
                if(Direction=="Retrograde"){
                        dx_now=(x[i]-x[i+1]);
                }

                if(Direction=="Anterograde"){
                        dx_now=(x[i+1]-x[i]);
                }

                sum_dx=sum_dx+dx_now;

                //sets time
                dt_now=abs(y[i+1]-y[i]);
                        if (dt_now==0)dt_now=1;
                sum_dt=sum_dt+dt_now;


                //if (mode=='Kymograph' ){

                        //print ("nresults"+nResults);

                        nrow=nResults;
                        setResult("vesicle ID", nrow, Roi.getName);
                        setResult("dx now", nrow, dx_now);
                        setResult("dt now", nrow, dt_now);
                        setResult("actual speed", nrow, (dx_now/dt_now));
                        setResult("dx sum", nrow, sum_dx);
                        setResult("dt sum", nrow, sum_dt);
                        setResult("average speed", nrow, (sum_dx/sum_dt));
                        //convertion
                        setResult("period (s)", nrow, period);
                        setResult("frequency (fps)", nrow, (1/period));
                        setResult("pixel size (microm)", nrow, pixelsize);
                        //real units
                        setResult("dx now (microm)", nrow, dx_now*pixelsize);
                        setResult("dt now (s)", nrow, dt_now*period);
                        setResult("actual speed (microm/s)", nrow,
((dx_now*pixelsize)/(dt_now*period)));
                        setResult("dx sum (microm)", nrow, sum_dx*pixelsize);
                        setResult("dt sum (s)", nrow, sum_dt*period);
                        setResult("average speed (microm/s)", nrow,
((sum_dx*pixelsize)/(sum_dt*period)));
```

```
                        //}
                }
                print (Roi.getName+"\t"+sum_dt*period+"\t"+((sum_dx*pixelsize)/(sum_dt*period)));
                updateResults();
}
print ("\t");
print ("ROIs:\t"+"\tTime:\t"+"\tFrequency:\t");
print (roiManager("count")+"\t"+(getWidth()*period)+"\t"+roiManager("count")/(getWidth()*period));
}

------------------------------------------------------------------------------------------
macro 'Velocities Action Tool - Cd00T1d13VT9d13' {
//requires a line selection.
//reads the selection coordinates.
//outputs to result table: y total, x total, x actual, speed actual, speed average.

        velocities('Kymograph');
//add saveAs("Results", "/Directory/Results.csv");
}

------------------------------------------------------------------------------------------
macro 'Velocities  - [v]' {
//requires a line selection.
//reads the selection coordinates.
//outputs to result table: y total, x total, x actual, speed actual, speed average.

        velocities('Kymograph');
//add saveAs("Results", "/Directory/Results.csv");

}

------------------------------------------------------------------------------------------
macro 'Velocities Action Tool Options' {
  showOptionsDialog()
}

function showOptionsDialog() {
                Dialog.create("Kymograph Options");
                Dialog.addMessage("Add the values of your recordings:");
                Dialog.addNumber("Pixel Size (microm)", pixelsize);
                Dialog.addNumber("Period (s)", period);
                Dialog.addChoice("Direction", newArray("Anterograde", "Retrograde"), Direction);
                Dialog.show();
                pixelsize = Dialog.getNumber();
                period = Dialog.getNumber();
                Direction = Dialog.getChoice();
}
```

Part 2: Installing the macros

1. Copy the whole code and save it under a Mykymo v1.7.txt file, under the toolsets directory in Fiji (e.g. /Applications/Fiji.app/macros/toolsets)
2. Open Fiji and load the MyKymo v1.7 macro by clicking on the two red arrows (More Tools) and then on MyKymo v1.7

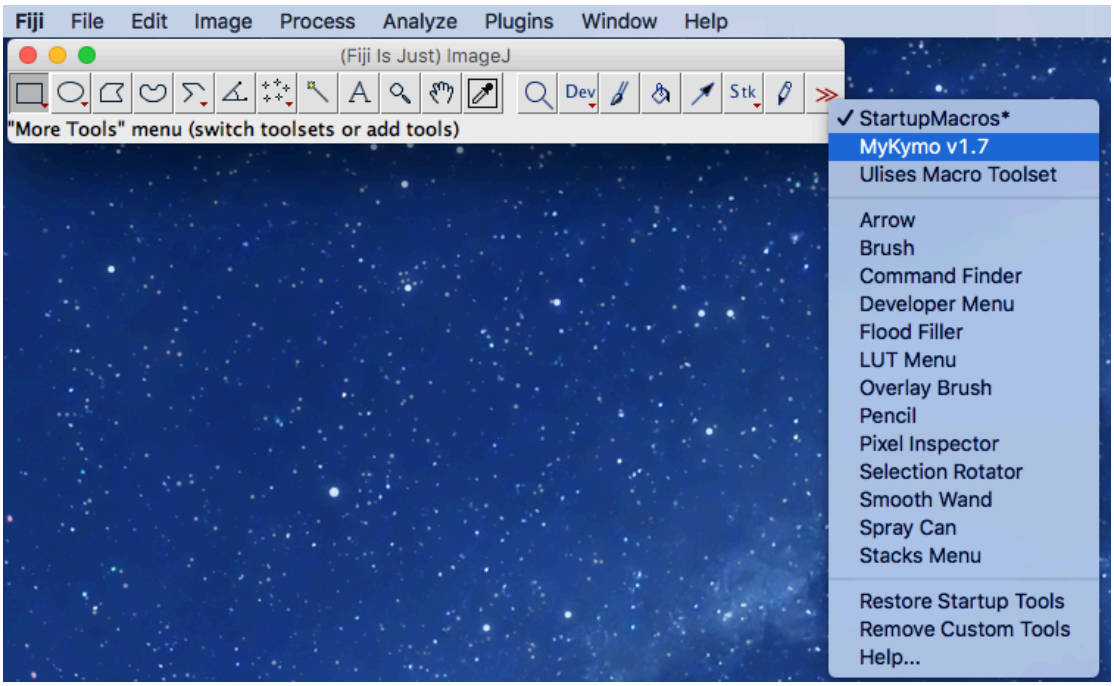

3. Now the Fiji panel looks like this:

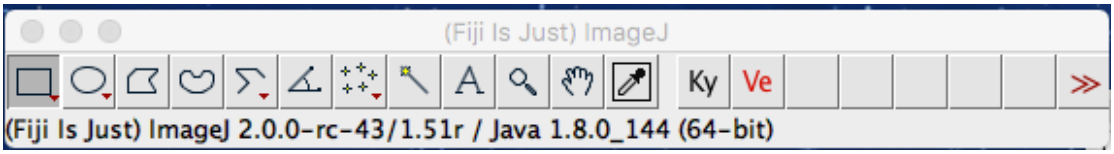

4. The first macro (Ky) produces the kymographs and the second (Ve) extracts kinetic parameters from trajectories traced on kymographs.

Part 3: Plotting a Kymograph

1. Load the data you want to analyze. It should be a multistack recording, the different stacks are images of the same region at different time points. The Bio-Formats plug in might be helpful for it (https://www.openmicroscopy.org/bio-formats/).
2. Trace a kymoline on your image, from left to right, by using “straight line” or “Segmented line”.

3. If you trace your line from right to left instead, the kymograph will be inverted. Right to left is recommended when anterograde particles from your recording are going from left to right too. It can be done either way, but take it into account.
4. The line can be a bit bended if the trajectories are not completely straight.
5. By double clicking the line tool, you can adjust the width of it. If it is wider it will include more data to plot the profile (this is not necessarily good). Best is to adjust it to a similar width to your organelle.

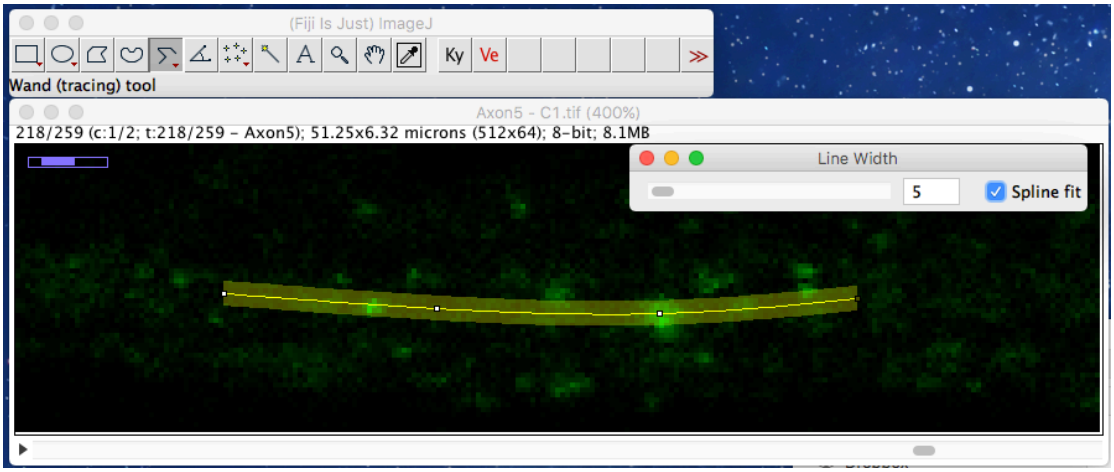

6. By plotting the profile (Analyze>Plot profile) of your line you can see your vesicles (in this case two). Play with the line width to see how the profiles change accordingly. On the left panel the line width was 2, on the right was 20. Notice that the Signal to noise (SNR) is higher one the left ~ (150:50) than on the right ~(65:40).

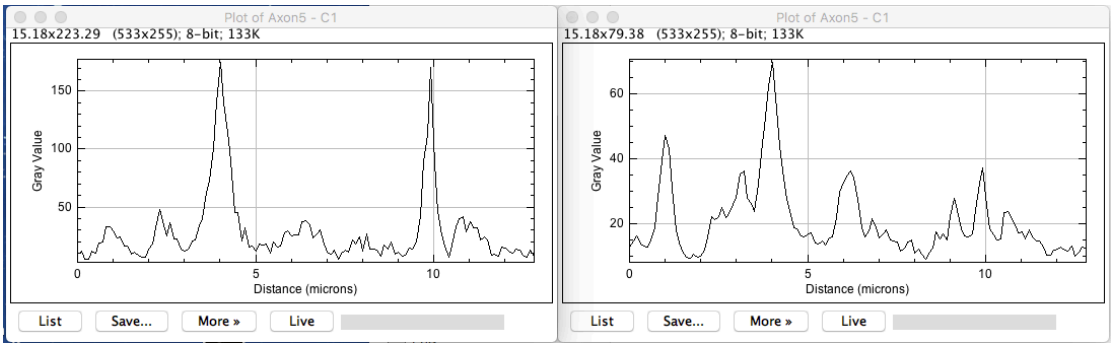

After choosing the best width, save your line as a ROI to the ROI manager (press “T”), rename it, and save the ROI in your data folder.

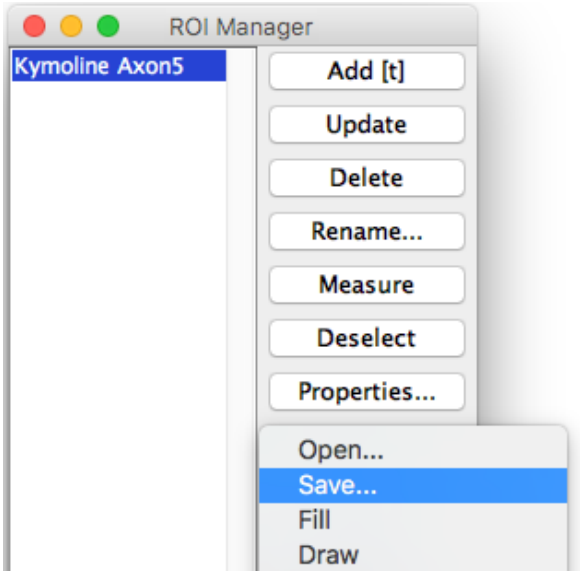

7. Now print the Kymograph from the Kymoline by pressing the macro “Ky”. Make sure that the active window is your Stack and that the kymoline is there.
8. A new window will appear with your kymograph

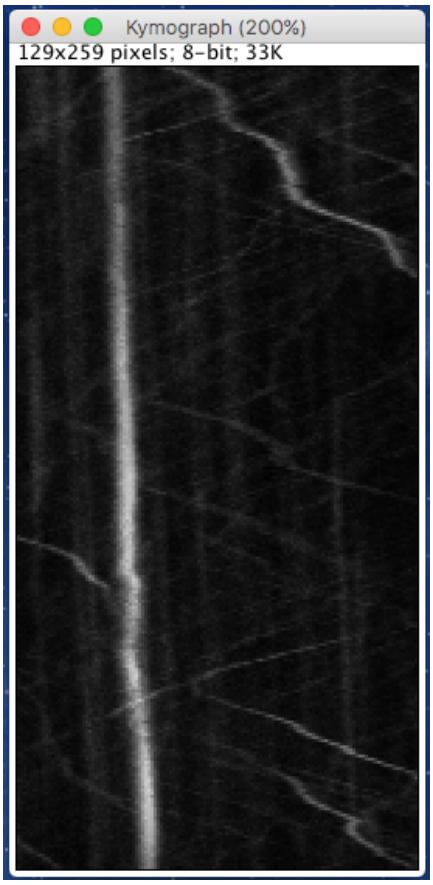

9. (Vertical lines are stationary particles)
10. Save it in your data folder.

Part 4: Velocities Analysis

1. Open your Kymograph image with Fiji
2. Right click on the macro “Velocities”. The following panel will open:

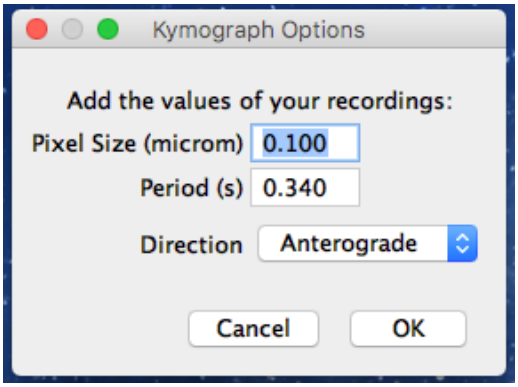

3. Introduce the corresponding values. You can find them in your original file. Choose which direction you want to analyze trajectories: Anterograde or Retrograde.
4. Press OK.

5. Use the segmented line to trace your trajectories.

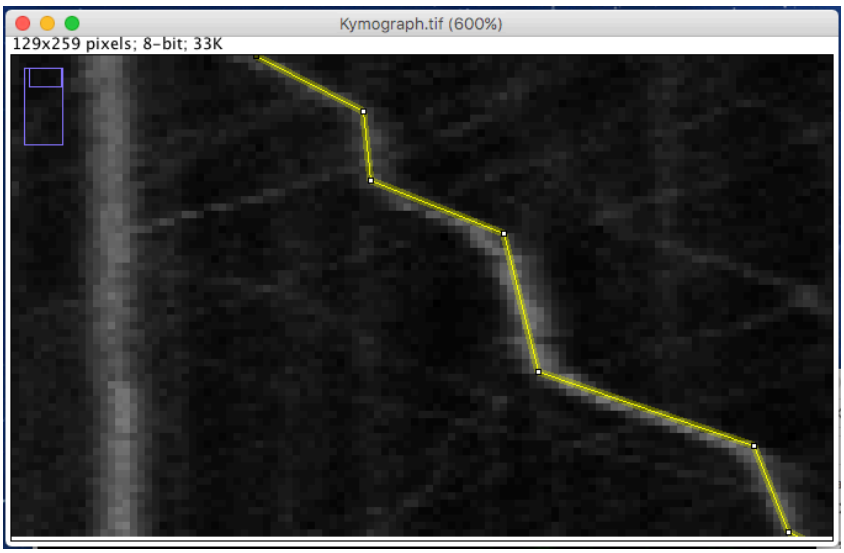

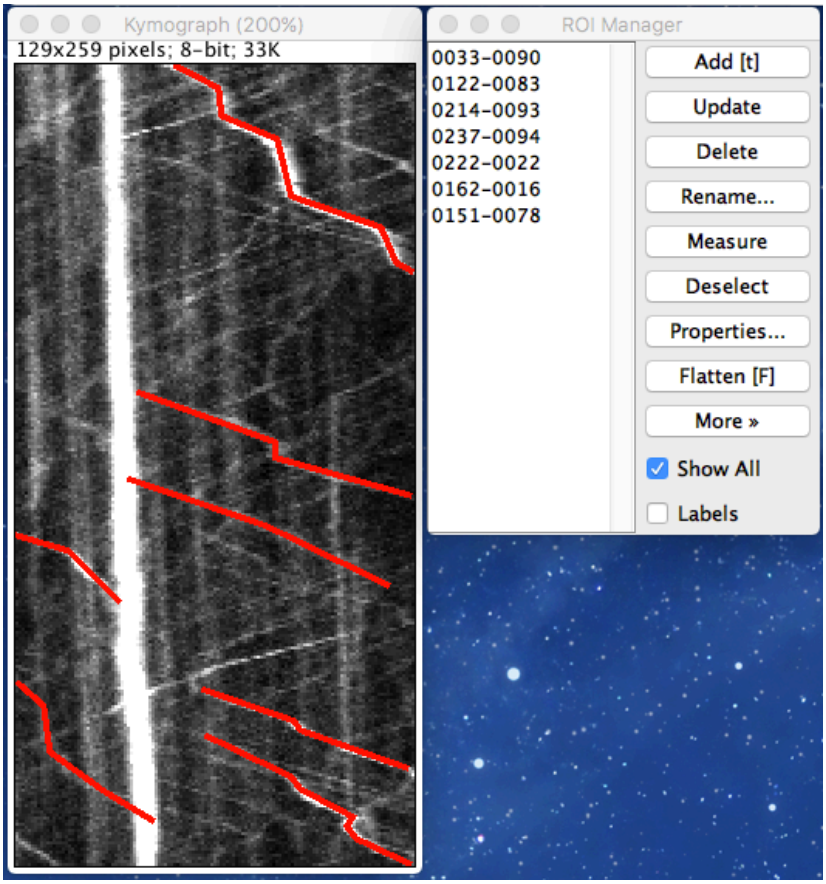

6. Save every trajectory one by one in your ROI Manager
7. Save all your ROIs as a single .zip file in your data directory.
8. Now you can run the “Velocities” macro. Click on it.

As outputs you get two files.

The first one is the “Log”:

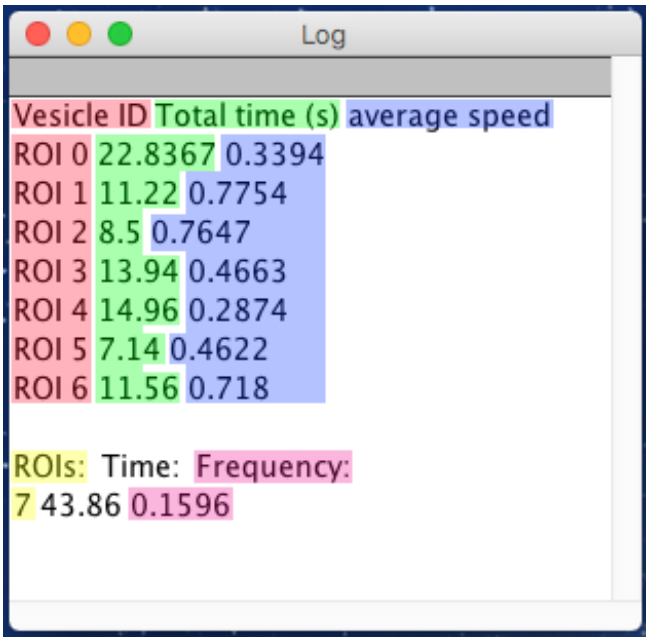

Here colored for clarity. The first column contains the ROIs ID (red), the second one contains the total time the trajectory was traced (green) and the third one the average speed of that vesicle (blue).

At the end of the Log file there is the total number of ROIs analyzed in the Kymograph (yellow), the total time window of the Kymograph (white) and the Frequency (number of ROIs/time)(purple). Save the file. It can be opened in a spreadsheet for further analysis.

The second output window contains the results. These consist on the kinetic data for every trajectory detailed (See next page). Rows correspond to every segmentation of the indicated trajectory. Columns indicate the following:

- vesicle ID: The ID of the vesicle
- dx now: Distance in pixels for the specified segment (row)
- dt now: Time in pixels for the specified segment
- actual speed: Velocity in pixels for the specified segment
- dx sum: Accumulated distance for the given vesicle
- dt sum: Accumulated time for the given vesicle
- average speed: average speed of the vesicle until that given segment
- period (s): Period at which the recording was acquired
- frequency (fps) : Frequency at which the recording was acquired (1/Period)
- pixel size (microm): Pixel size of the original image in µm
- dx now (microm): Distance in micrometers for the specified segment (row)
- dt now (s): Time in seconds for the specified segment
- actual speed (microm/s): Speed during the specified segment

- dx sum (microm): Accumulated distance in micrometers
- dt sum (s): Accumulted time in seconds until the specified segment
- average speed (microm/s): Accumulated verage speed until that row.

Notice that changes in direction within a trajectory appear as negative distance and therefore negative velocities (for an example see ROI 3, line 17).

9. Save the file in your data folder for further analysis.

10. If you want to analyze the trajectories that moved in the other direction (in this example would be retrograde), start again from step 4.

Results

	vesicle ID	dx now	dt now	actual speed	dx sum	dt sum	average speed	period (s)	frequency (fps)	pixel size (microm)	dx now (microm)	dt now (s)	actual speed (microm/s)	dx sum (microm)	dt sum (s)	average speed (microm/s)
1	ROI 0	14.500	7.500	1.933	14.500	7.500	1.933	0.340	2.941	0.100	1.450	2.550	0.569	1.450	2.550	0.569
2	ROI 0	1.000	9.333	0.107	15.500	16.833	0.921	0.340	2.941	0.100	0.100	3.173	0.032	1.550	5.723	0.271
3	ROI 0	18.000	7.333	2.455	33.500	24.167	1.386	0.340	2.941	0.100	1.800	2.493	0.722	3.350	8.217	0.408
4	ROI 0	4.667	18.667	0.250	38.167	42.833	0.891	0.340	2.941	0.100	0.467	6.347	0.074	3.817	14.563	0.262
5	ROI 0	29.167	9.833	2.966	67.333	52.667	1.278	0.340	2.941	0.100	2.917	3.343	0.872	6.733	17.907	0.376
6	ROI 0	4.833	11.667	0.414	72.167	64.333	1.122	0.340	2.941	0.100	0.483	3.967	0.122	7.217	21.873	0.330
7	ROI 0	5.333	2.833	1.882	77.500	67.167	1.154	0.340	2.941	0.100	0.533	0.963	0.554	7.750	22.837	0.339
8	ROI 1	44.000	16.000	2.750	44.000	16.000	2.750	0.340	2.941	0.100	4.400	5.440	0.809	4.400	5.440	0.809
9	ROI 1	0.000	5.000	0.000	44.000	21.000	2.095	0.340	2.941	0.100	0.000	1.700	0.000	4.400	7.140	0.616
10	ROI 1	43.000	12.000	3.583	87.000	33.000	2.636	0.340	2.941	0.100	4.300	4.080	1.054	8.700	11.220	0.775
11	ROI 2	29.000	10.000	2.900	29.000	10.000	2.900	0.340	2.941	0.100	2.900	3.400	0.853	2.900	3.400	0.853
12	ROI 2	2.000	3.000	0.667	31.000	13.000	2.385	0.340	2.941	0.100	0.200	1.020	0.196	3.100	4.420	0.701
13	ROI 2	34.000	12.000	2.833	65.000	25.000	2.600	0.340	2.941	0.100	3.400	4.080	0.833	6.500	8.500	0.765
14	ROI 3	27.000	13.000	2.077	27.000	13.000	2.077	0.340	2.941	0.100	2.700	4.420	0.611	2.700	4.420	0.611
15	ROI 3	3.000	4.000	0.750	30.000	17.000	1.765	0.340	2.941	0.100	0.300	1.360	0.221	3.000	5.780	0.519
16	ROI 3	17.000	9.000	1.889	47.000	26.000	1.808	0.340	2.941	0.100	1.700	3.060	0.556	4.700	8.840	0.532
17	ROI 3	-2.000	3.000	-0.667	45.000	29.000	1.552	0.340	2.941	0.100	-0.200	1.020	-0.196	4.500	9.860	0.456
18	ROI 3	3.000	4.000	0.750	48.000	33.000	1.455	0.340	2.941	0.100	0.300	1.360	0.221	4.800	11.220	0.428
19	ROI 3	17.000	8.000	2.125	65.000	41.000	1.585	0.340	2.941	0.100	1.700	2.720	0.625	6.500	13.940	0.466
20	ROI 4	8.000	7.000	1.143	8.000	7.000	1.143	0.340	2.941	0.100	0.800	2.380	0.336	0.800	2.380	0.336
21	ROI 4	2.000	15.000	0.133	10.000	22.000	0.455	0.340	2.941	0.100	0.200	5.100	0.039	1.000	7.480	0.134
22	ROI 4	18.000	13.000	1.385	28.000	35.000	0.800	0.340	2.941	0.100	1.800	4.420	0.407	2.800	11.900	0.235
23	ROI 4	15.000	9.000	1.667	43.000	44.000	0.977	0.340	2.941	0.100	1.500	3.060	0.490	4.300	14.960	0.287
24	ROI 5	17.000	5.000	3.400	17.000	5.000	3.400	0.340	2.941	0.100	1.700	1.700	1.000	1.700	1.700	1.000
25	ROI 5	16.000	16.000	1.000	33.000	21.000	1.571	0.340	2.941	0.100	1.600	5.440	0.294	3.300	7.140	0.462
26	ROI 6	44.000	15.000	2.933	44.000	15.000	2.933	0.340	2.941	0.100	4.400	5.100	0.863	4.400	5.100	0.863
27	ROI 6	39.000	19.000	2.053	83.000	34.000	2.441	0.340	2.941	0.100	3.900	6.460	0.604	8.300	11.560	0.718

List of abreviations

a.u.	arbitrary units
ANF	Atrial Neuropeptidergic Factor
Arf	ADP ribosylation factors
Arl	Arf-like protein
ATP	Adenosine triphosphate
AZ	Active Zone
BP	Binding Protein
bp	base pairs
BRP	Bruchpilot
COS cells	CV-1 (simian) in Origin and carrying the SV40 genetic material cells
CREs	Cis-regulatory elements
DCV	Dense Core Vesicle
DHC	Dynein Heavy Chain
DNA	Deoxyribonucleic acid
GA	Golgi Apparatus
GFP	Green Fluorescent Protein
Gie	GTPase indispensable for equal segregation of chromosomes
GST	Glutathione S-transferases
GTP	Guanosine triphosphate
HA	Human influenza hemagglutinin
HOPS	Homotypic Fusion and Protein Sorting
KHC	Kinesin Heavy Chain
KLC	Kinesin Light Chain
NIH	National Institute of Health (USA)
NMJ	Neuromuscular Junction
OE	overexpression
PSD	Post Synaptic Density
RBP	Rim Binding Protein
RFP	Red Fluorescent Protein
RNA	Ribonucleic acid
RNAi	RNA interference
siRNA	Small interfering RNA
SKIP	SifA and kinesin-interacting protein
Syt-1	Synaptotagmin 1
ToW	Tug of War
Y2H	Yeast two hybrid

References

References

Adams, M.D., Celniker, S.E., Holt, R.A., Evans, C.A., Gocayne, J.D., Amanatides, P.G., Scherer, S.E., Li, P.W., Hoskins, R.A., Galle, R.F., et al. (2000). The Genome Sequence of Drosophila melanogaster. Science *287*, 2185–2195.

Akins, M.R., Berk-Rauch, H.E., and Fallon, J.R. (2009). Presynaptic Translation: Stepping Out of the Postsynaptic Shadow. Front. Neural Circuits *3*.

Alberts, B., Johnson, A., Lewis, J., Raff, M., Roberts, K., and Walter, P. (2002). Ion Channels and the Electrical Properties of Membranes.

Andlauer, T.F., and Sigrist, S.J. (2012). Quantitative analysis of Drosophila larval neuromuscular junction morphology. Cold Spring Harb. Protoc. *2012*, pdb–prot068601.

Balderhaar, H.J. kleine, and Ungermann, C. (2013). CORVET and HOPS tethering complexes – coordinators of endosome and lysosome fusion. J Cell Sci *126*, 1307–1316.

Bate, M. (1990). The embryonic development of larval muscles in Drosophila. Development *110*, 791–804.

Blott, E.J., and Griffiths, G.M. (2002). Secretory lysosomes. Nat. Rev. Mol. Cell Biol. *3*, 122–131.

Böhme, M.A., Beis, C., Reddy-Alla, S., Reynolds, E., Mampell, M.M., Grasskamp, A.T., Lützkendorf, J., Bergeron, D.D., Driller, J.H., Babikir, H., et al. (2016). Active zone scaffolds differentially accumulate Unc13 isoforms to tune Ca^{2+} channel–vesicle coupling. Nat. Neurosci. *19*, 1311.

Bouchard, P., Penningroth, S.M., Cheung, A., Gagnon, C., and Bardin, C.W. (1981). erythro-9-[3-(2-Hydroxynonyl)]adenine is an inhibitor of sperm motility that blocks dynein ATPase and protein carboxylmethylase activities. Proc. Natl. Acad. Sci. U. S. A. *78*, 1033–1036.

Boucrot, E., Henry, T., Borg, J.-P., Gorvel, J.-P., and Méresse, S. (2005). The Intracellular Fate of Salmonella Depends on the Recruitment of Kinesin. Science *308*, 1174–1178.

Bradshaw, R.A., Brickey, W.W., and Walker, K.W. (1998). N-Terminal processing: the methionine aminopeptidase and Nα-acetyl transferase families. Trends Biochem. Sci. *23*, 263–267.

Brady, S.T. (1985). A novel brain ATPase with properties expected for the fast axonal transport motor. Nature *317*, 73.

Brand, A.H., and Perrimon, N. (1993). Targeted gene expression as a means of altering cell fates and generating dominant phenotypes. Development *118*, 401–415.

Brendza, K.M., Rose, D.J., Gilbert, S.P., and Saxton, W.M. (1999). Lethal Kinesin Mutations Reveal Amino Acids Important for ATPase Activation and Structural Coupling. J. Biol. Chem. *274*, 31506–31514.

Bucci, C., Thomsen, P., Nicoziani, P., McCarthy, J., and Deurs, B. van (2000). Rab7: A Key to Lysosome Biogenesis. Mol. Biol. Cell *11*, 467–480.

Burd, C.G., Strochlic, T.I., and Setty, S.R.G. (2004). Arf-like GTPases: not so Arf-like after all. Trends Cell Biol. *14*, 687–694.

Bury, L.A., and Sabo, S.L. (2011). Coordinated trafficking of synaptic vesicle and active zone proteins prior to synapse formation. Neural Develop. *6*, 24.

Busson, D., and Pret, A.-M. (2007). GAL4/UAS Targeted Gene Expression for Studying *Drosophila* Hedgehog Signaling. In Hedgehog Signaling Protocols, (Humana Press), pp. 161–201.

Chia, P.H., Li, P., and Shen, K. (2013). Cellular and molecular mechanisms underlying presynapse formation. J. Cell Biol. *203*, 11–22.

Chua, J.J.E., Butkevich, E., Worseck, J.M., Kittelmann, M., Grønborg, M., Behrmann, E., Stelzl, U., Pavlos, N.J., Lalowski, M.M., Eimer, S., et al. (2012). Phosphorylation-regulated axonal dependent transport of syntaxin 1 is mediated by a Kinesin-1 adapter. Proc. Natl. Acad. Sci. *109*, 5862–5867.

Cohen, J. (2007). NIH to End Chimp Breeding for Research. Science *316*, 1265–1265.

Consortium*, T.C. elegans S. (1998). Genome Sequence of the Nematode C. elegans: A Platform for Investigating Biology. Science *282*, 2012–2018.

Cooper, G.M. (2000). The Cell (Sinauer Associates).

Crossley, A.C., Crossley, N.A., and Crossley, C. (1978). The morphology and development of the Drosophila muscular system.

Darwin (1859). On the origin of species by means of natural selection, or, The preservation of favoured races in the struggle for life.

Dietzl, G., Chen, D., Schnorrer, F., Su, K.-C., Barinova, Y., Fellner, M., Gasser, B., Kinsey, K., Oppel, S., Scheiblauer, S., et al. (2007). A genome-wide transgenic RNAi library for conditional gene inactivation in Drosophila. Nature *448*, 151–156.

Dresbach, T., Torres, V., Wittenmayer, N., Altrock, W.D., Zamorano, P., Zuschratter, W., Nawrotzki, R., Ziv, N.E., Garner, C.C., and Gundelfinger, E.D. (2006). Assembly of Active Zone Precursor Vesicles obligatory trafficking of presynaptic cytomatrix proteins bassoon and piccolo via a trans-golgi compartment. J. Biol. Chem. *281*, 6038–6047.

Farías, G.G., Guardia, C.M., De Pace, R., Britt, D.J., and Bonifacino, J.S. (2017). BORC/kinesin-1 ensemble drives polarized transport of lysosomes into the axon. Proc. Natl. Acad. Sci. *114*, E2955–E2964.

Forman, D.S., Brown, K.J., and Promersberger, M.E. (1983). Selective inhibition of retrograde axonal transport byerythro-9-[3-(-2-hydroxynonyl)]adenine. Brain Res. *272*, 194–197.

Fouquet, W., Owald, D., Wichmann, C., Mertel, S., Depner, H., Dyba, M., Hallermann, S., Kittel, R.J., Eimer, S., and Sigrist, S.J. (2009). Maturation of active zone assembly by Drosophila Bruchpilot. J. Cell Biol. *186*, 129–145.

Franker, M.A.M., and Hoogenraad, C.C. (2013). Microtubule-based transport – basic mechanisms, traffic rules and role in neurological pathogenesis. J. Cell Sci. *126*, 2319–2329.

Fraser, M.J., Smith, G.E., and Summers, M.D. (1983). Acquisition of Host Cell DNA Sequences by Baculoviruses: Relationship Between Host DNA Insertions and FP Mutants

of Autographa californica and Galleria mellonella Nuclear Polyhedrosis Viruses. J. Virol. *47*, 287–300.

Fu, M., and Holzbaur, E.L.F. (2013). JIP1 regulates the directionality of APP axonal transport by coordinating kinesin and dynein motors. J. Cell Biol. *202*, 495–508.

Füger, P., Behrends, L.B., Mertel, S., Sigrist, S.J., and Rasse, T.M. (2007). Live imaging of synapse development and measuring protein dynamics using two-color fluorescence recovery after photo-bleaching at Drosophila synapses. Nat. Protoc. *2*, 3285–3298.

Füger, P., Sreekumar, V., Schüle, R., Kern, J.V., Stanchev, D.T., Schneider, C.D., Karle, K.N., Daub, K.J., Siegert, V.K., Flötenmeyer, M., et al. (2012). Spastic Paraplegia Mutation N256S in the Neuronal Microtubule Motor KIF5A Disrupts Axonal Transport in a Drosophila HSP Model. PLoS Genet *8*, e1003066.

Gauger, A.K., and Goldstein, L.S. (1993). The Drosophila kinesin light chain. Primary structure and interaction with kinesin heavy chain. J. Biol. Chem. *268*, 13657–13666.

Geng, J., and Klionsky, D.J. (2008). The Atg8 and Atg12 ubiquitin-like conjugation systems in macroautophagy. EMBO Rep. *9*, 859–864.

Gibbons, I.R., and Rowe, A.J. (1965). Dynein: A Protein with Adenosine Triphosphatase Activity from Cilia. Science *149*, 424–426.

Gindhart, J.G., Desai, C.J., Beushausen, S., Zinn, K., and Goldstein, L.S.B. (1998). Kinesin Light Chains Are Essential for Axonal Transport in Drosophila. J. Cell Biol. *141*, 443–454.

Glater, E.E., Megeath, L.J., Stowers, R.S., and Schwarz, T.L. (2006). Axonal transport of mitochondria requires milton to recruit kinesin heavy chain and is light chain independent. J. Cell Biol. *173*, 545–557.

Goldberg, D.J. (1982). Microinjection into an identified axon to study the mechanism of fast axonal transport. Proc. Natl. Acad. Sci. *79*, 4818–4822.

Grenningloh, G., Rehm, E.J., and Goodman, C.S. (1991). Genetic analysis of growth cone guidance in Drosophila: fasciclin II functions as a neuronal recognition molecule. Cell *67*, 45–57.

Gupta, V.K., Scheunemann, L., Eisenberg, T., Mertel, S., Bhukel, A., Koemans, T.S., Kramer, J.M., Liu, K.S.Y., Schroeder, S., Stunnenberg, H.G., et al. (2013). Restoring polyamines protects from age-induced memory impairment in an autophagy-dependent manner. Nat. Neurosci. *16*, 1453–1460.

Hallermann, S., Kittel, R.J., Wichmann, C., Weyhersmüller, A., Fouquet, W., Mertel, S., Owald, D., Eimer, S., Depner, H., Schwärzel, M., et al. (2010). Naked Dense Bodies Provoke Depression. J. Neurosci. *30*, 14340–14345.

Harrison, R.E., Bucci, C., Vieira, O.V., Schroer, T.A., and Grinstein, S. (2003). Phagosomes Fuse with Late Endosomes and/or Lysosomes by Extension of Membrane Protrusions along Microtubules: Role of Rab7 and RILP. Mol. Cell. Biol. *23*, 6494–6506.

Haucke, V., Neher, E., and Sigrist, S.J. (2011). Protein scaffolds in the coupling of synaptic exocytosis and endocytosis. Nat. Rev. Neurosci. *12*, 127.

Heuser, J. (1989). Changes in lysosome shape and distribution correlated with changes in cytoplasmic pH. J. Cell Biol. *108*, 855–864.

Hirokawa, N., and Noda, Y. (2008). Intracellular Transport and Kinesin Superfamily Proteins, KIFs: Structure, Function, and Dynamics. Physiol. Rev. *88*, 1089–1118.

Hirokawa, N., Niwa, S., and Tanaka, Y. (2010). Molecular Motors in Neurons: Transport Mechanisms and Roles in Brain Function, Development, and Disease. Neuron *68*, 610–638.

Hofmann, I., and Munro, S. (2006). An N-terminally acetylated Arf-like GTPase is localised to lysosomes and affects their motility. J Cell Sci *119*, 1494–1503.

Horiuchi, D., Barkus, R.V., Pilling, A.D., Gassman, A., and Saxton, W.M. (2005). APLIP1, a Kinesin Binding JIP-1/JNK Scaffold Protein, Influences the Axonal Transport of Both Vesicles and Mitochondria in Drosophila. Curr. Biol. *15*, 2137–2141.

Huo, L., Yue, Y., Ren, J., Yu, J., Liu, J., Yu, Y., Ye, F., Xu, T., Zhang, M., and Feng, W. (2012). The CC1-FHA Tandem as a Central Hub for Controlling the Dimerization and Activation of Kinesin-3 KIF1A. Structure *20*, 1550–1561.

Hurd, D.D., and Saxton, W.M. (1996). Kinesin Mutations Cause Motor Neuron Disease Phenotypes by Disrupting Fast Axonal Transport in Drosophila. Genetics *144*, 1075–1085.

Ito, K., Okada, R., Tanaka, N.K., and Awasaki, T. (2003). Cautionary observations on preparing and interpreting brain images using molecular biology-based staining techniques. Microsc. Res. Tech. *62*, 170–186.

Jahn, R., and Fasshauer, D. (2012). Molecular machines governing exocytosis of synaptic vesicles. Nature *490*, 201–207.

Jan, L.Y., and Jan, Y.N. (1976). Properties of the larval neuromuscular junction in Drosophila melanogaster. J. Physiol. *262*, 189–214.

Jenett, A., Rubin, G.M., Ngo, T.-T.B., Shepherd, D., Murphy, C., Dionne, H., Pfeiffer, B.D., Cavallaro, A., Hall, D., Jeter, J., et al. (2012). A GAL4-Driver Line Resource for Drosophila Neurobiology. Cell Rep. *2*, 991–1001.

Jennings, B.H. (2011). Drosophila – a versatile model in biology & medicine. Mater. Today *14*, 190–195.

Jiang, P., Nishimura, T., Sakamaki, Y., Itakura, E., Hatta, T., Natsume, T., and Mizushima, N. (2014). The HOPS complex mediates autophagosome–lysosome fusion through interaction with syntaxin 17. Mol. Biol. Cell *25*, 1327–1337.

Jin, E.J., Kiral, F.R., and Hiesinger, P.R. (2007). The where, what, and when of membrane protein degradation in neurons. Dev. Neurobiol. n/a-n/a.

Julien, J.-P., and Millecamps, S. (2013). Axonal transport deficits and neurodegenerative diseases. Nat. Rev. Neurosci. *14*, 161.

Kahn, R.A., Cherfils, J., Elias, M., Lovering, R.C., Munro, S., and Schurmann, A. (2006). Nomenclature for the human Arf family of GTP-binding proteins: ARF, ARL, and SAR proteins. J. Cell Biol. *172*, 645–650.

Kern, J.V., Zhang, Y.V., Kramer, S., Brenman, J.E., and Rasse, T.M. (2013). The Kinesin-3, Unc-104 Regulates Dendrite Morphogenesis and Synaptic Development in Drosophila. Genetics *195*, 59–72.

Khatter, D., Raina, V.B., Dwivedi, D., Sindhwani, A., Bahl, S., and Sharma, M. (2015). The small GTPase Arl8b regulates assembly of the mammalian HOPS complex on lysosomes. J Cell Sci *128*, 1746–1761.

Kim, E., and Jung, H. (2015). Local protein synthesis in neuronal axons: why and how we study. BMB Rep. *48*, 139–146.

Kittel, R.J., Wichmann, C., Rasse, T.M., Fouquet, W., Schmidt, M., Schmid, A., Wagh, D.A., Pawlu, C., Kellner, R.R., Willig, K.I., et al. (2006a). Bruchpilot promotes active zone assembly, Ca2+ channel clustering, and vesicle release. Science *312*, 1051–1054.

Kittel, R.J., Hallermann, S., Thomsen, S., Wichmann, C., Sigrist, S.J., and Heckmann, M. (2006b). Active zone assembly and synaptic release. Biochem. Soc. Trans. *34*, 939–941.

Klassen, M.P., Wu, Y.E., Maeder, C.I., Nakae, I., Cueva, J.G., Lehrman, E.K., Tada, M., Gengyo-Ando, K., Wang, G.J., Goodman, M., et al. (2010). An Arf-like small G protein, ARL-8, promotes the axonal transport of presynaptic cargoes by suppressing vesicle aggregation. Neuron *66*, 710–723.

Knight, A. (2008). The beginning of the end for chimpanzee experiments? Philos. Ethics Humanit. Med. PEHM *3*, 16.

Kononenko, N.L., and Haucke, V. (2015). Molecular Mechanisms of Presynaptic Membrane Retrieval and Synaptic Vesicle Reformation. Neuron *85*, 484–496.

Koon, A.C., and Budnik, V. (2012). Inhibitory Control of Synaptic and Behavioral Plasticity by Octopaminergic Signaling. J. Neurosci. *32*, 6312–6322.

Koon, A.C., Ashley, J., Barria, R., DasGupta, S., Brain, R., Waddell, S., Alkema, M.J., and Budnik, V. (2011). Autoregulatory and paracrine control of synaptic and behavioral plasticity by octopaminergic signaling. Nat. Neurosci. *14*, 190.

Korolchuk, V.I., Saiki, S., Lichtenberg, M., Siddiqi, F.H., Roberts, E.A., Imarisio, S., Jahreiss, L., Sarkar, S., Futter, M., Menzies, F.M., et al. (2011). Lysosomal positioning coordinates cellular nutrient responses. Nat. Cell Biol. *13*, 453–460.

Kudo, A., Awasaki, T., Ishikawa, Y., and Matsuo, T. (2017). piggyBac-and phiC31 integrase-mediated transgenesis in Drosophila prolongata. Genes Genet. Syst. 17–00024.

Kvon, E.Z., Kazmar, T., Stampfel, G., Yáñez-Cuna, J.O., Pagani, M., Schernhuber, K., Dickson, B.J., and Stark, A. (2014). Genome-scale functional characterization of *Drosophila* developmental enhancers *in vivo*. Nature *512*, 91.

Landgraf, M., and Thor, S. (2006). Development of Drosophila motoneurons: Specification and morphology. Semin. Cell Dev. Biol. *17*, 3–11.

Liang, Y., and Sigrist, S. (2018). Autophagy and proteostasis in the control of synapse aging and disease. Curr. Opin. Neurobiol. *48*, 113–121.

Lin, M.-Y., and Sheng, Z.-H. (2015). Regulation of mitochondrial transport in neurons. Exp. Cell Res. *334*, 35–44.

Linck, R.W., and Langevin, G.L. (1981). Reassembly of flagellar B (alpha beta) tubulin into singlet microtubules: consequences for cytoplasmic microtubule structure and assembly. J. Cell Biol. *89*, 323–337.

Liu, K.S.Y., Siebert, M., Mertel, S., Knoche, E., Wegener, S., Wichmann, C., Matkovic, T., Muhammad, K., Depner, H., Mettke, C., et al. (2011). RIM-Binding Protein, a Central Part of the Active Zone, Is Essential for Neurotransmitter Release. Science *334*, 1565–1569.

Liu-Yesucevitz, L., Bassell, G.J., Gitler, A.D., Hart, A.C., Klann, E., Richter, J.D., Warren, S.T., and Wolozin, B. (2011). Local RNA Translation at the Synapse and in Disease. J. Neurosci. Off. J. Soc. Neurosci. *31*, 16086–16093.

Lockery, S.R., and Goodman, M.B. (2009). The Quest for Action Potentials in C. elegans Neurons Hits a Plateau. Nat. Neurosci. *12*, 377–378.

Lockery, S.R., Goodman, M.B., and Faumont, S. (2009). First report of action potentials in a *C. elegans* neuron is premature. Nat. Neurosci. *12*, 365.

Luzio, J.P., Pryor, P.R., and Bright, N.A. (2007). Lysosomes: fusion and function. Nat. Rev. Mol. Cell Biol. *8*, 622.

Luzio, J.P., Hackmann, Y., Dieckmann, N.M.G., and Griffiths, G.M. (2014). The Biogenesis of Lysosomes and Lysosome-Related Organelles. Cold Spring Harb. Perspect. Biol. *6*, a016840.

Maas, C., Torres, V.I., Altrock, W.D., Leal-Ortiz, S., Wagh, D., Terry-Lorenzo, R.T., Fejtova, A., Gundelfinger, E.D., Ziv, N.E., and Garner, C.C. (2012). Formation of Golgi-Derived Active Zone Precursor Vesicles. J. Neurosci. *32*, 11095–11108.

Maday, S., Wallace, K.E., and Holzbaur, E.L.F. (2012). Autophagosomes initiate distally and mature during transport toward the cell soma in primary neurons. J. Cell Biol. *196*, 407–417.

Maeder, C.I., San-Miguel, A., Wu, E.Y., Lu, H., and Shen, K. (2014). In Vivo Neuron-Wide Analysis of Synaptic Vesicle Precursor Trafficking. Traffic *15*, 273–291.

Marks, M.S., Heijnen, H.F., and Raposo, G. (2013). Lysosome-related organelles: unusual compartments become mainstream. Curr. Opin. Cell Biol. *25*, 495–505.

Mellem, J.E., Brockie, P.J., Madsen, D.M., and Maricq, A.V. (2008). Action potentials contribute to neuronal signaling in *C. elegans*. Nat. Neurosci. *11*, 865.

Menon, K.P., Carrillo, R.A., and Zinn, K. (2013). Development and plasticity of the Drosophila larval neuromuscular junction. Wiley Interdiscip. Rev. Dev. Biol. *2*, 647–670.

Miki, H., Okada, Y., and Hirokawa, N. (2005). Analysis of the kinesin superfamily: insights into structure and function. Trends Cell Biol. *15*, 467–476.

Mochizuki, H., Toda, H., Ando, M., Kurusu, M., Tomoda, T., and Furukubo-Tokunaga, K. (2011). Unc-51/ATG1 Controls Axonal and Dendritic Development via Kinesin-Mediated Vesicle Transport in the Drosophila Brain. PLoS ONE *6*, e19632.

Moreau, K., Ravikumar, B., Renna, M., Puri, C., and Rubinsztein, D.C. (2011). Autophagosome Precursor Maturation Requires Homotypic Fusion. Cell *146*, 303–317.

Morgan, T.H. (1911). The Origin of Five Mutations in Eye Color in Drosophila and Their Modes of Inheritance. Science *33*, 534–537.

Mozziconacci, J., Sandblad, L., Wachsmuth, M., Brunner, D., and Karsenti, E. (2008). Tubulin Dimers Oligomerize before Their Incorporation into Microtubules. PLOS ONE *3*, e3821.

Muhammad, K., Reddy-Alla, S., Driller, J.H., Schreiner, D., Rey, U., Böhme, M.A., Hollmann, C., Ramesh, N., Depner, H., Lützkendorf, J., et al. (2015). Presynaptic spinophilin tunes neurexin signalling to control active zone architecture and function. Nat. Commun. *6*, 8362.

Müller, M.J.I., Klumpp, S., and Lipowsky, R. (2008). Motility States of Molecular Motors Engaged in a Stochastic Tug-of-War. J. Stat. Phys. *133*, 1059–1081.

Muller, M.J.I., Klumpp, S., and Lipowsky, R. (2008). Tug-of-war as a cooperative mechanism for bidirectional cargo transport by molecular motors. Proc. Natl. Acad. Sci. U. S. A. *105*, 4609–4614.

Müller, M.J.I., Klumpp, S., and Lipowsky, R. (2010). Bidirectional Transport by Molecular Motors: Enhanced Processivity and Response to External Forces. Biophys. J. *98*, 2610–2618.

Murthy, V.N., and Camilli, P.D. (2003). Cell Biology of the Presynaptic Terminal. Annu. Rev. Neurosci. *26*, 701–728.

Napoli, C., Lemieux, C., and Jorgensen, R. (1990). Introduction of a Chimeric Chalcone Synthase Gene into Petunia Results in Reversible Co-Suppression of Homologous Genes in trans. Plant Cell *2*, 279–289.

Nie, Z., Boehm, M., Boja, E.S., Vass, W.C., Bonifacino, J.S., Fales, H.M., and Randazzo, P.A. (2003). Specific Regulation of the Adaptor Protein Complex AP-3 by the Arf GAP AGAP1. Dev. Cell *5*, 513–521.

Okai, T., Araki, Y., Tada, M., Tateno, T., Kontani, K., and Katada, T. (2004). Novel small GTPase subfamily capable of associating with tubulin is required for chromosome segregation. J. Cell Sci. *117*, 4705–4715.

Otokawa, M. (1972). Stimulation of ATPase activity of 30-S dynein with microtubular protein. Biochim. Biophys. Acta BBA - Bioenerg. *275*, 464–466.

Owald, D., Fouquet, W., Schmidt, M., Wichmann, C., Mertel, S., Depner, H., Christiansen, F., Zube, C., Quentin, C., Körner, J., et al. (2010). A Syd-1 homologue regulates pre- and postsynaptic maturation in Drosophila. J. Cell Biol. *188*, 565–579.

Owald, D., Khorramshahi, O., Gupta, V.K., Banovic, D., Depner, H., Fouquet, W., Wichmann, C., Mertel, S., Eimer, S., Reynolds, E., et al. (2012). Cooperation of Syd-1 with Neurexin synchronizes pre- with postsynaptic assembly. Nat. Neurosci. *15*, 1219–1226.

Pack-Chung, E., Kurshan, P.T., Dickman, D.K., and Schwarz, T.L. (2007). A Drosophila kinesin required for synaptic bouton formation and synaptic vesicle transport. Nat. Neurosci. *10*, 980–989.

Patel, N., Thierry-Mieg, D., and Mancillas, J.R. (1993). Cloning by insertional mutagenesis of a cDNA encoding Caenorhabditis elegans kinesin heavy chain. Proc. Natl. Acad. Sci. *90*, 9181–9185.

Peled, E.S., Newman, Z.L., and Isacoff, E.Y. (2014). Evoked and Spontaneous Transmission Favored by Distinct Sets of Synapses. Curr. Biol. *24*, 484–493.

Pennetta, G., Hiesinger, P.R., Fabian-Fine, R., Meinertzhagen, I.A., and Bellen, H.J. (2002). Drosophila VAP-33A Directs Bouton Formation at Neuromuscular Junctions in a Dosage-Dependent Manner. Neuron *35*, 291–306.

Petzoldt, A.G., Lee, Y.-H., Khorramshahi, O., Reynolds, E., Plested, A.J.R., Herzel, H., and Sigrist, S.J. (2014). Gating Characteristics Control Glutamate Receptor Distribution and Trafficking In Vivo. Curr. Biol. *24*, 2059–2065.

Pilling, A.D., Horiuchi, D., Lively, C.M., and Saxton, W.M. (2006). Kinesin-1 and Dynein Are the Primary Motors for Fast Transport of Mitochondria in Drosophila Motor Axons. Mol. Biol. Cell *17*, 2057–2068.

Podufall, J., Tian, R., Knoche, E., Puchkov, D., Walter, A.M., Rosa, S., Quentin, C., Vukoja, A., Jung, N., Lampe, A., et al. (2014). A Presynaptic Role for the Cytomatrix Protein GIT in Synaptic Vesicle Recycling. Cell Rep. *7*, 1417–1425.

Pulipparacharuvil, S., Akbar, M.A., Ray, S., Sevrioukov, E.A., Haberman, A.S., Rohrer, J., and Krämer, H. (2005). Drosophila Vps16A is required for trafficking to lysosomes and biogenesis of pigment granules. J. Cell Sci. *118*, 3663–3673.

Qin, G., Schwarz, T., Kittel, R.J., Schmid, A., Rasse, T.M., Kappei, D., Ponimaskin, E., Heckmann, M., and Sigrist, S.J. (2005). Four Different Subunits Are Essential for Expressing the Synaptic Glutamate Receptor at Neuromuscular Junctions of *Drosophila*. J. Neurosci. *25*, 3209–3218.

Reddy, A., Caler, E.V., and Andrews, N.W. (2001). Plasma membrane repair is mediated by Ca(2+)-regulated exocytosis of lysosomes. Cell *106*, 157–169.

Reddy-Alla, S., Böhme, M.A., Reynolds, E., Beis, C., Grasskamp, A.T., Mampell, M.M., Maglione, M., Jusyte, M., Rey, U., Babikir, H., et al. (2017). Stable Positioning of Unc13 Restricts Synaptic Vesicle Fusion to Defined Release Sites to Promote Synchronous Neurotransmission. Neuron *95*, 1350–1364.e12.

Rohrer, J., Schweizer, A., Russell, D., and Kornfeld, S. (1996). The targeting of Lamp1 to lysosomes is dependent on the spacing of its cytoplasmic tail tyrosine sorting motif relative to the membrane. J. Cell Biol. *132*, 565–576.

Ronzano, R. (2017). Astrocytes, microglie et plasticité synaptique. médecine/sciences *33*, 1071–1078.

Rosa-Ferreira, C., and Munro, S. (2011). Arl8 and SKIP Act Together to Link Lysosomes to Kinesin-1. Dev. Cell *21*, 1171–1178.

Ruiz-Canada, C., Ashley, J., Moeckel-Cole, S., Drier, E., Yin, J., and Budnik, V. (2004). New Synaptic Bouton Formation Is Disrupted by Misregulation of Microtubule Stability in aPKC Mutants. Neuron *42*, 567–580.

Sánchez-Soriano, N., Tear, G., Whitington, P., and Prokop, A. (2007). Drosophila as a genetic and cellular model for studies on axonal growth. Neural Develop. *2*, 9.

Saxton, W.M., Hicks, J., Goldstein, L.S.B., and Raff, E.C. (1991). Kinesin heavy chain is essential for viability and neuromuscular functions in Drosophila, but mutants show no defects in mitosis. Cell *64*, 1093–1102.

Schindelin, J., Arganda-Carreras, I., Frise, E., Kaynig, V., Longair, M., Pietzsch, T., Preibisch, S., Rueden, C., Saalfeld, S., Schmid, B., et al. (2012). Fiji: an open-source platform for biological-image analysis. Nat. Methods *9*, 676–682.

Schmid, A., Hallermann, S., Kittel, R.J., Khorramshahi, O., Frölich, A.M.J., Quentin, C., Rasse, T.M., Mertel, S., Heckmann, M., and Sigrist, S.J. (2008). Activity-dependent site-specific changes of glutamate receptor composition in vivo. Nat. Neurosci. *11*, 659–666.

Schoch, S., and Gundelfinger, E.D. (2006). Molecular organization of the presynaptic active zone. Cell Tissue Res. *326*, 379–391.

Schuster, C.M. (2006). Glutamatergic synapses of *Drosophila* neuromuscular junctions: a high-resolution model for the analysis of experience-dependent potentiation. Cell Tissue Res. *326*, 287.

Setty, S.R.G., Tenza, D., Sviderskaya, E.V., Bennett, D.C., Raposo, G., and Marks, M.S. (2008). Cell-specific ATP7A transport sustains copper-dependent tyrosinase activity in melanosomes. Nature *454*, 1142–1146.

Shapira, M., Zhai, R.G., Dresbach, T., Bresler, T., Torres, V.I., Gundelfinger, E.D., Ziv, N.E., and Garner, C.C. (2003). Unitary Assembly of Presynaptic Active Zones from Piccolo-Bassoon Transport Vesicles. Neuron *38*, 237–252.

Siebert, M., Böhme, M.A., Driller, J.H., Babikir, H., Mampell, M.M., Rey, U., Ramesh, N., Matkovic, T., Holton, N., Reddy-Alla, S., et al. (2015). A high affinity RIM-binding protein/Aplip1 interaction prevents the formation of ectopic axonal active zones. ELife *4*, e06935.

Sigrist, S.J., and Schmitz, D. (2011). Structural and functional plasticity of the cytoplasmic active zone. Curr. Opin. Neurobiol. *21*, 144–150.

Spudich, J.A. (2011). Molecular Motors, Beauty in Complexity. Science *331*, 1143–1144.

Stenmark, H., Aasland, R., Toh, B.-H., and D'Arrigo, A. (1996). Endosomal Localization of the Autoantigen EEA1 Is Mediated by a Zinc-binding FYVE Finger. J. Biol. Chem. *271*, 24048–24054.

Stephen D. Skaper, Laura Facci, Morena Zusso, and Pietro Giusti (2017). Neuroinflammation, Mast Cells, and Glia: Dangerous Liaisons. The Neuroscientist *23*, 478–498.

Stephens, R.E. (1970). Thermal fractionation of outer fiber doublet microtubules into A- and B-subfiber components. A- and B-tubulin. J. Mol. Biol. *47*, 353–363.

Stewart, B.A., Atwood, H.L., Renger, J.J., Wang, J., and Wu, C.-F. (1994). Improved stability of Drosophila larval neuromuscular preparations in haemolymph-like physiological solutions. J. Comp. Physiol. A *175*, 179–191.

Stowers, R.S., Megeath, L.J., Górska-Andrzejak, J., Meinertzhagen, I.A., and Schwarz, T.L. (2002). Axonal Transport of Mitochondria to Synapses Depends on Milton, a Novel Drosophila Protein. Neuron *36*, 1063–1077.

Su, Z., Shen, H., Wang, H., Wang, J., Li, J., Nienhaus, G.U., Shang, L., and Wei, G. (2015). Motif-Designed Peptide Nanofibers Decorated with Graphene Quantum Dots for Simultaneous Targeting and Imaging of Tumor Cells. Adv. Funct. Mater. *25*, 5472–5478.

Südhof, T.C. (2012). The Presynaptic Active Zone. Neuron *75*, 11–25.

Südhof, T.C. (2013). A molecular machine for neurotransmitter release: synaptotagmin and beyond. Nat. Med. *19*, 1227–1231.

Sweeney, S.T., and Davis, G.W. (2002). Unrestricted Synaptic Growth in spinster—a Late Endosomal Protein Implicated in TGF-β-Mediated Synaptic Growth Regulation. Neuron *36*, 403–416.

Takáts, S., Pircs, K., Nagy, P., Varga, Á., Kárpáti, M., Heged\Hus, K., Kramer, H., Kovács, A.L., Sass, M., and Juhász, G. (2014). Interaction of the HOPS complex with Syntaxin 17 mediates autophagosome clearance in Drosophila. Mol. Biol. Cell *25*, 1338–1354.

Tamkun, J.W., Kahn, R.A., Kissinger, M., Brizuela, B.J., Rulka, C., Scott, M.P., and Kennison, J.A. (1991). The arflike gene encodes an essential GTP-binding protein in Drosophila. Proc. Natl. Acad. Sci. *88*, 3120–3124.

Tanaka, Y., Kanai, Y., Okada, Y., Nonaka, S., Takeda, S., Harada, A., and Hirokawa, N. (1998). Targeted disruption of mouse conventional kinesin heavy chain, kif5B, results in abnormal perinuclear clustering of mitochondria. Cell *93*, 1147–1158.

Tao-Cheng, J.-H. (2007). Ultrastructural Localization of Active Zone and Synaptic Vesicle Proteins in a Preassembled Multi-vesicle Transport Aggregate. Neuroscience *150*, 575–584.

Toda, H., Mochizuki, H., Flores, R., Josowitz, R., Krasieva, T.B., LaMorte, V.J., Suzuki, E., Gindhart, J.G., Furukubo-Tokunaga, K., and Tomoda, T. (2008). UNC-51/ATG1 kinase regulates axonal transport by mediating motor–cargo assembly. Genes Dev. *22*, 3292–3307.

Tokuyasu, K.T. (1973). A technique for ultracryotomy of cell suspensions and tissues. J. Cell Biol. *57*, 551–565.

Trotta, T., Panaro, M.A., Cianciulli, A., Mori, G., Di Benedetto, A., and Porro, C. (2018). Microglia-derived extracellular vesicles in Alzheimer's Disease: a double-edged sword. Biochem. Pharmacol.

Tsien, H.C., and Wattiaux, J.M. (1971). Effect of maternal age on DNA and RNA content of Drosophila eggs. Nature. New Biol. *230*, 147–148.

Tsuji, S. (2006). René Couteaux (1909–1999) and the morphological identification of synapses. Biol. Cell *98*, 503–509.

Valakh, V., Naylor, S.A., Berns, D.S., and DiAntonio, A. (2012). A large-scale RNAi screen identifies functional classes of genes shaping synaptic development and maintenance. Dev. Biol. *366*, 163–171.

Vale, R.D., Reese, T.S., and Sheetz, M.P. (1985). Identification of a novel force-generating protein, kinesin, involved in microtubule-based motility. Cell *42*, 39–50.

Verstreken, P., Ohyama, T., and Bellen, H.J. (2008). FM 1-43 Labeling of Synaptic Vesicle Pools at the *Drosophila* Neuromuscular Junction. In Exocytosis and Endocytosis, (Humana Press), pp. 349–369.

Vicario-Orri, E., Opazo, C.M., and Munoz, F.J. (2015). The pathophysiology of axonal transport in Alzheimer's disease. J. Alzheimers Dis. *43*, 1097–1113.

Vukoja (2014). The Role of the Small GTPase Arl8 in Development and Morphology of the Fly Neuromuscular Junction.

Wagh, D.A., Rasse, T.M., Asan, E., Hofbauer, A., Schwenkert, I., Dürrbeck, H., Buchner, S., Dabauvalle, M.-C., Schmidt, M., Qin, G., et al. (2006). Bruchpilot, a protein with homology to ELKS/CAST, is required for structural integrity and function of synaptic active zones in Drosophila. Neuron *49*, 833–844.

Wilhelm, B.G., Mandad, S., Truckenbrodt, S., Kröhnert, K., Schäfer, C., Rammner, B., Koo, S.J., Claßen, G.A., Krauss, M., Haucke, V., et al. (2014). Composition of isolated synaptic boutons reveals the amounts of vesicle trafficking proteins. Science *344*, 1023–1028.

Wong, Y.L., and Rice, S.E. (2010). Kinesin's light chains inhibit the head- and microtubule-binding activity of its tail. Proc. Natl. Acad. Sci. U. S. A. *107*, 11781–11786.

Wong, M.Y., Zhou, C., Shakiryanova, D., Lloyd, T.E., Deitcher, D.L., and Levitan, E.S. (2012). Neuropeptide Delivery to Synapses by Long-Range Vesicle Circulation and Sporadic Capture. Cell *148*, 1029–1038.

Wu, Y.E., Huo, L., Maeder, C.I., Feng, W., and Shen, K. (2013). The Balance between Capture and Dissociation of Presynaptic Proteins Controls the Spatial Distribution of Synapses. Neuron *78*, 994–1011.

Yonekawa, Y., Harada, A., Okada, Y., Funakoshi, T., Kanai, Y., Takei, Y., Terada, S., Noda, T., and Hirokawa, N. (1998). Defect in Synaptic Vesicle Precursor Transport and Neuronal Cell Death in KIF1A Motor Protein–deficient Mice. J. Cell Biol. *141*, 431–441.

Zhai, R.G., Vardinon-Friedman, H., Cases-Langhoff, C., Becker, B., Gundelfinger, E.D., Ziv, N.E., and Garner, C.C. (2001). Assembling the Presynaptic Active Zone: A Characterization of an Active Zone Precursor Vesicle. Neuron *29*, 131–143.

Zhang, B., Koh, Y.H., Beckstead, R.B., Budnik, V., Ganetzky, B., and Bellen, H.J. (1998). Synaptic Vesicle Size and Number Are Regulated by a Clathrin Adaptor Protein Required for Endocytosis. Neuron *21*, 1465–1475.

Zhang, M., Chen, L., Wang, S., and Wang, T. (2009). Rab7: roles in membrane trafficking and disease. Biosci. Rep. *29*, 193.

Zhao, W., Moest, T., Zhao, Y., Guilhon, A.-A., Buffat, C., Gorvel, J.-P., and Méresse, S. (2015). The Salmonella effector protein SifA plays a dual role in virulence. Sci. Rep. *5*.

Zhou, Q., Zhou, P., Wang, A.L., Wu, D., Zhao, M., Südhof, T.C., and Brunger, A.T. (2017). The primed SNARE–complexin–synaptotagmin complex for neuronal exocytosis. Nature *548*, 420.

(1982). Advances in Genetics, Development, and Evolution of Drosophila (Boston, MA: Springer US).